



University  
of Glasgow

Toland, Karl William (2015) *Development and characterisation of a pulling machine to produce small diameter silica fibres for use in prototype advanced gravitational wave detectors*. MSc(R) thesis.

<http://theses.gla.ac.uk/6997/>

Copyright and moral rights for this thesis are retained by the author

A copy can be downloaded for personal non-commercial research or study

This thesis cannot be reproduced or quoted extensively from without first obtaining permission in writing from the Author

The content must not be changed in any way or sold commercially in any format or medium without the formal permission of the Author

When referring to this work, full bibliographic details including the author, title, awarding institution and date of the thesis must be given

# Development and characterisation of a pulling machine to produce small diameter silica fibres for use in prototype advanced gravitational wave detectors

Karl William Toland, BSc(Hons)



University  
of Glasgow

Submitted in fulfilment of the requirements for the  
Degree of Master of Science by Research

Institute for Gravitational Research  
School of Physics and Astronomy  
College of Science and Engineering  
The University of Glasgow

Submitted December 2015

# Abstract

This thesis will give an overview of gravitational waves and the history behind attempts to directly observe them using laser based interferometers and the detectors current configuration. The noise sources associated with the interferometers such as gravity gradient, seismic and quantum noise will also be discussed. Thermal noise will be discussed in depth.

The main body of this thesis focused on developing and characterising a pulling machine capable of producing small diameter silica fibres for use in prototype advanced gravitational wave detectors. An initial diameter target was to pull repeatable sets of fibres with a minimum diameter  $\leq 20 \mu\text{m}$ . The pulling machine worked by heating a silica stock, with one end clamped down and the other clamped to a high velocity pulling stage, with a  $\text{CO}_2$  laser until the stock was sufficiently hot enough and producing a fibre by moving the pulling stage. The  $\text{CO}_2$  beam was directed to and focused down onto the stock using a series of mirrors and two lenses to a beam width of  $105 \pm 7 \mu\text{m}$ . Three different methods were used to create fibres: one stage absolute position pull, one stage velocity profile pull and two stage velocity profile pulls.

The one stage absolute position pull produced fibres that would taper down to a minimum diameter ranging between 20 to 48  $\mu\text{m}$ .

The one stage velocity profile pulls produced fibres ranging between  $7.4 \pm 0.4 \mu\text{m}$  and  $18.3 \pm 0.6 \mu\text{m}$ . These fibres then ranged in breaking stress values of  $2.26 \pm 0.26 \times 10^8 \text{ Pa}$  and  $6.05 \pm 0.39 \times 10^9 \text{ Pa}$  and a Young's modulus value between  $14.4 \pm 1.7 \times 10^9 \text{ Pa}$  and  $106.0 \pm 6.8 \times 10^9 \text{ Pa}$ .

The two stage velocity profile pulls produced fibres ranging between  $8.72 \pm 0.61 \mu\text{m}$  and  $14.83 \pm 0.57 \mu\text{m}$ . These fibres then ranged in breaking stress values of  $2.14 \pm 0.3 \times 10^9 \text{ Pa}$  and  $4.82 \pm 0.36 \times 10^9 \text{ Pa}$  and a Young's modulus value between  $54.0 \pm 7.5 \times 10^9 \text{ Pa}$  and  $87.0 \pm 14.3 \times 10^9 \text{ Pa}$ .

The thinnest set of fibres were produced with two stage pulls and were found to have a higher Young's modulus value than the literature value for bulk fused silica, indicating a possible change in properties when the diameter is  $\leq 10 \mu\text{m}$ . Further investigation will need to be carried out to find out if this is the case.

The target of producing repeatable silica fibres with a minimum diameter  $\leq 20 \mu\text{m}$  was met. There is still a lot of work to be completed with regards to perfecting the fibre's shape, improving the strength and investigating the loss associated with the fibre. This will be carried out in the future.

# Contents

<b>1</b>	<b>Gravitational Waves</b>	<b>1</b>
1.1	Introduction to Gravitational Waves . . . . .	1
1.2	Gravitational Wave Sources . . . . .	4
1.2.1	Burst Sources . . . . .	5
1.2.2	Periodic Sources . . . . .	8
1.3	Instruments used to detect gravitational waves . . . . .	9
1.3.1	Resonant Bars . . . . .	9
1.3.2	Ground Based Laser Interferometers . . . . .	10
1.3.3	Space Based Laser Interferometers . . . . .	16
1.4	Noise Sources . . . . .	17
1.4.1	Gravity Gradient Noise . . . . .	18
1.4.2	Seismic Noise . . . . .	19
1.4.3	Quantum Noise . . . . .	21
1.4.4	Thermal Noise . . . . .	24
1.5	Work at Glasgow . . . . .	24
<b>2</b>	<b>Thermal Noise</b>	<b>26</b>
2.1	Introduction . . . . .	26
2.2	Suspension thermal noise . . . . .	27
2.2.1	Sources of dissipation . . . . .	27
2.2.2	Thermoelastic loss . . . . .	31
2.2.3	Dissipation Dilution . . . . .	32
2.2.4	Violin mode . . . . .	35
2.3	Conclusion . . . . .	36
<b>3</b>	<b>Development of the fibre pulling machine</b>	<b>37</b>
3.1	Aim of this project . . . . .	37
3.1.1	General concept of pulling machine to produce small diameter silica fibres . . . . .	39
3.2	Design . . . . .	42
3.2.1	Initial Design . . . . .	42
3.2.2	Current configuration and alignment process . . . . .	46
3.2.3	Future changes . . . . .	54
3.3	Beam Profiling . . . . .	55

3.3.1	Beam Simulation . . . . .	55
3.3.2	Experiment to measure the beam waist . . . . .	57
3.3.3	Experimental results . . . . .	60
3.3.4	Error analysis and conclusion . . . . .	65
3.4	Characterising the pulling stage . . . . .	67
3.4.1	Introduction . . . . .	67
3.4.2	Position set 1 . . . . .	68
3.4.3	Position set 2 . . . . .	73
3.4.4	Position set 3 . . . . .	75
3.4.5	Improvements and conclusion . . . . .	78
<b>4</b>	<b>Fibre production - one stage pull</b>	<b>80</b>
4.1	Absolute position pull method . . . . .	80
4.1.1	Fibre pulling procedure . . . . .	81
4.1.2	Fibre profiles and analysis . . . . .	83
4.2	Velocity profile pull method . . . . .	89
4.2.1	Velocity profile for the fibre pull . . . . .	89
4.2.2	Fibre profiles and analysis . . . . .	91
4.2.3	Strength testing . . . . .	96
4.2.4	Young's Modulus . . . . .	100
4.2.5	Analysis and conclusion . . . . .	103
<b>5</b>	<b>Fibre production - two stage pull</b>	<b>105</b>
5.1	Batch 1 fibres . . . . .	105
5.1.1	Velocity profile . . . . .	105
5.1.2	Fibre profiles and analysis . . . . .	107
5.1.3	Strength testing and Young's modulus . . . . .	112
5.1.4	Analysis . . . . .	115
5.2	Batch 2 fibres . . . . .	116
5.2.1	Velocity profile . . . . .	116
5.2.2	Fibre profiles and analysis . . . . .	119
5.2.3	Strength testing and Young's modulus . . . . .	123
5.2.4	Analysis . . . . .	125
<b>6</b>	<b>Conclusion</b>	<b>129</b>

# List of Tables

3.1	The FWHM obtained for the 5 different data sets that were obtained. .	63
3.2	The text file entered containing the velocity, acceleration and time values for data set 1. . . . .	68
3.3	The theoretical data for the stage's velocity, time interval, acceleration time, accumulated time and distance travelled for data set 1. Note the non-integer values for the distance travelled is due to the acceleration time being taken into account. . . . .	69
3.4	A 10 run average obtained containing the distance travelled, time interval between positions, the accumulated time and velocity values for data set 1. . . . .	69
3.5	The position readings for each entry for all 10 runs. . . . .	70
3.6	The standard deviation and largest difference value of the stage position for the 10 runs at each entry for data set 1. . . . .	71
3.7	The text file entered containing the velocity, acceleration and time values for data set 2. . . . .	73
3.8	The theoretical data for the stage's velocity, time interval, acceleration time, accumulated time and distance travelled for data set 2. . . . .	73
3.9	The text file obtained containing the distance travelled, time interval between positions, the accumulated time and velocity values for data set 2. . . . .	74
3.10	The standard deviation and largest difference value of the stage position for the 10 runs at each entry for data set 2. . . . .	75
3.11	The text file entered containing the velocity, acceleration and time values for data set 3 along with the calculated distances travelled by the stage. . . . .	76
3.12	The theoretical data for the stage's velocity, time interval, acceleration time, accumulated time and distance travelled for data set 3. . . . .	76
3.13	The text file obtained containing the distance travelled, time interval between positions, the accumulated time and velocity values for data set 3. . . . .	76
3.14	The standard deviation and largest difference value of the stage position for the 10 runs at each entry for data set 2. . . . .	78
4.1	The profiler data for a length of wire with a diameter of $25 \pm 1.25 \mu\text{m}$ . . . . .	84
4.2	The minimum values of the fibre diameters that were pulled via the absolute position method. . . . .	88

4.3	The text file entered containing the velocity, acceleration and time values for the 1 stage pull. . . . .	90
4.4	The theoretical data for the stage's velocity, time interval, acceleration time, accumulated time and distance travelled for the velocity profile. Note the predicted 40 ms delay is taken into account. . . . .	90
4.5	The minimum diameter values and length of the fibres that were pulled.	92
4.6	The text file obtained containing the 5 run average distance travelled, time interval between positions, the accumulated time and velocities values for the velocity profile. . . . .	93
4.7	The standard deviation and largest difference value of the stage position for the 5 fibres at each entry. . . . .	95
4.8	The breaking force and breaking stress values for the five fibres. . . . .	97
4.9	The Young's modulus values for the five fibres. . . . .	102
5.1	The text file entered containing the velocity, acceleration and time values for the 2 stage pull. . . . .	106
5.2	The theoretical data for the stage's velocity, time interval, acceleration time, accumulated time and distance travelled for the velocity profile. Note a 40 ms time delay is taken into account for the first entries of each stage. . . . .	107
5.3	The text file obtained containing the 5 run average distance travelled time interval between positions, the accumulated time values and velocities for the velocity profile. . . . .	109
5.4	The minimum diameter values and length of the fibres from 'Batch 1'. . . . .	109
5.5	The standard deviation and largest difference value of the stage position for the 5 fibres at each entry of 'Batch 1'. . . . .	112
5.6	The breaking force and breaking stress values for the five fibres in 'Batch 1'. . . . .	114
5.7	The Young's modulus values for the five fibres in batch 1. . . . .	114
5.8	The text file entered containing the velocity, acceleration and time values for the 2 stage pull, with the new entries in bold. . . . .	117
5.9	The theoretical data for the stage's velocity, time interval, acceleration time, accumulated time and distance travelled for the velocity profile for 'Batch 2'. Note a 40 ms time delay is taken into account for the first entries of each stage. . . . .	118
5.10	The minimum diameter values and length of the fibres from 'Batch 2'. . . . .	119
5.11	The text file obtained containing the 5 run average distance travelled, time interval between positions, the accumulated time and velocity values for the velocity profile. . . . .	121
5.12	The standard deviation and largest difference value of the stage position for the 5 fibres at each entry of 'Batch 2'. . . . .	122
5.13	The breaking force and breaking stress values for the five fibres in 'Batch 2'. . . . .	124
5.14	The Young's modulus values for the five fibres in 'Batch 2'. . . . .	125

5.15	The total measured extension values for the five fibres in 'Batch 2' at point of fibre breakage. . . . .	127
------	--	-----

# List of Figures

1.1	Illustration showing the rubber sheet like nature of space time [4]. . . .	2
1.2	Diagram showing ring of free particles illustrating the $\times$ and $+$ polarisations of gravitational waves, where the length value refers to the length of the arrows. . . . .	3
1.3	Graph of gravitational strain amplitude against source frequency [6]. . .	4
1.4	Orbital decay of PSR B1913+16 showing the observed orbital decay of the binary system agreeing with the theoretical general relativistic orbital decay [14]. . . . .	7
1.5	A diagram showing the layout of a simple Michelson interferometer. . .	10
1.6	An illustration showing the effects of a $+$ polarised gravitational wave on a Michelson interferometer. Note that change in arm length has been exaggerated for illustration purposes. . . . .	12
1.7	Aerial view of the LIGO site in Livingston, Louisiana, United States of America. . . . .	13
1.8	A diagram showing the layout of Fabry-Perot cavities in the arms of a Michelson Interferometer. . . . .	14
1.9	A diagram showing the layout of delay lines in the arms of a Michelson Interferometer. . . . .	14
1.10	A diagram showing the layout of an interferometer with Fabry-Perot cavities and power recycling. . . . .	15
1.11	A diagram showing the layout of an interferometer with Fabry-Perot cavities and signal recycling. . . . .	16
1.12	Artists impression of eLISA satellite [29]. . . . .	17
1.13	Various noise curves limiting the sensitivity of aLIGO over various frequency ranges [30]. . . . .	18
1.14	Time lapse of a surface wave travelling through the ground showing the change in the gravitational force on a suspended mass [6]. . . . .	19
1.15	Graph showing the variation in the linear spectral density of the velocity due to good and bad weather at the VIRGO site [34]. . . . .	20
1.16	The large chamber seismic isolation system that is implemented in aLIGO. Note that image has been inverted to show features [9]. . . . .	20
1.17	Graphs illustrating the fluctuation experienced with radiation pressure noise and photon shot noise respectively [36]. . . . .	22

2.1	Diagram showing two springs in parallel, one connected to a dashpot to show the anelastic properties of a material. . . . .	29
2.2	The displacement thermal noise spectra for a single aLIGO suspension [51]. . . . .	35
3.1	CAD drawing of the aLIGO pulling machine with all major components annotated [56]. . . . .	38
3.2	The suspension system that was used for LIGO and the upgraded suspensions for aLIGO [50]. . . . .	38
3.3	A fibre that was pulled from the aLIGO fibre pulling machine [50]. . . . .	39
3.4	Solidworks CAD rendering of the initial design of the small diameter silica fibre pulling machine courtesy of Liam Cunningham and Russell Jones. . . . .	41
3.5	Silica stock, highlighted in red, just before going to its molten state. . . . .	42
3.6	Silica stock once heated up to its molten state. . . . .	42
3.7	The initial setup of the small diameter silica fibre pulling machine. . . . .	43
3.8	The axicon that is attached to the backplate of the first conical mirror mount. . . . .	43
3.9	Illustration of the cylindrical beam reflecting off the second conical mirror onto the stock. . . . .	44
3.10	Illustration of the optical path for the laser beam once it reflects off the axicon. . . . .	45
3.11	Layout of the pulling machine in its current form. . . . .	46
3.12	The beam path and distribution of the beam if the beam hits the tip of the axicon at a slight angle. . . . .	48
3.13	A target plate placed after the second kinematic mirror mount used to get the beam parallel to the bench. . . . .	49
3.14	An annulus seen on a viewing screen immediately after the first conical mirror showing the desired beam distribution indicating the beam hitting the centre of the cone mirror. . . . .	50
3.15	The beam distribution in the far field indicating that the cone mirror is not perfectly perpendicular to the bench. . . . .	51
3.16	The beam distribution in the far field after a slight adjustment indicating the cone mirror is almost in the correct position. . . . .	51
3.17	Illustration of the beam path if the beam hits the cone just above the tip. . . . .	52
3.18	The ideal distribution of the beam around the silica stock. . . . .	53
3.19	A piece of silica stock that has been mis-shapen due to the clamps not being coaxial. . . . .	54
3.20	Simulated lens layout using JAMMT using $f=-100$ mm plano-concave and $f=110$ mm positive meniscus lenses with the lenses at 0.805 m and 0.930 m into the beam path and the focus at 1.155 m. . . . .	56
3.21	Data obtained from the JAMMT simulation showing the simulated beam waist of 87.26 $\mu\text{m}$ at an optical path length of 1.155 m. . . . .	57

3.22	Illustration of layout of equipment and experimental setup used to take the profile of the laser beam. . . . .	59
3.23	Three run average showing the input and output power obtained as the beam passes through the 50 $\mu\text{m}$ pinhole at the focus. . . . .	61
3.24	Three run average showing the input and output power obtained as the beam passes through the 50 $\mu\text{m}$ pinhole, -2.5 mm from focus. . . . .	61
3.25	Three run average showing the input and output power obtained as the beam passes through the 50 $\mu\text{m}$ pinhole, -5 mm from focus . . . . .	62
3.26	Three run average showing the input and output power obtained as the beam passes through the 50 $\mu\text{m}$ pinhole, +2.5 mm from focus. . . . .	62
3.27	Three run average showing the input and output power obtained as the beam passes through the 50 $\mu\text{m}$ pinhole, +5 mm from focus. . . . .	63
3.28	Simulated and experimental beam waists at the five measured positions.	64
3.29	Alternate simulation with the distance between the lenses 2 cm less than original simulation. . . . .	67
3.30	Alternate simulated and experimental beam waists at the five measured positions. . . . .	67
3.31	Distance against time for the 10 runs obtained with data set 1 . . . . .	70
3.32	The theoretical velocity profile and the 10 run average velocity profile for the pulling stage. . . . .	72
3.33	Distance against time for the 10 runs obtained with data set 2. . . . .	74
3.34	The theoretical velocity profile and the 10 run average velocity profile for the pulling stage. . . . .	75
3.35	Distance against time for the 10 runs obtained with data set 3. . . . .	77
3.36	The theoretical velocity profile and the 10 run average velocity profile for the pulling stage. . . . .	78
4.1	The silica stock being heated by the CO <sub>2</sub> laser. . . . .	82
4.2	The pulling stage beginning the pull of a fibre. . . . .	82
4.3	The fibre cartridge that is used to transport the silica fibre around the laboratory. . . . .	83
4.4	The fibre profiler used to find the width of the fibres produced. . . . .	84
4.5	Profiles of three 10 cm long fibres. . . . .	85
4.6	A zoomed in graph of the three 10 cm long fibre profiles. . . . .	85
4.7	Profiles of three 15 cm long fibres. . . . .	86
4.8	A zoomed in graph of the three 15 cm fibre profiles. . . . .	86
4.9	Profiles of three 20 cm long fibres. . . . .	87
4.10	A zoomed in graph of the three 20 cm fibre profiles. . . . .	87
4.11	The profile of 5 fibres pulled with the velocity profile in table 4.3. . . . .	91
4.12	A zoomed in image of figure 4.11. . . . .	91
4.13	Distance against time for the pulling stage for each of the five fibre entires.	94
4.14	Theoretical velocity profile and 5 run average velocity profile used to create 1 stage fibres. . . . .	94
4.15	The strength tester used to break the silica fibres. . . . .	97

4.16	The force required to break all five fibres. . . . .	98
4.17	The calculated breaking stress of all five fibres. . . . .	98
4.18	Illustration of a fibre and the central section broken down into lengths, $L_n$ , with differing diameters along the fibre. . . . .	101
4.19	Young's modulus values obtained for the five fibres. . . . .	102
5.1	Profiles of the five fibres from 'Batch 1'. . . . .	108
5.2	Close up of figure 5.1. . . . .	108
5.3	A profile of the silica stock after the first pull down for 'Batch 1'. . . . .	110
5.4	Distance against time for all 5 fibre pulls. . . . .	111
5.5	Velocity profile for the two stages for the 'Batch 1' fibres. . . . .	111
5.6	Breaking force values for all five fibres from 'Batch 1'. . . . .	113
5.7	Breaking stress values for all five fibres from 'Batch 1'. . . . .	113
5.8	Young's modulus values for all fibres from 'Batch 1'. . . . .	114
5.9	Profile of the fibres produced from 'Batch 2'. . . . .	120
5.10	Close up of figure 5.9. . . . .	120
5.11	The velocity profile used to produce the fibres in 'Batch 2'. . . . .	122
5.12	The force required to break each fibre in 'Batch 2'. . . . .	123
5.13	The breaking stress of all the fibres in 'Batch 2'. . . . .	124
5.14	Young's modulus values for all fibres from 'Batch 2'. . . . .	125
5.15	An illustration of a deformation that can occur at the end of the pulling process due to overexposure of the laser when the pulling stage is sta- tionary. . . . .	127

# Preface

This thesis is the result of a 12 month Masters of Science (by Research) project carried out with the Institute of Gravitational Research at the University of Glasgow. The project aim was to develop the small diameter silica fibre pulling machine to produce silica fibres with a width of tens of microns to be used in prototype advanced gravitational wave detectors.

Chapter one is an introduction to gravitational waves, the history behind their existence, their characteristics, sources, detectors and noise associated with the detectors. The information in this chapter is based on published literature.

Chapter two goes into detail about the thermal noise associated with ground based interferometer detectors. The information in this chapter is based on published literature.

Chapter three describes the pulling machine that was designed for this project. It goes into detail regarding the design, alignment process and future changes. The design of the pulling machine set up was carried out by Dr Alan Cummings, Dr Liam Cunningham, Dr Giles Hammond and Mr Russell Jones from the Institute for Gravitational Research. Beam profile measurements, carried out by the author, for the CO<sub>2</sub> laser that is used in the production of the fibres are shown. The characterisation of the pulling stage is shown in detail, carried out by the author.

Chapter four looks at one stage fibre pulls. Firstly, using an absolute position movement by the pulling stage where the pulling stage will accelerate to a stated

velocity to move to a position and then stop. The fibres produced were made into three batches of lengths 10 cm, 15 cm and 20 cm with each batch consisting of three fibres. Secondly, a batch of five fibres were pulled using velocity profiles. All fibres in this chapter were profiled using a fibre profiler. The batch of fibres produced with a velocity profile were then strength tested using a small fibre strength tester to find the force at which the fibre breaks, followed by calculating the Young's modulus of the fibres. All experimental work in this chapter was carried out by the author.

Chapter five looks at two stage fibre pulls. This process involves pulling the silica stock down to a smaller diameter using a velocity profile, followed by pulling the stock down to a fibre with another velocity profile. This chapter looks at two batches of fibres, each containing 5 fibres. As with the second batch of fibres in the previous chapter, the two batches of fibres were profiled and strength tested followed by calculating the Young's modulus. All experimental work in this chapter was carried out by the author.

# Acknowledgements

I would like to thank my two supervisors, Dr Giles Hammond and Prof. Sheila Rowan, for the opportunity to carry out this MSc and all their input and guidance in this project. I would also like to thank them for giving me the opportunity to present my work at the LVC meeting in Budapest, providing me with valuable experience for any presentations I may do at collaboration meetings in the future.

I would also like to thank Dr Alan Cumming, Dr Liam Cunningham and Mr Russell Jones for all their work with regards to the initial design of the pulling machine and their input to the various upgrades that were made during this thesis. Another thank you to Alan for reading and correcting numerous drafts of this thesis, that has probably driven you crazy. Also thanks to the group technicians Mr Colin Craig and Mr Stephen Craig for all their help with making components and making sure I did not lose any fingers in the workshop.

I would also like to thank my office mates in 253 for all the coffee and intellectual discussions we've had, such as what makes a salad a salad and designing an ancient Egyptian gravitational wave detector. Also thanks to everyone else in IGR for the warm welcome when I started this MSc and all the new friends I've made and I look forward to continuing working with everyone in the future during my PhD.

Finally, I would like to thank my Mum and Dad, and everyone else in my family, for all their support and motivation throughout all the years I've been in education to get me to where I am today.

# Author's Declaration

I declare that, except where explicit reference is made to the contribution of others, that this thesis is the result of my own work and has not been submitted for any other degree at the University of Glasgow or any other institution.

Karl William Toland, December 2015.

# Chapter 1

## Gravitational Waves

### 1.1 Introduction to Gravitational Waves

Albert Einstein first predicted the existence of gravitational waves in his theory of General Relativity [1], which has led to experiments designed to firstly directly detect their existence and then led to a brand new window of gravitational astronomy research. Einstein's theory combines the laws from his theory of Special Relativity [2] and Newton's laws of gravity [3]. It explains how a body can affect the curvature of spacetime and the impact it has on how gravity affects the motion of the bodies around it. An analogy for this can be seen with a simple example: Take a rubber sheet with a grid marked out on it and place a heavy sphere in the middle, illustrated in figure 1.1. The sphere will sink down, creating a curvature in the rubber sheet, which represents a two dimensional form of spacetime. A passing objects path would then be influenced by the curvature that the sphere has induced on spacetime and follow a curved path, called a geodesic, as long as there are no non-gravitational forces acting on the object.

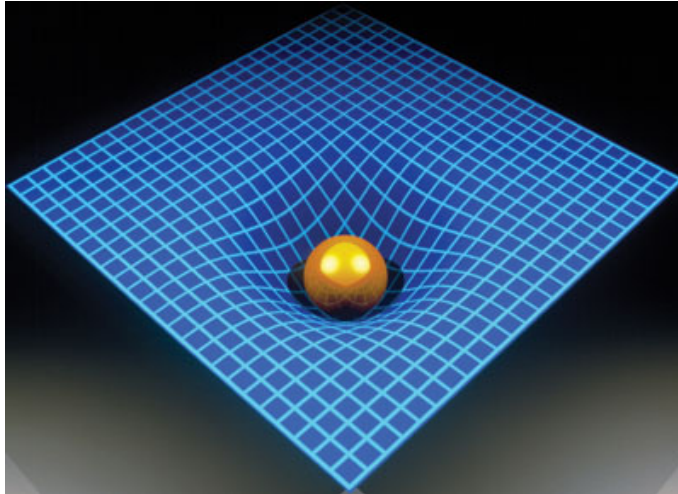


**Figure 1.1:** Illustration showing the rubber sheet like nature of space time [4].

According to General Relativity, gravitational waves are ripples in space time where energy is transported at the speed of light in the form of gravitational radiation [5]. Similar to how an accelerated electric charge generates electromagnetic waves in the electromagnetic field, an accelerated mass in space can generate gravitational waves as long as this acceleration is asymmetrical [6]. The result produces gravitational waves that are quadrupole in nature. This is due to the conservation of mass - which forbids the existence of gravitational monopoles as the mass does not change with time - and the conservation of momentum - which in turn forbids the existence of gravitational dipoles for the same reason as before. Their nature can be determined via the Quadrupole Formula, derived by Einstein [7], that can be approximated to:

$$h_{jk} = \frac{2G}{r c^4} \frac{d^2 Q_{jk}}{dt^2} \quad (1.1)$$

where  $h_{jk}$  is the gravitational wave amplitude tensor,  $r$  is the distance to the source,  $c$  is the speed of light,  $G$  is the gravitational constant and  $Q_{jk}$  is the second moment of mass distribution.

Gravitational waves come in two distinct polarisations that are orthogonal to one another:  $+$  and  $\times$ .

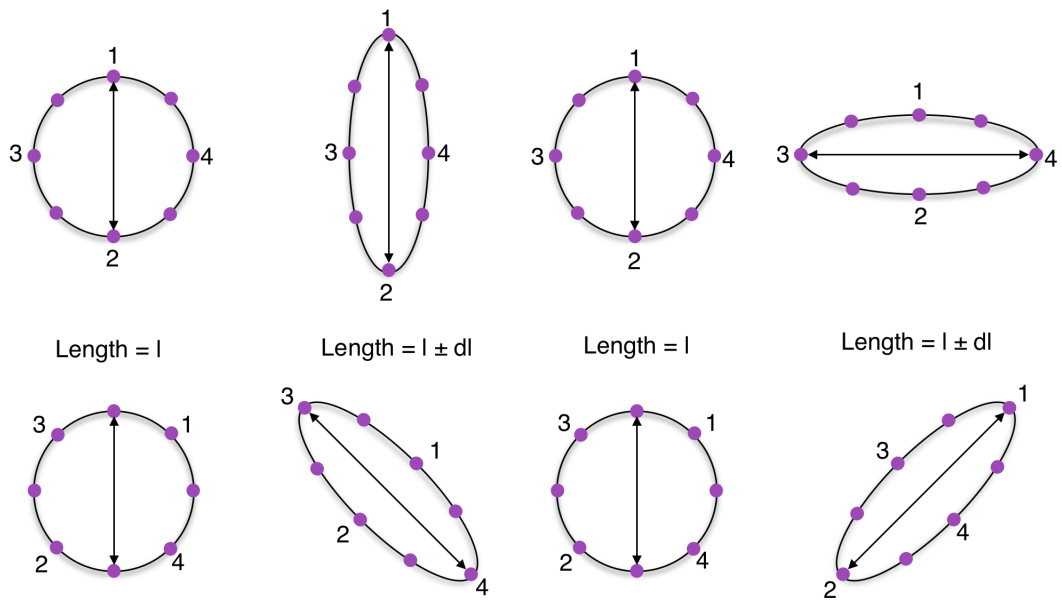


**Figure 1.2:** Diagram showing ring of free particles illustrating the  $\times$  and  $+$  polarisations of gravitational waves, where the length value refers to the length of the arrows.

Figure 1.2 illustrates the effect a passing gravitational wave would have on a ring of free particles. Take the  $+$  polarisation transition between the first two rings for example: The length change between particles one and two increases by a distance  $dl$ , while the length change between particles three and four decrease by  $dl$ . This results in a distance of  $l + dl$  between one and two and  $l - dl$  between three and four. The strain amplitude,  $h$ , of the gravitational wave is a dimensionless variable and indicates the strength of the gravitational wave signal that would be observed:

$$h = \frac{2dl}{l} \quad (1.2)$$

where  $l$  is the distance between two free particles and  $dl$  is the change in distance (sometimes written as  $\Delta l$ )

## 1.2 Gravitational Wave Sources

Of the four fundamental forces in nature, gravity is the weakest. A consequence of this is that the amplitude of gravitational waves we can detect is very small. Sathyaprakash [8] calculated the amplitude of a gravitational wave should one generate one in a laboratory. His example gave an amplitude of  $\approx 5 \times 10^{-43}$  and a frequency of 20 Hz for two  $10^3$  kg masses on a 10 m rod. Considering current gravitational wave detectors, the Advanced Laser Interferometer Gravitational wave Observatory (aLIGO) [9], for example, have a sensitivity to around  $10^{-23}$  in the frequency band of a few hertz to kilohertz, it is clear that our best chances of detecting gravitational waves directly must come from massive astronomical sources, in particular, burst sources and periodic sources. Figure 1.3 [6] shows a variety of gravitational wave sources that detectors are hoping to observe showing the projected order of magnitude and frequency of the sources.

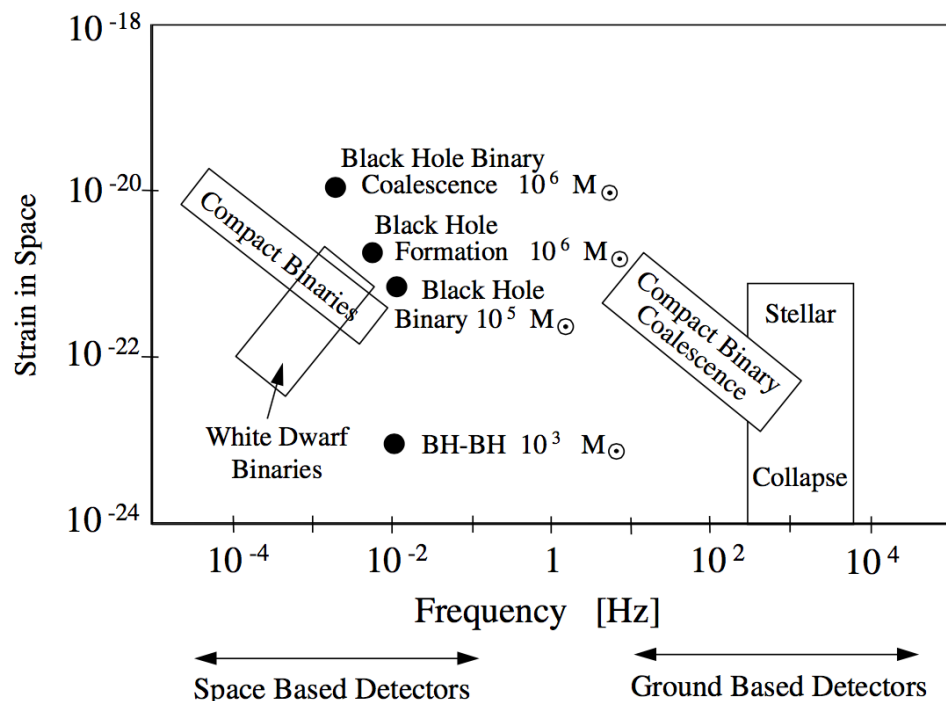


**Figure 1.3:** Graph of gravitational strain amplitude against source frequency [6].

### 1.2.1 Burst Sources

When gravitational radiation is emitted once over a short timescale, the likely source of this is would be from events such as supernovae and coalescing binary star systems. These are what are known as burst sources.

#### Supernovae

As stated previously, it is known that gravitational waves can only be emitted from sources if there is an asymmetrical acceleration involved. This is the case when it comes to core-collapse supernovae, such as type II supernovae, which can be considered to be a burst source. Where the core mass is greater than the Chandrasekhar limit,  $1.44 M_{\odot}$ , a type II supernovae [10] will result from the star collapsing under gravity when the outwards force from the fusion of elements can no longer counteract the force of gravity. Having the core mass greater than the Chandrasekhar limit overcomes the electron degeneracy pressure to allow neutrons to form from the combination of electrons and protons in the core.

When the star is unable to produce enough energy to counteract the force of gravity, the star collapses until neutron degeneracy pressure brings the collapse to a halt. This collapse is due to the fact that it takes more energy to fuse two iron atoms together than what is produced. The star is therefore not able to use the iron produced as a source of fuel. The sudden stop when the collapse comes to a halt causes a rebound shockwave that results in the outward explosion of the stellar matter. The remnant from this explosion is a neutron star, unless the star has a sufficiently large enough mass to overcome the neutron degeneracy pressure, in which case the end outcome is a black hole.

Sathyaprakash [8] gave an approximation of the possible amplitude of a gravitational wave that would be observed with instruments on the ground. He states that taking a supernova with a timescale of 1 ms in the Milky Way at a distance of 10 kpc, that

has a radiating energy equivalence of  $10^{-7} M_{\odot}$  at a frequency of 1 kHz, the amplitude that would be observed would be:

$$h \approx 6 \times 10^{-21} \left( \frac{E}{10^{-7} M_{\odot}} \right)^{\frac{1}{2}} \left( \frac{1ms}{T} \right)^{\frac{1}{2}} \left( \frac{1kHz}{f} \right) \left( \frac{10kpc}{r} \right) \quad (1.3)$$

where  $E$  is the mass/energy that has been converted into gravitational waves,  $T$  is the timescale of the collapse,  $f$  is the frequency of emission and  $r$  is the distance to the source. This approximation shows that even for events such as supernovae, the amplitude of gravitational waves that would be detected by detectors is still incredibly small.

### **Coalescing compact binary star system.**

Compact binary star systems come in three different pairings:

- Neutron star/neutron star
- Neutron star/black hole
- Black hole/black hole

As the stars orbit around a common centre of mass, the bodies will be gravitationally attracted to each other. This attraction results in the system radiating energy away in the form of gravitational radiation where the loss of energy decreases the orbital period of the two stars. A considerable emission of gravitational waves is predicted to be detectable with ground based detectors in a lower frequency range than supernovae, during the final stages of the stars prior to and at the moment they coalesce [11]. In a paper published in 1975 [12], a pulsar, named PSR B1913+16, was discovered by R. A. Hulse and J. H. Taylor where two neutron stars were orbiting a common centre of mass; a binary system. Further study of the system [13] indicated that the pair of stars were coalescing, with the orbital period decreasing over time in agreement with

calculated predictions using general relativity, as seen in figure 1.4 [14].

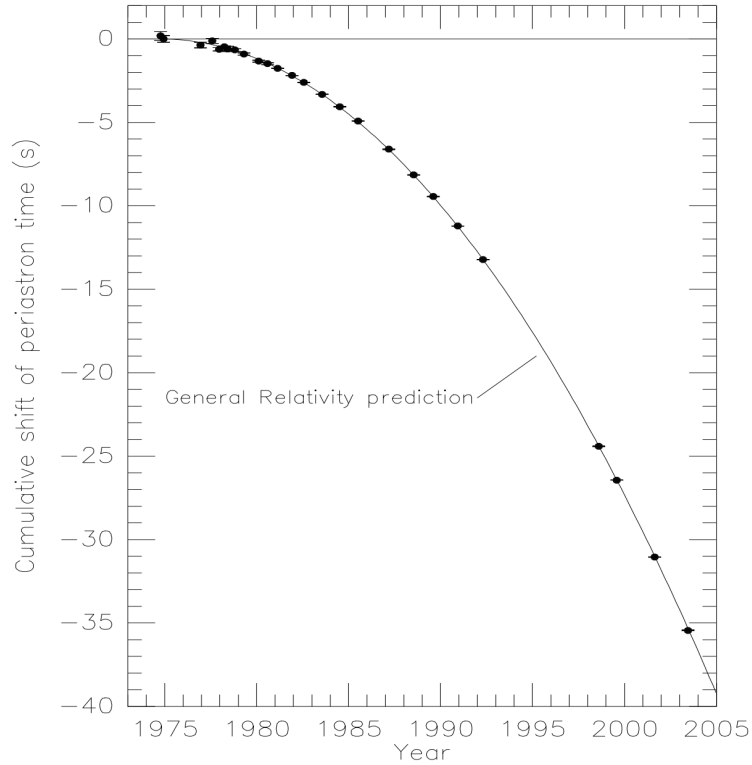


**Figure 1.4:** Orbital decay of PSR B1913+16 showing the observed orbital decay of the binary system agreeing with the theoretical general relativistic orbital decay [14].

The fact that the orbital period is decreasing showed that the system is losing energy, therefore there must be energy radiated out from the system. This radiated energy was then deduced to be gravitational radiation, thus providing the first indirect evidence of the existence of gravitational waves. This discovery led to Hulse and Taylor receiving a Nobel Prize in 1993 for their work. The amplitude that would be observed for a neutron star neutron star binary can be calculated via [15]:

$$h \approx 1 \times 10^{-23} \left( \frac{100 Mpc}{r} \right) \left( \frac{M_B}{1.2 M_\odot} \right)^{\frac{5}{3}} \left( \frac{f}{200 Hz} \right)^{\frac{2}{3}} \quad (1.4)$$

where  $r$  is the distance to the source,  $M_B = \frac{(M_1 M_2)^{\frac{3}{5}}}{(M_1 + M_2)^{\frac{1}{5}}}$ ,  $M_1$  and  $M_2$  are the masses of the two stars in the binary system and  $f$  is the frequency of the gravitational

wave. Referring to figure 1.3, one can see that for binary neutron star coalescence, the observation frequency ranges from around 10 Hz to just over  $10^3$  Hz which is in the frequency band of ground based detectors. However, for binary black hole coalescence, the observational frequency drops to the order  $10^{-3}$  Hz indicating that these are most likely to be observed with space interferometers.

### 1.2.2 Periodic Sources

As the name suggests, periodic sources are sources that will produce gravitational waves periodically. An example of this are pulsars. If the neutron star has an asymmetric mass distribution, due to accretion of mass from another star or large bumps on the surface, gravitational waves will be produced. If the neutron star was perfectly symmetrical, then it would be able to rotate on its axis perfectly preventing any gravitational waves being produced. The asymmetry however allows the star to rotate off its axis resulting in the production of gravitational waves. The wave amplitude for a neutron star with a standard mass and moment of inertia can be calculated via [16]:

$$h \approx 6 \times 10^{-25} \left( \frac{f_{rot}}{500Hz} \right)^2 \left( \frac{1kpc}{r} \right) \left( \frac{\epsilon}{10^{-6}} \right) \quad (1.5)$$

where  $f_{rot}$  is the rotational frequency of the neutron star,  $r$  is the distance to the source,  $\epsilon$  is the ellipticity of the neutron star.

Another source is the stochastic background radiation which is a superposition of unresolved and uncorrelated random events. One detector alone would not be able to distinguish the stochastic background, but combining two or more detectors would allow the possibility of getting the appropriate data [17].

## 1.3 Instruments used to detect gravitational waves

Current ground based detectors are based around two different designs: Resonant bars and Michelson interferometers.

### 1.3.1 Resonant Bars

One of the first experiments to prove the existence of gravitational waves was led by Joseph Weber of the University of Maryland. He proposed having an aluminium cylinder at sites separated by a large distance, in this case 1000 km between Maryland and Chicago, that would resonate within a narrow frequency band. Piezoelectric crystals attached to the detector would convert this resonance to an electrical signal [18] [19]. Having a resonant cylinder at two separate sites allows coincident events to be recorded to help confirm that a signal had indeed been detected and was not just a noise signal. These bars would be named after Weber and are known as “Weber bars”. Weber soon published his findings [20], in one instance claiming to have recorded 17 significant two detector coincidences in an 81 day period, thus proving experimentally the existence of gravitational waves. However, his excitement was short lived as replica experiments were conducted by other research groups that failed to observe any signals [21]. Resonant bars are still used for current research, mainly with cryogenically cooled bars to a few Kelvin such as AURIGA [22].

### 1.3.2 Ground Based Laser Interferometers

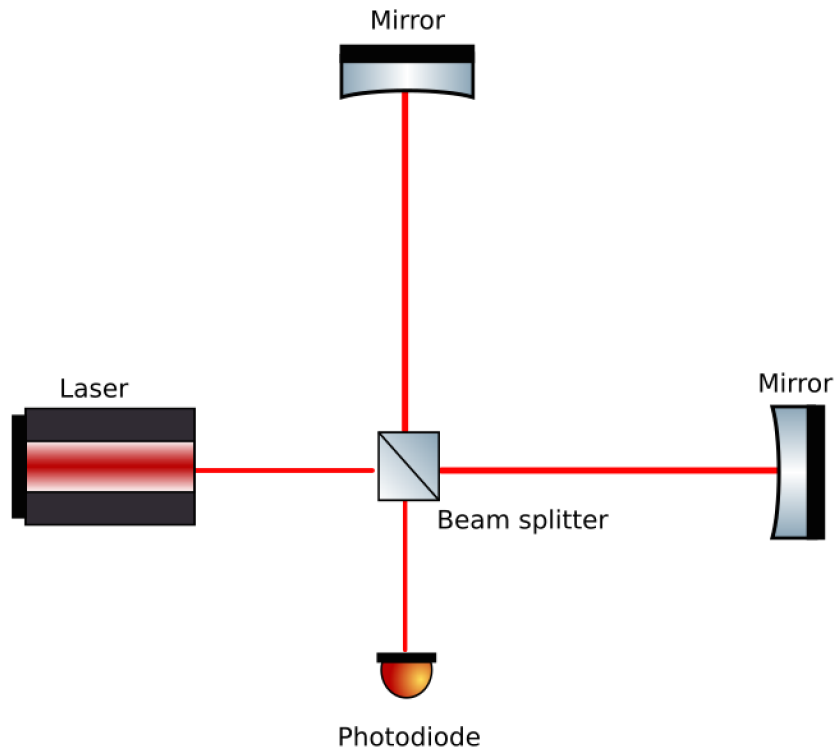


**Figure 1.5:** A diagram showing the layout of a simple Michelson interferometer.

Michelson interferometers are used as a base design for several observatories, such as the Laser Interferometer Gravitational-Wave Observatory (LIGO) [23] in the United States of America, VIRGO [24] in Italy and GEO600 [25] in Germany. As of October 2015, these detectors have gone through various upgrades and they are reaching their second generation performance level, Advanced VIRGO (AdV) [26] and GEO High Frequency (GEO-HF) [27], whereas Advanced LIGO (aLIGO) has completed all its upgrades and is now online in its first operating run [9].

The basic design of an interferometer has a laser beam going through a beam splitter to two suspended mirrors placed at a specified distance away perpendicular to each other. The beams are then reflected from the mirrors, recombining at the beam splitter where a photodiode detector will read out the interference pattern. The idea behind the use of interferometers as gravitational wave detectors comes from the

concept that as a gravitational wave would pass by, there would be a differential change in arm lengths leading to an observed change in the interference pattern generated, as illustrated in figure 1.6. The mirrors reflecting the laser beam would be fixed in place such that the point on the interference pattern is close to a dark fringe. Holding the mirrors in place is achieved via the use of transducers being fed back information from the photodiode at the output to adjust the position of the mirror and is known as “locking”.

It is favourable to have long arm lengths when detecting small signals since  $dl$  is larger. An interferometer is at peak sensitivity when the time it takes for the beam to leave the beam splitter, reflect off the end mirror and recombine back at the beam splitter is half the period of a gravitational wave. This scenario results in the mirrors being at a maximum displacement due to the nature of the gravitational wave’s quadrupole nature. Consider the following example: For a gravitational wave of frequency 100 Hz, the period of the wave would be  $1 \times 10^{-2}$  seconds. This means that the maximum displacement will occur at  $0.5 \times 10^{-2}$  seconds. The optimum arm length can then be calculated via

$$L = \frac{vt}{2} \tag{1.6}$$

where  $v = c$ ,  $t = 0.5 \times 10^{-2}$  seconds and the division by 2 to give the arm length as opposed to the total distance the beam travels in the arm. This results in an optimal arm length of 750,000 m (11% of the Earth’s radius) for a 100 Hz gravitational wave which is not practically possible on Earth due to its curvature and the need for the beam to travel in a straight line. For example, LIGO has two interferometers of arm length 4 km, VIRGO 3 km arms and GEO with 600 m arms.

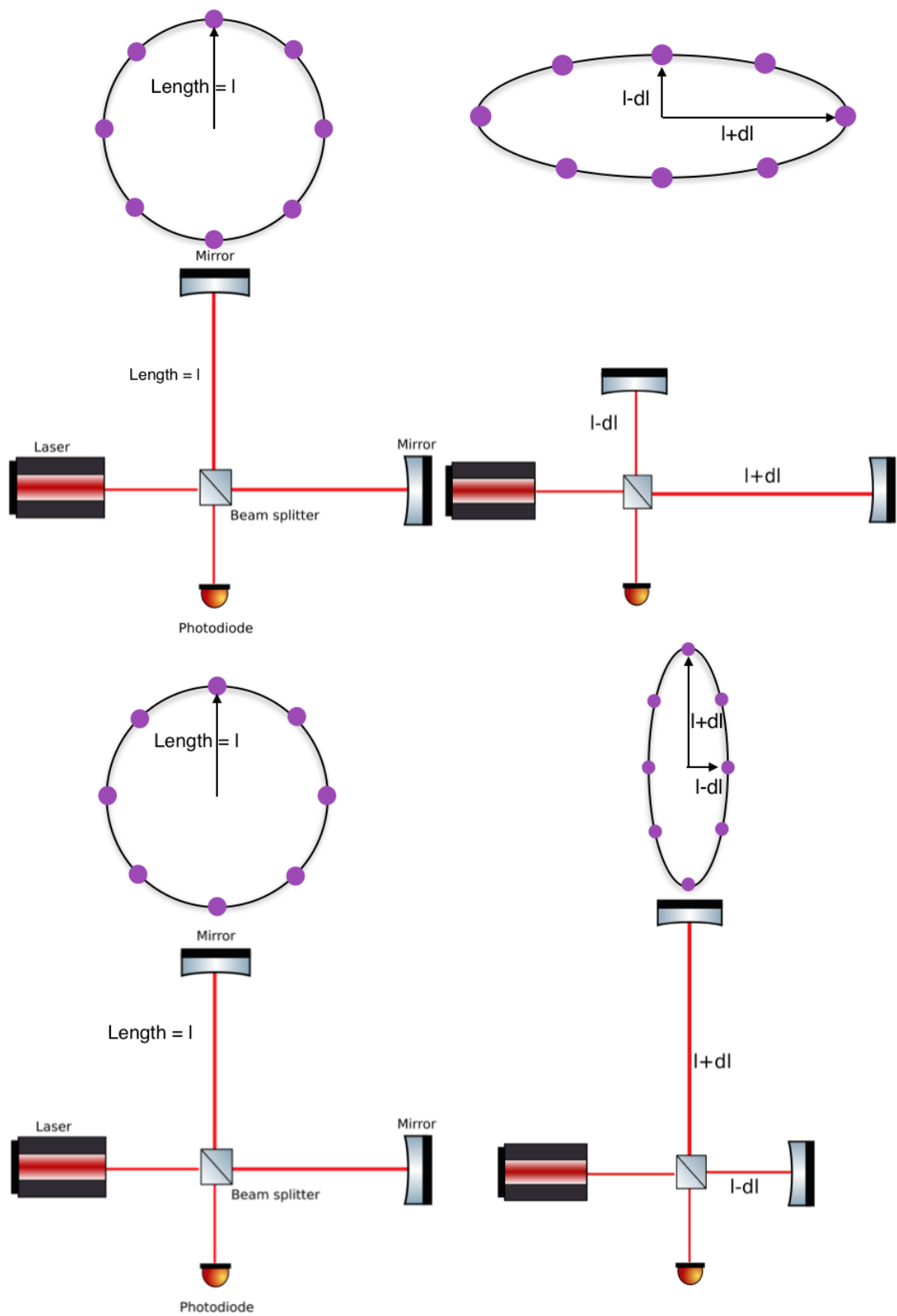


**Figure 1.6:** An illustration showing the effects of a + polarised gravitational wave on a Michelson interferometer. Note that change in arm length has been exaggerated for illustration purposes.



**Figure 1.7:** Aerial view of the LIGO site in Livingston, Louisiana, United States of America.

It is possible however to increase the effective arm length to contain the beam in the arms of the interferometer resulting in the beam being stored for half the period of a gravitational wave through the use of Fabry-Perot Cavities and delay lines [6]. Fabry-Perot cavities, as shown in figure 1.8, are cavities in the arms of the interferometers using highly reflective mirrors, one of which that transmits a small amount of the laser beam. For the cavities to work, they must be locked at a resonance where the length of the cavity is an integral number of the laser's wavelength to allow the energy in the cavity to build up. The cavity is locked via the use of control systems altering the position of one of the mirrors in each arm.

Increasing the storage time through the use of delay lines, see figure 1.9, is achieved by using pairs of mirrors designed to reflect the beam back and forth, thus increasing the time the beam is in the arm until it reaches the photodiode for detection. The beam enters the cavity through a hole in the first mirror and is reflected back and forth along the mirror until it exits to the output detector. Bigger mirrors are needed however compared to the Fabry-Perot cavities due to the fact that the beam does not reflect back on top of itself, whereas with Fabry-Perot cavities, smaller mirrors can be used as the beam reflects on itself.

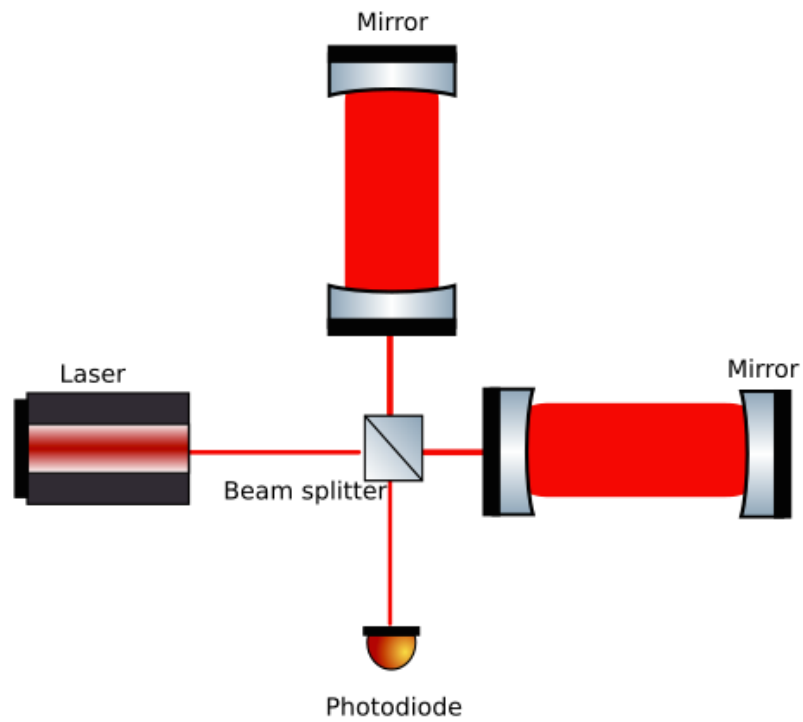


**Figure 1.8:** A diagram showing the layout of Fabry-Perot cavities in the arms of a Michelson Interferometer.

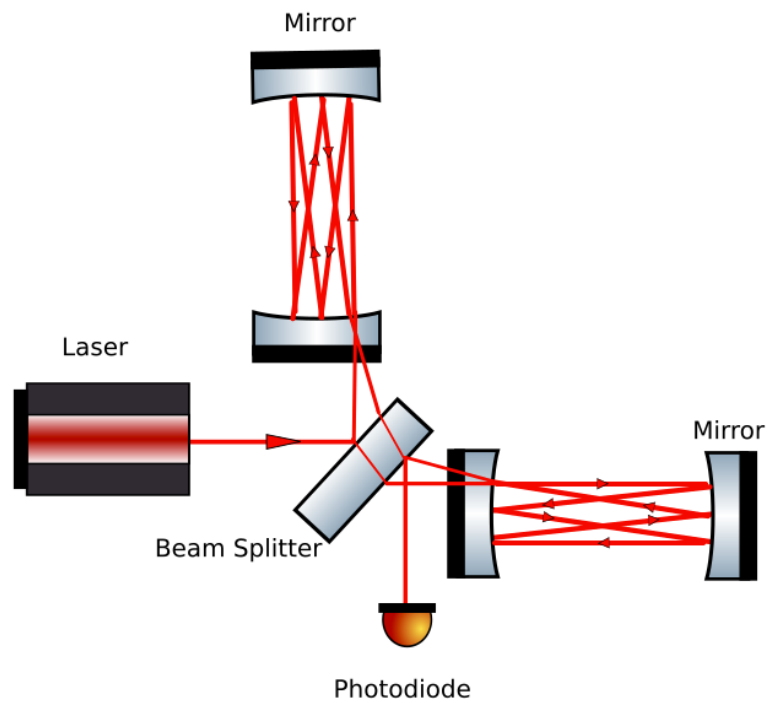


**Figure 1.9:** A diagram showing the layout of delay lines in the arms of a Michelson Interferometer.

The use of Fabry-Perot cavities and delay lines to increase the effective arm length of the interferometer and increase instrument sensitivity can also be improved via the use of power recycling [6], figure 1.10 and signal recycling [6], figure 1.11. Power recycling is based on the concept that locking the interferometer near a dark fringe results in the vast majority of the beam being reflected back to the laser source. Therefore placing a mirror in between the beam splitter and the laser to reflect the beam that is heading back will then result in the number of photons in the interferometer to increase, thus increasing the total power of the laser beam without physically increasing the power of the laser itself. Signal recycling works in the same manner, except that a mirror is placed in front of the photodiode to reflect the sidebands back into the arms of the interferometer. This is beneficial when trying to observe a source in a narrow bandwidth as the placement of the mirror will allow the interferometer to be tuned in and therefore more sensitive in that chosen bandwidth.

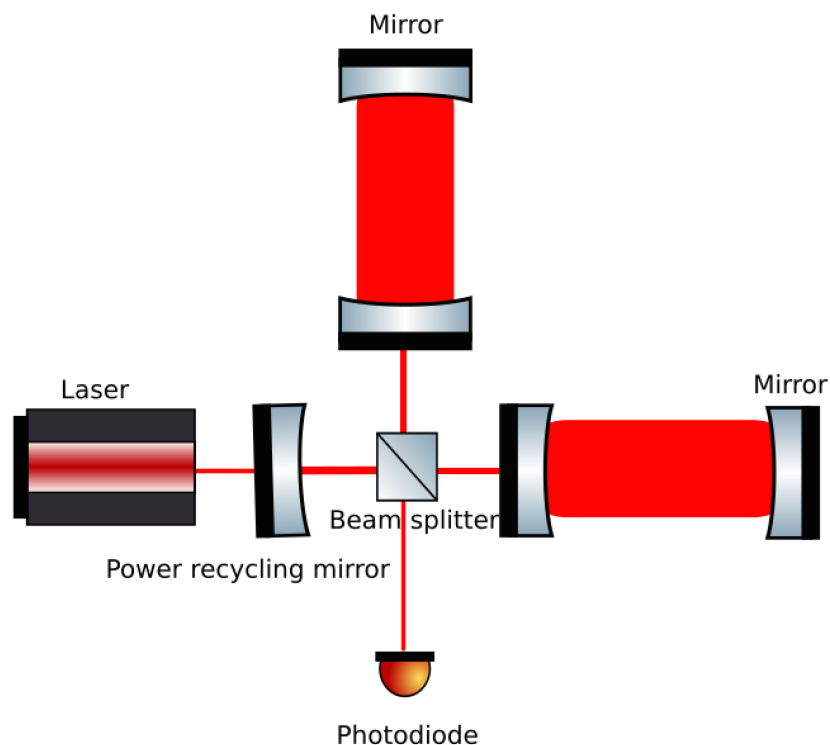


**Figure 1.10:** A diagram showing the layout of an interferometer with Fabry-Perot cavities and power recycling.

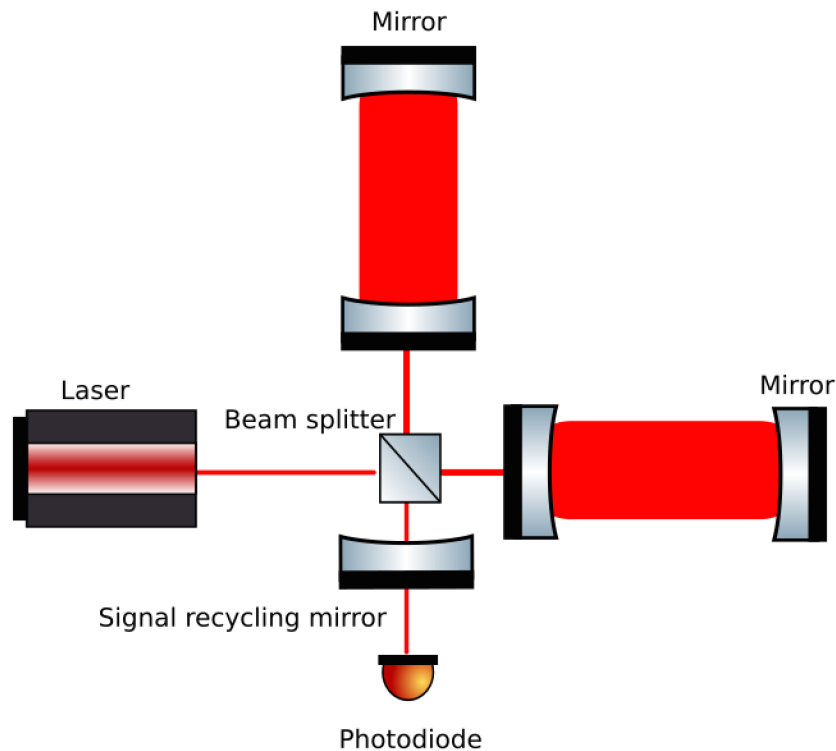


**Figure 1.11:** A diagram showing the layout of an interferometer with Fabry-Perot cavities and signal recycling.

### 1.3.3 Space Based Laser Interferometers

The Evolved Laser Interferometer Space Antenna (eLISA) [28] is currently under development by the European Space Agency (ESA) with aims to operate at frequencies below 1 Hz. eLISA will consist of three satellites, one ‘mother’ and two ‘daughter’ satellites. This will make up an equilateral triangle with arm lengths of approximately  $1 \times 10^9$  m following the Earth’s orbit around the Sun, trailing the Earth by  $20^\circ$  and a  $60^\circ$  inclination to the ecliptic. Inside the satellites, there will be free falling masses that are held in place via the use of sensors and thrusters to counteract any external forces the masses may experience, while the space craft also acts as a shield to protect them.

At the moment of writing this thesis, LISA Pathfinder is due to launch in November 2015. LISA Pathfinder will test various components and concepts associated with the

final design of eLISA, such as the behaviour of the free floating test masses and other aspects that are not testable on Earth.

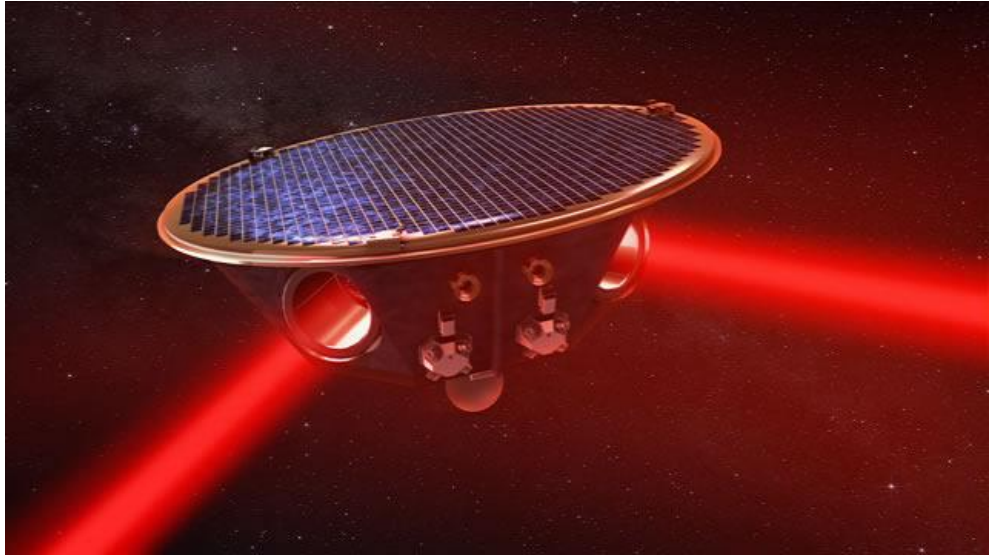


**Figure 1.12:** Artists impression of eLISA satellite [29].

## 1.4 Noise Sources

When trying to observe signals with amplitudes below the order of  $10^{-20}$  for ground based observations, limiting the amount of noise present in the detectors is a key priority to maximise sensitivity. Figure 1.13 [30] is a graph showing various noise sources that are taken into account for aLIGO. It shows that some noises only affect observations within a small frequency band and noise sources that affect a wide range of frequencies. A selection of dominant noise sources associated with ground based interferometers will be discussed in this section.

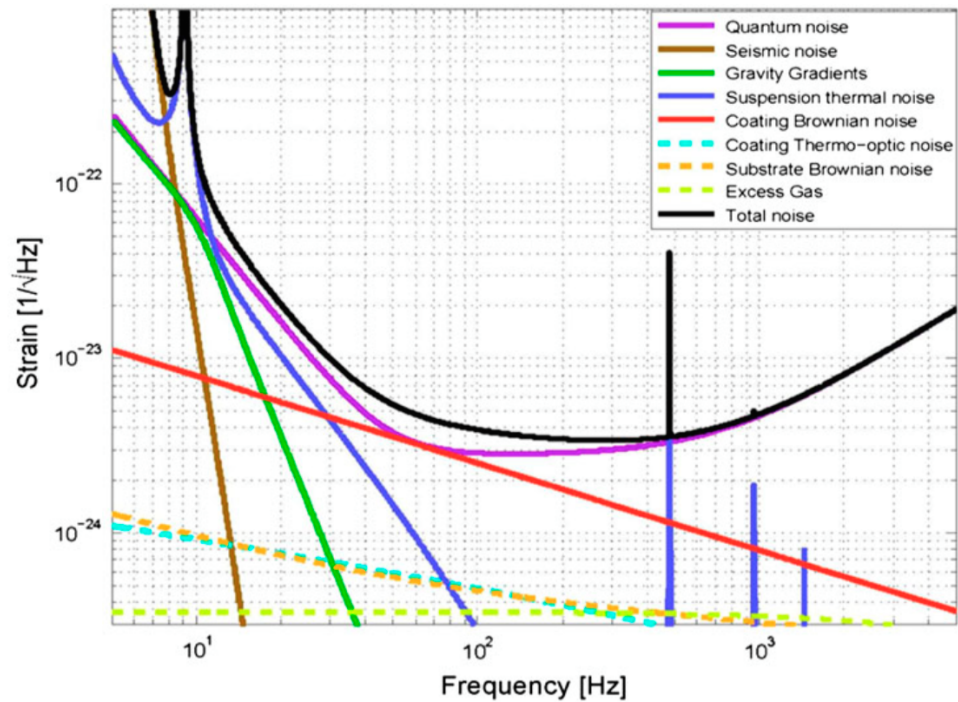


**Figure 1.13:** Various noise curves limiting the sensitivity of aLIGO over various frequency ranges [30].

### 1.4.1 Gravity Gradient Noise

Gravity gradient noise arises from the gravitational interaction between the test masses at the end of the interferometer arms and moving masses in the environment and can not be shielded against. Moving masses can include near by vehicles, clouds, air pressure changes, seismic surface waves etc which provides a problem when detectors are at ground level. Seismic surface waves, illustrated in figure 1.14 [6], cause density fluctuations in the Earth's surface, which if occurring near the interferometer, can influence the position of the test mass in the arm. Gravity gradient noise affects low frequencies placing a lower limit of source observation to around 10 Hz [31].

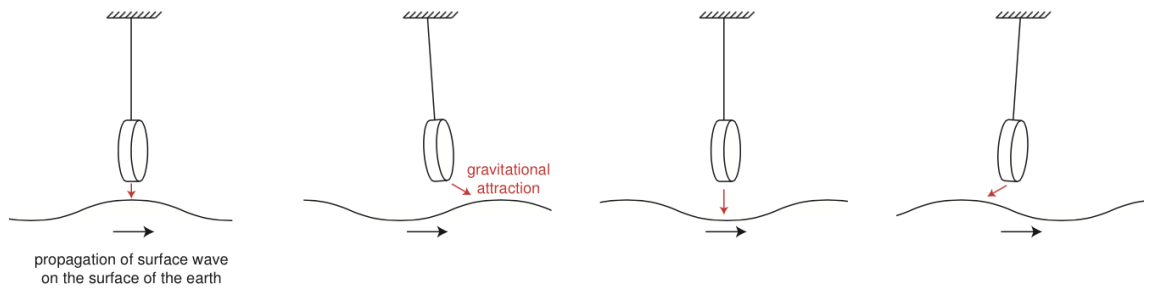


**Figure 1.14:** Time lapse of a surface wave travelling through the ground showing the change in the gravitational force on a suspended mass [6].

Research shows [32] that surface waves decrease exponentially with depth, indicating that future generation gravitational wave detectors will be built underground to help decrease the lower observation limit to below 1 Hz [33]. The other option to going underground to nullify gravity gradient noise would be to go into space, as LISA is planned to do.

### 1.4.2 Seismic Noise

Seismic noise also dominates in the low frequency region. Seismic noise can arise via several sources such as human activities, turbulent weather which can result in significant variations between good and bad weather, as illustrated in figure 1.15 [34]. The large variation that can be seen below 1 Hz is due to the sea activity and the variation close to 10 Hz is due to the resonances of the benches in the interferometer. At a reasonably quiet site, seismic noise follows an acceleration spectral density around  $10^{-7} f^{-2} \text{ mHz}^{-\frac{1}{2}}$  [35]. Consider the following example [35]: For  $f = 30 \text{ Hz}$ , if the disturbance to each test mass must be smaller than  $3 \times 10^{-20} \text{ mHz}^{-\frac{1}{2}}$ , then the reduction of seismic noise needed is greater than  $10^9$  in the horizontal direction, which couples with the vertical direction, due to cross coupling at the level of  $10^{-3}$ .

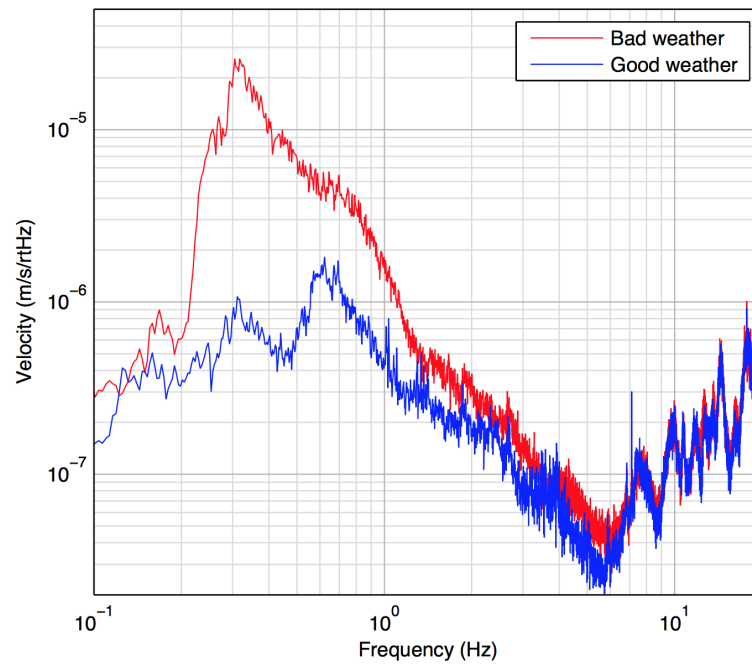


**Figure 1.15:** Graph showing the variation in the linear spectral density of the velocity due to good and bad weather at the VIRGO site [34].

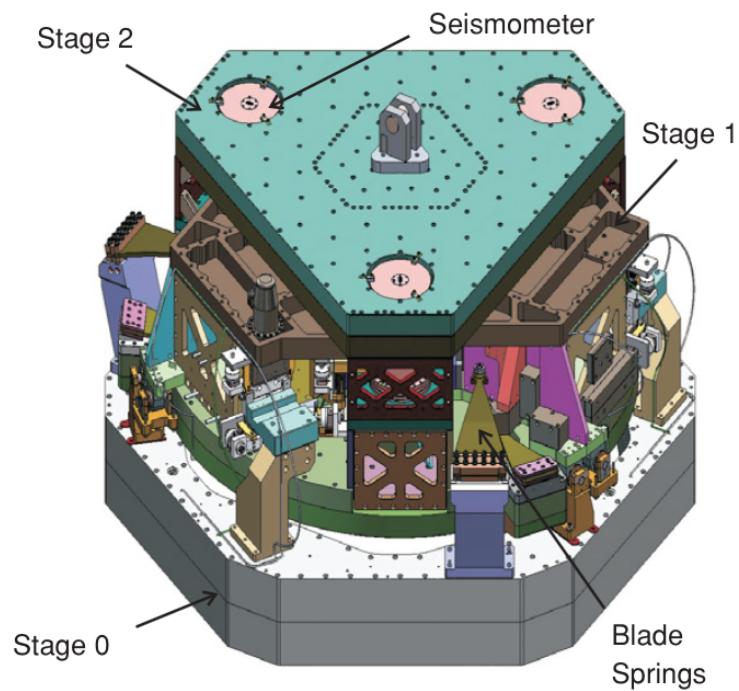


**Figure 1.16:** The large chamber seismic isolation system that is implemented in aLIGO. Note that image has been inverted to show features [9].

To isolate the test masses from seismic noise, the test masses must be suspended via the use of pendulums to combat the horizontal component and cantilever springs for the vertical component. The use of pendulums exploits the fact that the transfer function of a pendulum for the horizontal motion of the test mass follows  $\frac{1}{f^2}$  when above the pendulum's resonance frequency [6]. Consider a test mass,  $m$ , attached to a spring with spring constant,  $k$ , and damping constant  $b$ . Looking at the transfer function between the ground motion,  $x_g$ , and the motion of the test mass,  $x_m$ , one gets:

$$\frac{x_m}{x_g} = \frac{\omega_0^2}{\sqrt{(\omega_0^2 - \omega^2)^2 + \omega^2\gamma^2}} \quad (1.7)$$

where  $\omega_0$  is the resonant angular frequency equal to  $\sqrt{\frac{k}{m}}$  and  $\gamma$  is a constant equal to  $\frac{b}{m}$  [30]. One can see at low frequencies,  $\frac{x_m}{x_g} \approx 1$  resulting in the pendulum acting as one system and at high frequencies,  $\frac{x_m}{x_g} \approx \frac{\omega_0^2}{\omega^2}$  resulting in a small transfer of motion to the test mass. The same applies for the use of cantilever springs to isolate from the vertical component. Together one can make passive and active seismic isolation stages. aLIGO for example utilises a four stage system, the first two illustrated in figure 1.16 [9] and VIRGO a seven stage horizontal pendulum system [35].

### 1.4.3 Quantum Noise

One of the main contributors to noise over a wide range of frequencies that gravitational wave detectors are aiming to observe is the noise that is associated to the quantum nature of photons, called quantum noise. There are two main sources of quantum noise, photon shot noise and radiation pressure noise which together creates the Standard Quantum Limit.

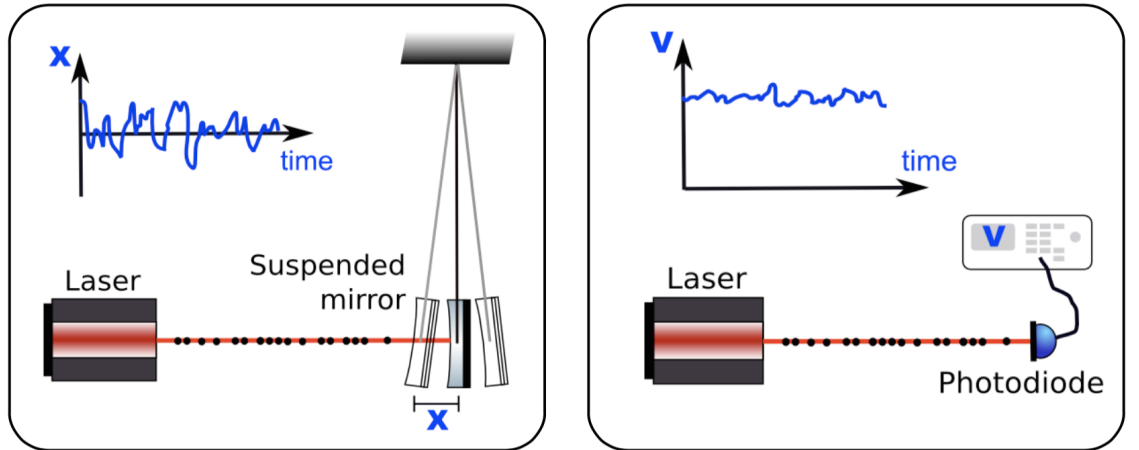


**Figure 1.17:** Graphs illustrating the fluctuation experienced with radiation pressure noise and photon shot noise respectively [36].

Photon shot noise arises from the distribution of the photons from the laser not being equal over time, but in fact following a Poisson statistic, affecting the sensitivity of the optical readout scheme. The uncertainty in the number of photons,  $N$ , within a time,  $T$ , is therefore  $\sqrt{N}$ . As mentioned previously, interferometer end test masses are locked such that the interference pattern would be close to a dark fringe, so that the majority of the laser beam is reflected back towards the laser, but reflected off the power recycling mirror. This results in the noise at the photodiode being at a minimum to give an ideal signal to noise ratio. The amplitude spectral density of the shot noise can be calculated via [36]:

$$h_{sn} = \frac{1}{L} \left[ \frac{\lambda h c}{\pi^2 P} \right]^{\frac{1}{2}} \text{Hz}^{-\frac{1}{2}} \quad (1.8)$$

where  $h_{sn}$  is the amplitude spectral density for shot noise,  $L$  is the arm length,  $\lambda$  is the wavelength of the laser,  $h$  is Planck's constant,  $c$  is the speed of light and  $P$  is the laser power. A calculation [6] shows that since the strains that ground based interferometers are hoping to observe are of the order  $10^{-23} \text{ Hz}^{-\frac{1}{2}}$ , using a laser with  $\lambda = 10^{-6} \text{ m}$  and assuming a quantum efficiency  $\approx 1$  for the photodiode, would require a laser power of the order  $10^6 \text{ W}$ . This can be achieved via methods described previously, such as the use of Fabry-Perot cavities. aLIGO for example has a circulating power of 800 kW,

AdV has a circulating power of 700 kW, GEO-HF has a circulating power of 20 kW and KAGRA has a circulating power of 400 kW [37].

Radiation pressure noise arises due to the fact that photons transfer some of their momentum to the mirror from which they are reflected, thus applying a force causing a positional change to the mirror. However, as mentioned previously, the photon distribution follow a Poisson distribution, this results in a fluctuation of the applied force on the mirror resulting in a fluctuation in the mirror position. Unlike photon shot noise, should the laser power increase, the radiation pressure too would increase, due to the increase in the number of photons reflecting off the mirror transferring their momentum. The fluctuation in position is explained by Caves [38] in terms of vacuum (zero-point) fluctuations in the electromagnetic field. Assume that light were to enter the interferometer from the output photodiode, that then interacts with the beam splitter. The light could then affect the intensity in the arms of the interferometer if the light had a specific phase. It would result in increasing intensity in one arm of the interferometer and decreasing intensity in the other simultaneously. Since physically there is no light source from this output, one can apply this logic to the case of vacuum fluctuations incident from the output. Superposing the vacuum fluctuations with the photons from the laser results in the  $\sqrt{N}$  fluctuating force. The amplitude spectral density for the radiation pressure can be calculated via [36]:

$$h_{rp} = \frac{1}{mf^2L} \left[ \frac{\hbar P}{2\pi^3 c \lambda} \right]^{\frac{1}{2}} Hz^{-\frac{1}{2}} \quad (1.9)$$

where  $h_{rp}$  is the amplitude spectral density of the radiation pressure,  $m$  is the mass of the mirror,  $f$  is the frequency,  $\hbar$  is the reduced Planck constant and the remaining symbols hold previous meaning. This formula shows that an increase in the power will result in a increase in radiation pressure but this could be counteracted via the use of heavier test masses.

This is analogous to the Heisenberg Uncertainty Principle; Increasing the optical power to increase the sensitivity at high frequencies due to the decrease in photon shot noise will in turn decrease the sensitivity at low frequencies due to the increase in radiation pressure noise and vice versa. This places a limit to the sensitivity of the classical interferometer, known as the Standard Quantum Limit (SQL). There are experiments that aim to reach a sensitivity below the SQL, such as the 10 m interferometer at the Albert Einstein Institute in Hannover [39] and the Sagnac speed meter interferometer that is being developed in Glasgow [40]. Measurements below the SQL however can be achieved via the use of techniques such as detuned signal recycling and quantum non-demolition configurations [41].

#### 1.4.4 Thermal Noise

Thermal noise is an important source of noise that is dominant at low frequencies,  $\leq 100$  Hz, and is mainly associated with the interferometer test masses and suspensions. It results from the statistical movement of atoms due to the thermal energy that each atom has. This thermal energy is explained by Einstein [42] where a particle has  $\frac{1}{2}k_B T$  energy per degree of freedom in the system, where  $k_B$  is the Boltzmann's constant and  $T$  is the temperature.

This noise source will be discussed in detail in the following chapter.

## 1.5 Work at Glasgow

The Institute of Gravitational Research (IGR) based at the University of Glasgow plays a major part in the research efforts towards the detection of gravitational waves. A collaboration between Glasgow, Cardiff University, the Albert-Einstein Institute Hannover and the Albert Einstein Institute Golm resulted in the GEO 600 interferometer where IGR focused on the development of the pendulum systems for the test masses for low

---

mechanical loss in the suspensions, coatings and hydroxy-catalysis bonding. Glasgow, also collaborates with the University of Birmingham, Cardiff University, University of Sheffield and the Rutherford Appleton Laboratory in providing the mirror suspensions and optics for the aLIGO detectors. The University of Glasgow also plays a key role in the eLISA developing the flight hardware optical bench.

# Chapter 2

## Thermal Noise

### 2.1 Introduction

Reducing the thermal noise in ground based interferometers has been an area of ongoing research for many years. It is one of the main noise source with regards to the test masses and their suspensions that is due to the statistical movement of atoms from the thermal energy that each atom possesses, known as Brownian motion. Thermal noise is dominant at frequencies  $\leq 100$  Hz as well as at certain high frequencies, the resonant modes of the mirror and the violin modes of the suspension.

Robert Brown, a Scottish botanist, documented the random motions of pollen grains that were floating in water that he observed [43], later named Brownian motion. This random motion was explained by Einstein [42] where he found that the pollen grains were actually interacting with the water molecules that were driven thermally. As the pollen moves through the water, the pollen will experience fluid resistance. This resistance dissipates the pollen's kinetic energy which results in the water molecules becoming thermally influenced. The random motion was caused from the fluctuation in the number of collisions that would occur between the water molecules and the pollen grains. This theory would later be known as the Fluctuation-Dissipation theorem [44], which states that a linear system that is in thermal equilibrium can be expressed in

terms of the fluctuation the system experiences and the dissipation.

The Fluctuation-Dissipation theorem can be expressed as [45]:

$$S_f(\omega) = 4k_B T \Re[Z(\omega)] [N^2 Hz^{-1}] \quad (2.1)$$

where  $S_f(\omega)$  is the power spectral density of the thermal driving force,  $k_B$  is the Boltzmann constant,  $T$  is the temperature and  $\Re[Z(\omega)]$  is the real part of the mechanical impedance of the system, known as the dissipation where

$$Z = \frac{F}{v} \quad (2.2)$$

where  $F$  is the applied force and  $v$  is the velocity. Equation 2.1 can be re-arranged to include the admittance,  $Y$ , and express the power spectral density for displacement:

$$S_x(\omega) = \frac{4k_B T}{\omega^2} \Re[Y] [m^2 Hz^{-1}] \quad (2.3)$$

## 2.2 Suspension thermal noise

### 2.2.1 Sources of dissipation

In gravitational wave interferometer's test masses and its suspensions, there are two sources of dissipation to consider: external and internal.

#### External Sources

External dissipation results in the loss of energy to the surrounding environment. There are several possible sources of external dissipation in the test masses and its suspensions:

- Gas/viscous damping. This occurs from collisions with any gas molecules that are left in the suspension system after it has been evacuated.

- The motion of the test mass can give rise to thermal energy dissipation that results from the suspension structure recoiling.
- Damping through eddy currents and magnetic hysteresis.

These sources of dissipation can be minimised to the point where the dominant sources are that which are internal.

### Internal Sources

Internal dissipation arises from energy being lost internally in the suspension system in the form of thermal energy [46]. The main source of internal dissipation is due to anelasticity of the suspensions which results in internal friction.

Consider a pendulum suspension that behaves elastically. The system will follow Hooke's law:

$$F = -kx \tag{2.4}$$

where  $F$  is the applied force,  $k$  is the spring constant and  $x$  is the displacement. When dealing with suspensions used in reality, this is not the case. The material used will in fact behave anelastically. This means that rather than the displacement being instantaneous once the force is applied, there is a delay to the reaction of the applied force. This can be visualised, as shown in figure 2.1, through the use of two spring systems in parallel, connected to a mass with one spring attached to a dashpot.

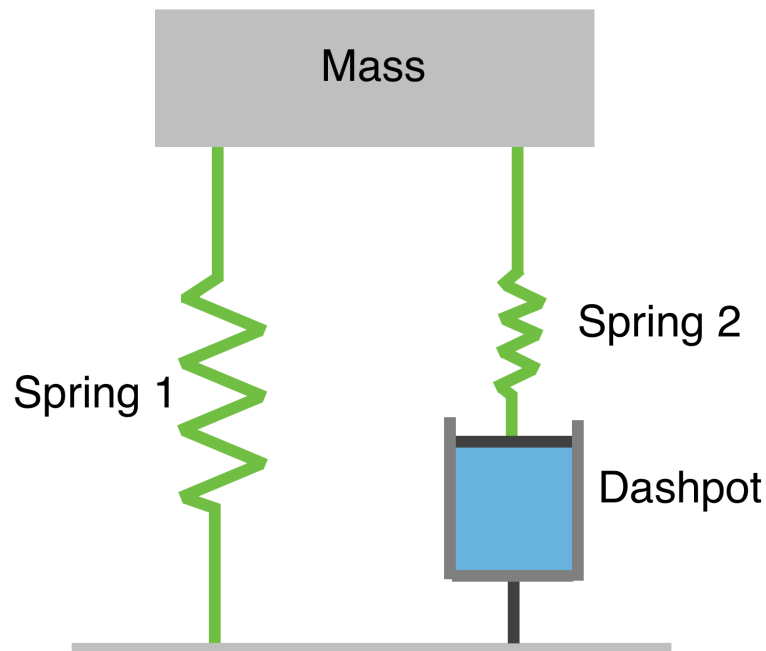


**Figure 2.1:** Diagram showing two springs in parallel, one connected to a dashpot to show the anelastic properties of a material.

The mass will compress the two springs, however the spring connected to the dashpot will decompress over time indicating an associated phase lag.

The anelasticity property of the spring will result in a complex spring constant to take into consideration the magnitudes and phase of the force displacement to give a modified version of equation 2.4:

$$F_{spring} = -k(1 + i\phi(\omega))x \quad (2.5)$$

where  $\phi(\omega)$  is the mechanical loss of the material which is the phase lag associated with the material.

For a damped harmonic oscillator with internal friction, the equation of motion is:

$$m\ddot{x} = -k(1 + i\phi(\omega))x + F_{thermal} \quad (2.6)$$

where  $m$  is the mass,  $k$  is the spring constant,  $\ddot{x}$  and  $x$  is the acceleration and displacement.

ment of the oscillator respectively and  $F_{thermal}$  is the thermal driving force.  $\ddot{x}$  and  $x$  can then be expressed in terms of velocity,  $\dot{x}$ , and frequency,  $\omega$ , such that  $\ddot{x} = i\omega\dot{x}$  and  $x = \frac{\dot{x}}{i\omega}$ . Therefore, the force on the oscillator is:

$$F_{thermal} = i\omega m\dot{x} + \frac{k}{i\omega}(1 + i\phi(\omega))\dot{x} \quad (2.7)$$

Using equation 2.2, the impedance,  $Z$ , can be expressed as:

$$Z = \frac{k - \omega^2 m + ik\phi(\omega)}{i\omega} \quad (2.8)$$

The admittance,  $Y$ , is the inverse of the impedance. By multiplying top and bottom of the equation by the conjugate of the denominator, one gets:

$$Y = \frac{k\phi(\omega)\omega + i\omega k - i\omega^3 m}{(k - \omega^2 m)^2 + k^2\phi^2(\omega)} \quad (2.9)$$

Taking only real parts of equation 2.9:

$$\Re(Y) = \frac{k\phi(\omega)\omega}{(k - \omega^2 m)^2 + k^2\phi^2(\omega)} \quad (2.10)$$

and combining with equation 2.3:

$$S_x(\omega) = \frac{4k_B T}{\omega^2} \frac{k\phi(\omega)\omega}{(k - \omega^2 m)^2 + k^2\phi^2(\omega)} \quad (2.11)$$

and substituting  $k = \omega_0^2 m$ :

$$S_x(\omega) = \frac{4k_B T}{\omega} \frac{\omega_0^2 m\phi(\omega)}{(\omega_0^2 m - \omega^2 m)^2 + (\omega_0^2 m)^2\phi^2(\omega)} \quad (2.12)$$

one can obtain the thermal noise power spectral density:

$$S_x(\omega) = \frac{4k_B T}{\omega} \frac{\omega_0^2\phi(\omega)}{m[(\omega_0^2 - \omega^2)^2 + \omega_0^4\phi^2(\omega)]} \quad (2.13)$$

This shows that to keep thermal noise to a minimum in the test masses and suspensions, the mechanical loss,  $\phi$ , of the material used must be very low. It was found [47] that fused silica shows a low mechanical loss value and has been used to create the monolithic suspensions in the interferometers.

### 2.2.2 Thermoelastic loss

A source of thermoelastic noise arises through internal dissipation. This can occur in both the suspensions and the test masses. For the suspensions, consider a silica fibre, that is bending. A temperature gradient generating a heat flow will occur in the bending region where one side of the fibre is compressed, resulting in a temperature increase, where as the opposite side that is stretched will result in a temperature decrease. This temperature gradient is determined via the thermal expansion coefficient,  $\alpha$ :

$$\alpha = \frac{1}{l} \frac{dl}{dT} \quad (2.14)$$

where  $l$  is the length of the fibre,  $dl$  is the change in length and  $dT$  is the change in temperature. The thermoelastic loss can be shown as [46]:

$$\phi_{Thermoelastic} = \frac{YT}{\rho C} \alpha^2 \left( \frac{\omega\tau}{1 + \omega^2\tau^2} \right) \quad (2.15)$$

where  $\phi_{Thermoelastic}$  is the linear thermoelastic loss,  $Y$  is the Young's modulus,  $T$  is the temperature,  $\rho$  is the density of the material,  $C$  is the specific heat capacity,  $\omega$  is the angular frequency and  $\tau$  is the characteristic time for heat to flow across the sample. The characteristic time for heat to flow for a fibre can be calculated via:

$$\tau = \frac{\rho C d^2}{13.55k} \quad (2.16)$$

where  $d$  is the diameter of the fibre.

It is shown [48] that the thermoelastic noise can be theoretically nullified by asserting a specific stress on the silica fibre. This is due to the Young's modulus of silica increases with temperature. For a silica fibre, the thermoelastic loss is:

$$\phi_{Thermoelastic} = \frac{Y_o T}{\rho C} \left( \alpha - \alpha_o \frac{\beta}{Y_o} \right)^2 \left( \frac{\omega \tau}{1 + \omega^2 \tau^2} \right) \quad (2.17)$$

where  $Y_o$  is the Young's modulus at room temperature,  $\alpha_o$  is the static stress on each fibre,  $\beta = \frac{1}{Y_o} \frac{dY}{dT}$  and all other variables hold prior definitions. This shows that the thermoelastic loss can be cancelled out should  $\alpha_o = \frac{\alpha \gamma}{\beta}$ . It was found that the silica fibre has a thermal expansion value of  $(4.1 \pm 0.2) \times 10^{-7} \text{ K}^{-1}$  and  $\beta = (1.67 \pm 0.05)^{-4} \text{ K}^{-1}$  [48]. The majority of the thermoelastic energy in the silica fibre is contained in the 800  $\mu\text{m}$  region, which requires a stress of 195 MPa to be applied for this noise to be nullified.

### 2.2.3 Dissipation Dilution

As mentioned previously, gravitational wave detectors make use of multiple stage pendulum systems to help combat seismic noise as well as thermal noise in the low frequency ranges. This means that most of the test mass' energy is in the form of gravitational potential energy [49]. If we take a test mass suspended on a single fibre, the mass will exert a force,  $F$ , of:

$$F = mg \quad (2.18)$$

on the fibre, where  $m$  is the mass of the test mass and  $g$  is the acceleration due to gravity. Should the mass now be displaced horizontally, there will be a restoring force acting to bring the mass back to an equilibrium. During this displacement, the main region that experiences the bending is at the top of the fibre. One can equate equation

2.18 with the restoring force  $F_{restore} = kL$ , where  $L$  is the length of the fibre to get:

$$k_{grav} = \frac{mg}{L} \quad (2.19)$$

where  $k_{grav}$  is the spring constant equivalent in a gravitational field.

The energy stored in the fibre is:

$$E_{stored\ in\ fibre} = \frac{1}{2}k_{fibre}x^2 \quad (2.20)$$

where  $k_{fibre}$  is the spring constant of the fibre and  $x$  is the horizontal displacement of the mass. As the mass moves, it would lose a fraction of its potential energy due to the internal friction in the top of the fibre,  $\epsilon$ , per cycle:

$$E_{lost\ per\ cycle} = \epsilon \frac{1}{2}k_{fibre}x^2 \quad (2.21)$$

The quality factor is defined as:

$$Q = 2\pi \frac{E_{stored\ in\ fibre}}{E_{lost\ per\ cycle}} = \frac{1}{\phi_{material}} \quad (2.22)$$

can then be rearranged to find the loss to give:

$$\phi_{fibre\ loss} = \frac{\epsilon}{2\pi} \quad (2.23)$$

The total potential energy stored in the pendulum is:

$$E_{stored\ in\ pendulum} = \frac{1}{2}(k_{fibre} + k_{grav})x^2 \quad (2.24)$$

where  $k_{grav}$  is the effective spring constant associated with the gravitational field.

Therefore:

$$\phi_{pendulum\ loss} = \frac{\epsilon k_{fibre}}{2\pi(k_{fibre} + k_{grav})} \quad (2.25)$$

One can therefore get a ratio of losses between that of the fibre and the pendulum:

$$\frac{\phi_{\text{pendulum loss}}}{\phi_{\text{fibre loss}}} = \frac{k_{\text{fibre}}}{k_{\text{fibre}} + k_{\text{grav}}} \quad (2.26)$$

Since  $k_{\text{grav}} \gg k_{\text{fibre}}$ ,

$$\phi_{\text{pendulum loss}} \approx \phi_{\text{fibre loss}} \frac{k_{\text{fibre}}}{k_{\text{grav}}} \quad (2.27)$$

This is indeed the case resulting in the dilution factor,  $D$ , which is the factor that the mechanical loss in the pendulum system is reduced over the mechanical loss in the fibre:

$$\frac{1}{D} = \frac{k_{\text{fibre}}}{k_{\text{grav}}} \quad (2.28)$$

An aLIGO fibre for example is found to have a dilution factor of 77 and 75 for the fundamental and second violin modes [50].

As the test masses and fibres are made of fused silica, a low loss material (high Q factor), this results in the concentration of energy in the system at the resonant modes. This means there is less off resonance thermal noise and can be seen in figure 2.2 [51], where the narrow peaks show a horizontal mode (red) and a vertical mode (blue) for the monolithic suspension for aLIGO.

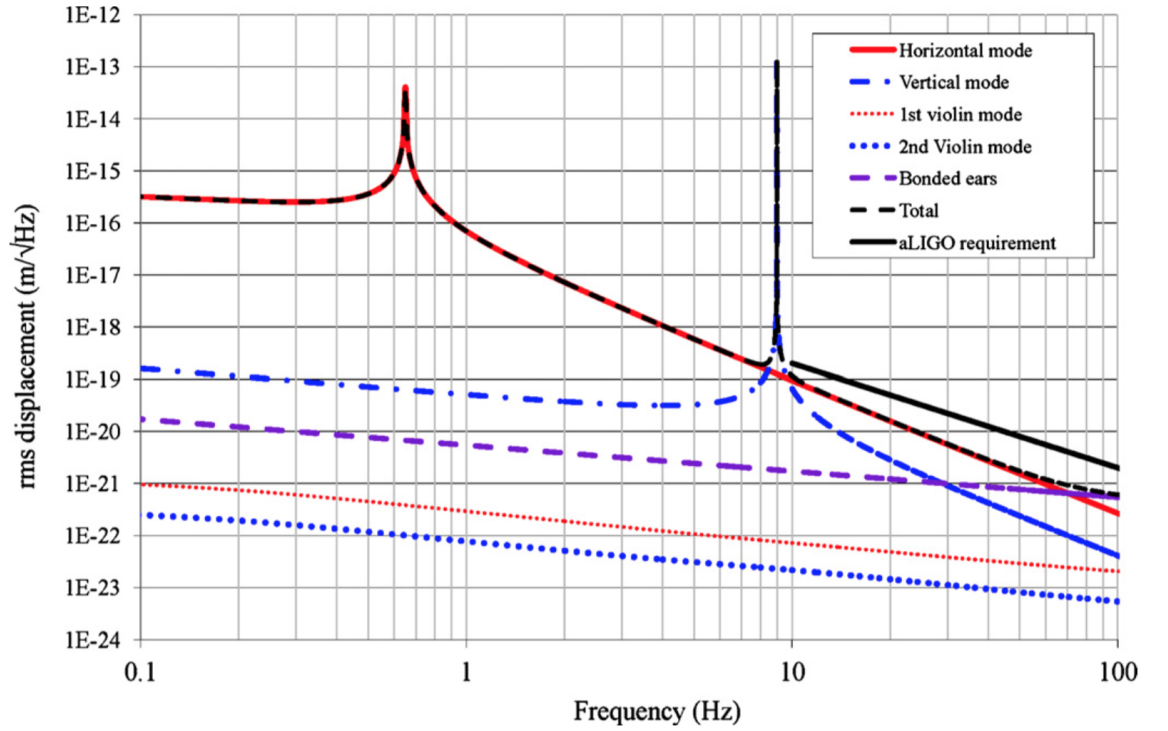


**Figure 2.2:** The displacement thermal noise spectra for a single aLIGO suspension [51].

The pendulum mode thermal noise arises from the mechanical loss associated with the material used to suspend the test mass.  $k_{fibre}$  for a pendulum system with  $n$  wires can be expressed as [52]:

$$k_{fibre} = \frac{n\sqrt{TYI}}{2L^2} \quad (2.29)$$

where  $T$  is the tension of the fibre,  $Y$  is the Young's modulus,  $I$  is the moment of inertia of the fibre and  $L$  is the length of the fibre. Using equation 2.29 and 2.19, one can express equation 2.27 as:

$$\phi_{pendulum\ loss} \approx \phi_{fibre\ loss} \frac{n\sqrt{TYI}}{2mgL} \quad (2.30)$$

## 2.2.4 Violin mode

The fibres holding the test masses also experience a transverse vibrational mode, known as violin modes. These modes are a harmonic series with the number of modes observed

depending on how wide the frequency band of the gravitational wave detector is. The loss associated with the first violin mode is [52]:

$$\phi_{violin\ loss} = 2\phi_{pendulum\ loss} \quad (2.31)$$

since the dilution factor of the first violin mode is half that of the pendulum mode. As the suspensions are made from fused silica, the thermal noise associated with the violin modes will be concentrated within a narrow frequency range next to the resonance frequencies. However, the low loss and high Q for fused silica results in a long ring down time, timescale of days, of these modes. This therefore requires a damping system to combat this to limit the downtime of the interferometer [53] [54].

## 2.3 Conclusion

Thermal noise is one of the most important noise sources that limits the sensitivity of the interferometer detectors. Extensive research and development had gone into looking at how to decrease the thermal noise for the upgrades applied to the second generation of gravitational wave detectors. The thermal noise upgrades, as well as other upgrades associated with other noise sources, has resulted in the most sensitive gravitational wave detectors with the hope of directly observing gravitational waves for the first time.

There is however a desire to make the next generation of detectors even more sensitive through both room temperature and cryogenic upgrades. This requires research and development to produce fibres suitable to suspend the test masses, which will have different masses depending on the experiment.

# Chapter 3

## Development of the fibre pulling machine

### 3.1 Aim of this project

Currently, the fibre pulling machine that produces silica fibres for the aLIGO monolithic suspensions, pulls fibres with a central diameter of 400  $\mu\text{m}$  to hold 40 kg test masses [50]. The pulling machine, monolithic suspensions and a silica fibre can be seen in figures 3.1, 3.2 and 3.3 respectively. There is however a desire to use thinner fibres for other related test experiments that require the use of smaller masses and therefore thinner fibres, such as for the AEI 10 m prototype [55] and the Sagnac Speed Meter (SSM) [40]. The aLIGO pulling machine can pull fibres down to 20  $\mu\text{m}$ , however the neck that appears is a lot longer than desired. This is due to the pulling stage not being able to accelerate fast enough to create a short enough neck which has led to the design of a new pulling machine. The aim of this project was to develop and characterise the small diameter silica fibre pulling machine. This new machine has been designed to pull fibres to have a diameter smaller than 20  $\mu\text{m}$ .

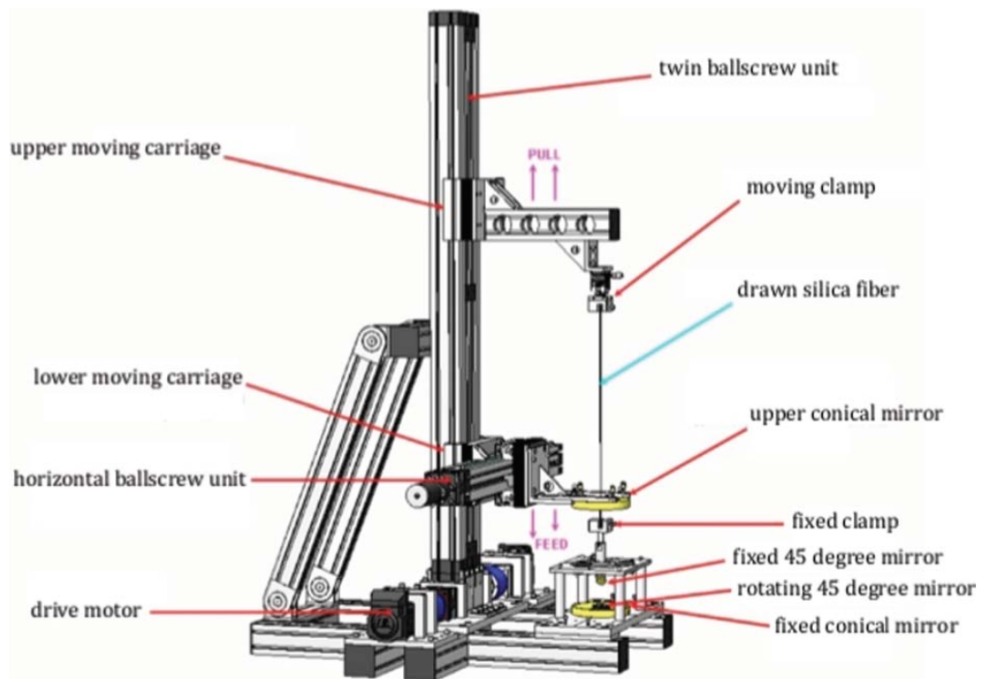


**Figure 3.1:** CAD drawing of the aLIGO pulling machine with all major components annotated [56].

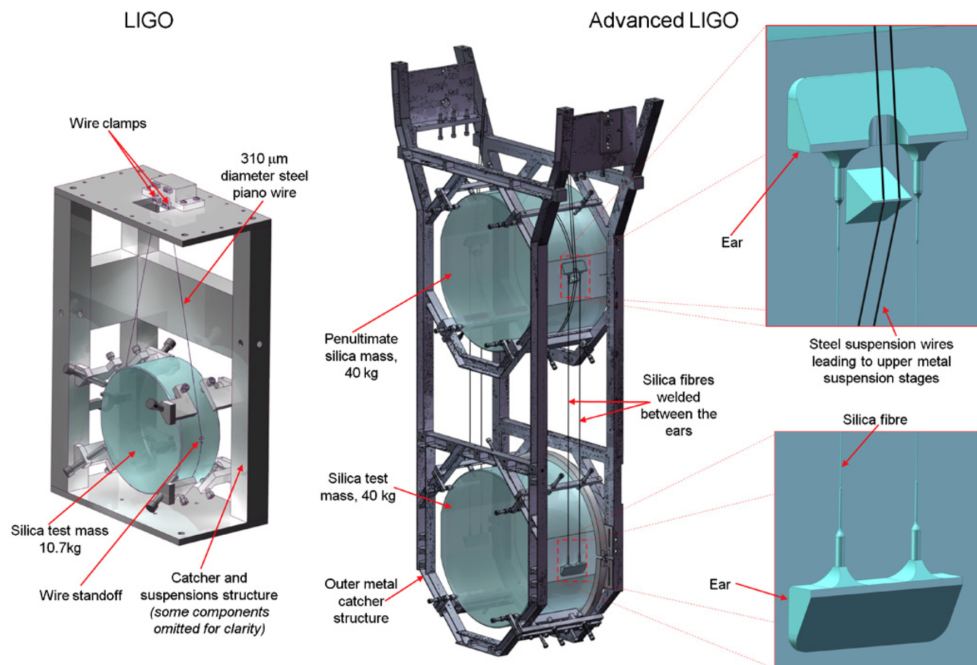


**Figure 3.2:** The suspension system that was used for LIGO and the upgraded suspensions for aLIGO [50].

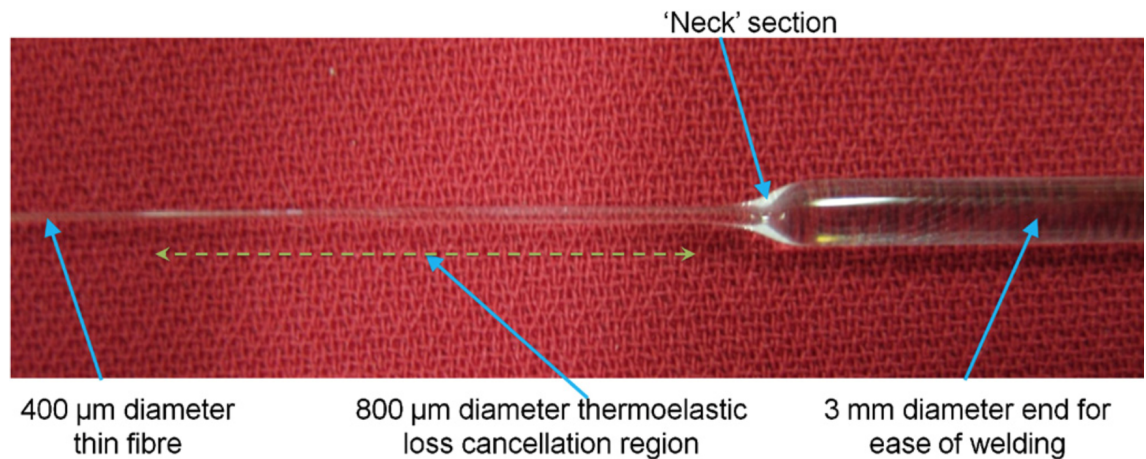


**Figure 3.3:** A fibre that was pulled from the aLIGO fibre pulling machine [50].

### 3.1.1 General concept of pulling machine to produce small diameter silica fibres

The pulling machine is based on similar principles as that of the aLIGO fibre pulling machine [56], though in this case, utilising a high acceleration pulling stage to create short thin silica fibres. A diagram of the pulling stage can be seen in figure 3.4. The stage has a maximum velocity of  $500 \text{ mm s}^{-1}$  and a maximum acceleration of  $26,000 \text{ mms}^{-2}$  and a total travel length of 40 cm. The maximum length of fibre that can be produced is approximately 35 cm, with the aim of creating fibres with a diameter less than  $20 \text{ }\mu\text{m}$ . This is due to the fibre extraction process requiring extra room to allow the fibre to be removed from the clamps without damaging any of the optics on the bench, though there is the possibility of reducing the room needed to extract the fibre to maximise the possible fibre length.

A  $\text{CO}_2$  laser is focused onto the silica stock using a selection of lenses to a beam waist approximately around  $100 \text{ }\mu\text{m}$ . To bring the beam onto the silica stock, a custom gold plated mirrors are used. A cone mirror, referred to as the ‘axicon’, and two conical mirrors, one of which is fixed onto the same base plate as the axicon and the second on a motorised stage. The cone mirror spreads the laser beam out to the first conical

mirror to then create a cylindric beam across to the second conical mirror. The beam then reflects onto the stock heating up around the circumference.

The silica stock needs to be in a molten state to commence the pulling process. It is obvious to the user when using the pulling machine when this occurs as the silica stock will go from a dim orange colour around the heated region, shown in figure 3.5, to a bright white glow, shown in figure 3.6. The power needed will change depending on diameter of the stock used. The user would then wait anywhere between 5 and 10 seconds before commencing the pull. As the pull commences, the second conical mirror (known as the feed mirror) moves at a set velocity along the stock. This is so the fibre does not run out of material to pull from. The velocity of the feed mirror depends on the diameter and length of the desired fibre. For a very short fibre or a fibre produced in a few hundred milliseconds, the feed mirror wont move at all. For a thin fibre that takes approximately a second to produce, the feed mirror would move at a velocity  $\leq 0.5 \text{ mm s}^{-1}$ . For thicker fibres, the feed mirror would move at a velocity  $\geq 0.5 \text{ mm s}^{-1}$ . This waiting period is just a general rule of thumb and is ultimately up to the user. It is possible for the laser to vaporise the silica stock should the laser power be too high. Therefore the user would initially control the laser power manually through the laser controller to understand approximately the power needed for the silica to reach its molten state before controlling the laser through the computer programme.

In depth detailed explanations, diagrams and configurations for the pulling machine are discussed in the following section.

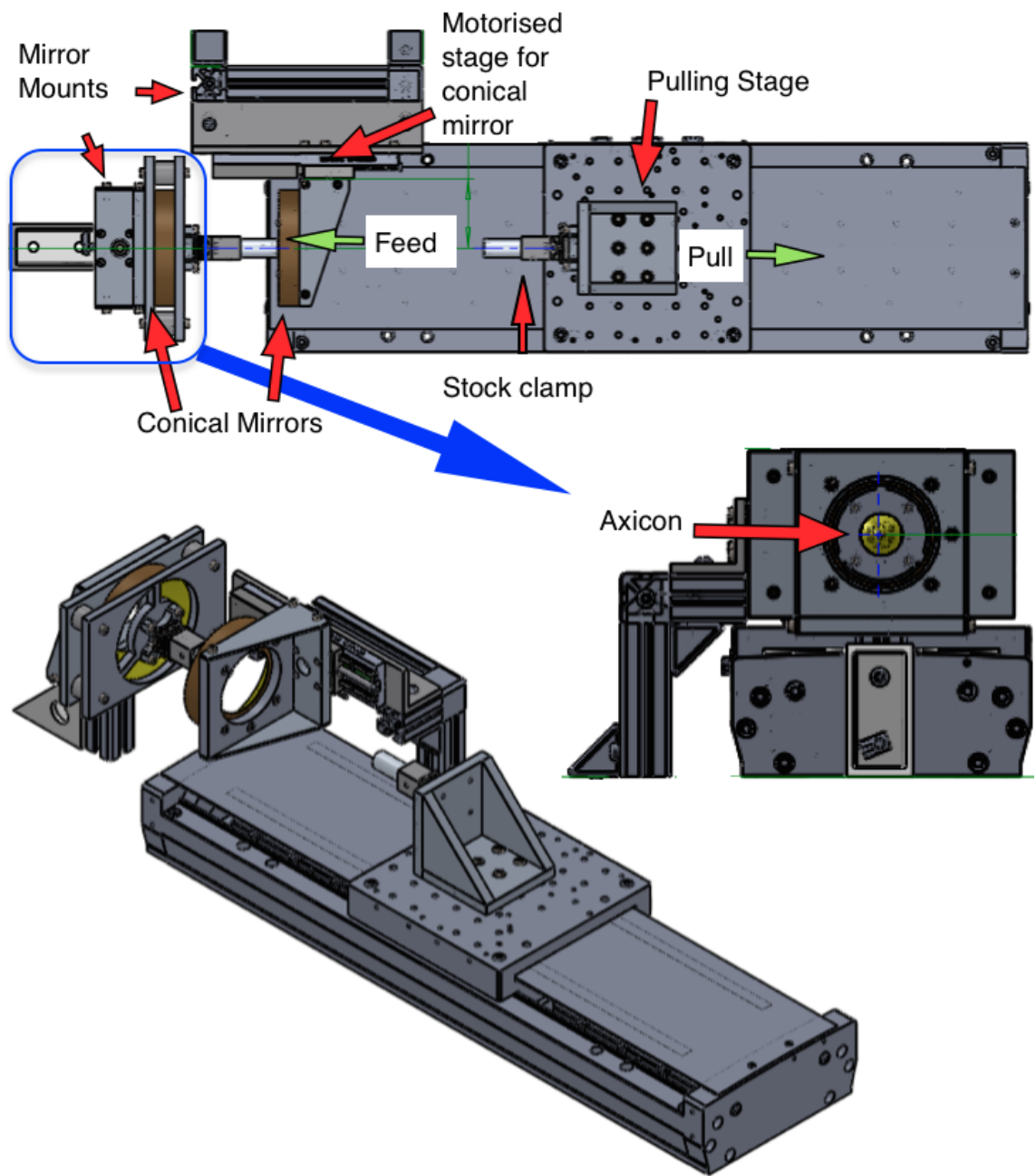


**Figure 3.4:** Solidworks CAD rendering of the initial design of the small diameter silica fibre pulling machine courtesy of Liam Cunningham and Russell Jones.

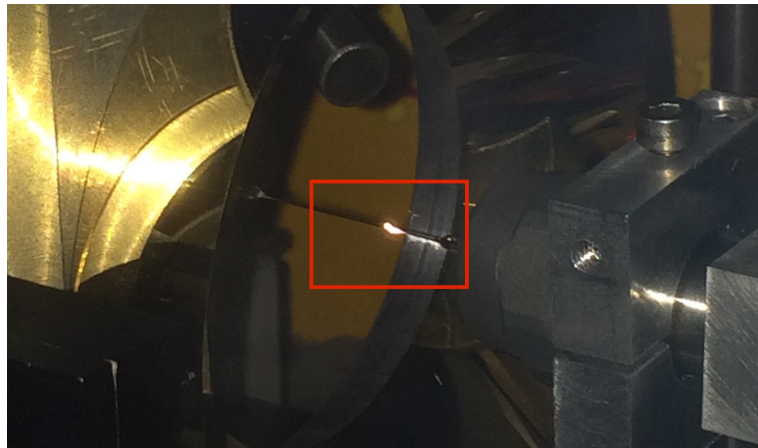


**Figure 3.5:** Silica stock, highlighted in red, just before going to its molten state.



**Figure 3.6:** Silica stock once heated up to its molten state.

## 3.2 Design

### 3.2.1 Initial Design

The pulling stage, Newport IMS-400LM, has a maximum acceleration of  $26000 \text{ mms}^{-2}$ , a maximum velocity of  $500 \text{ mms}^{-1}$  and a total range of 400 mm. The user can vary the diameter of the stock, by either using thin stock producing a fibre with a one stage pull, or pull down from a thicker stock to give a thinner diameter stock and producing the fibre from the centre of this in a two stage pull, which will be discussed later.

The longest length of fibre that can be produced with this stage is approximately

350 mm. This is due to the fact that although the stage had a total travel of 400 mm, there needs to be enough room to initially get the stock into the holders and enough room to then remove the pulled fibre, which takes up approximately 50 mm.

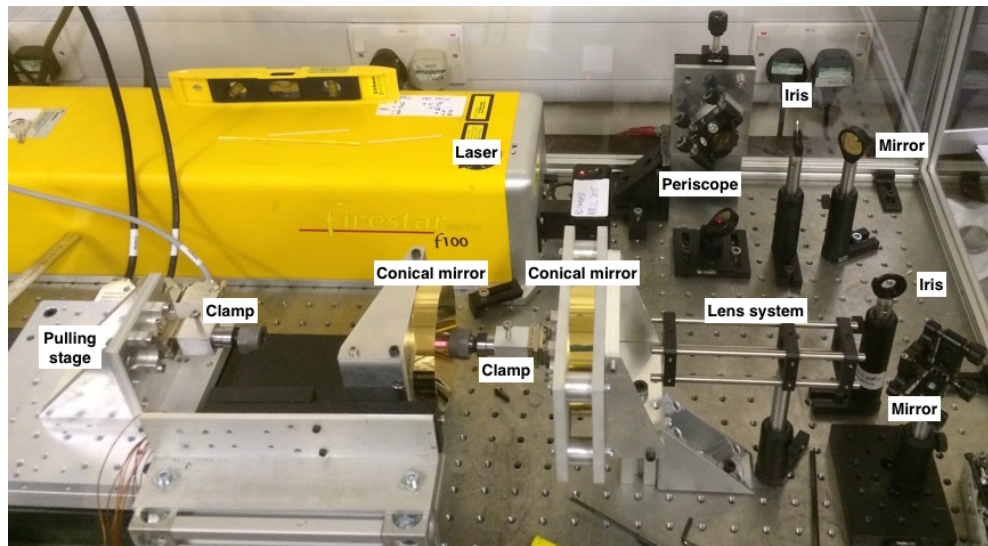


**Figure 3.7:** The initial setup of the small diameter silica fibre pulling machine.

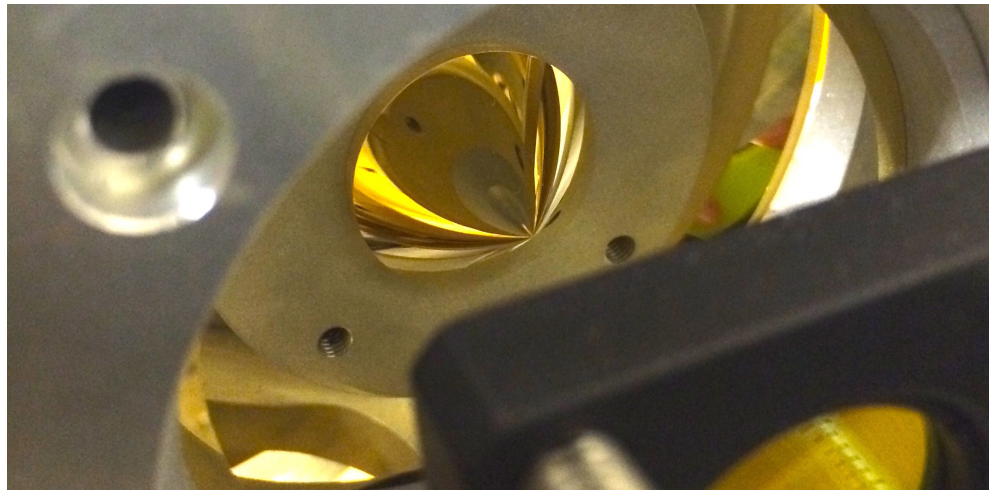


**Figure 3.8:** The axicon that is attached to the backplate of the first conical mirror mount.

To focus the beam around the stock, the aLIGO fibre puller uses a rotating  $45^\circ$  mirror, shown in figure 3.1, to spread the beam out to the first conical mirror to create a cylindrical beam. The second conical mirror then directs the beam to the stock. This

pulling machine however utilises a fixed cone mirror, also known as an axicon shown in figure 3.8, to reflect the beam onto conical mirrors to produce a cylindrical beam to focus onto the stock. An illustration of the optical path for the beam is shown in figure 3.10. The axicon is situated on the back plate of the first conical mirror mount such that it lies in the centre of the conical mirror. The beam hits the tip of the cone, spreading the beam in all directions out towards the first conical mirror. The first conical mirror reflects the incoming split beam as a cylinder towards the second conical mirror, which reflects the beam back towards the stock. The advantage to the axicon design system is that there are less moving parts in the set up, which can help with the long term alignment stability of the machine.

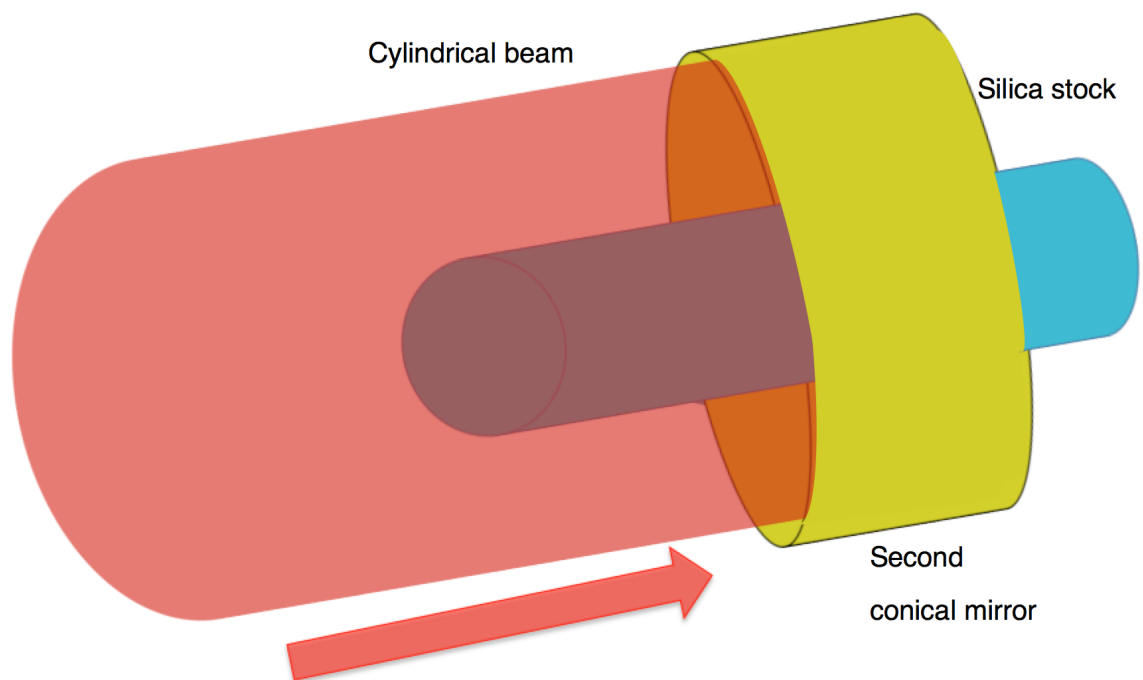


**Figure 3.9:** Illustration of the cylindrical beam reflecting off the second conical mirror onto the stock.

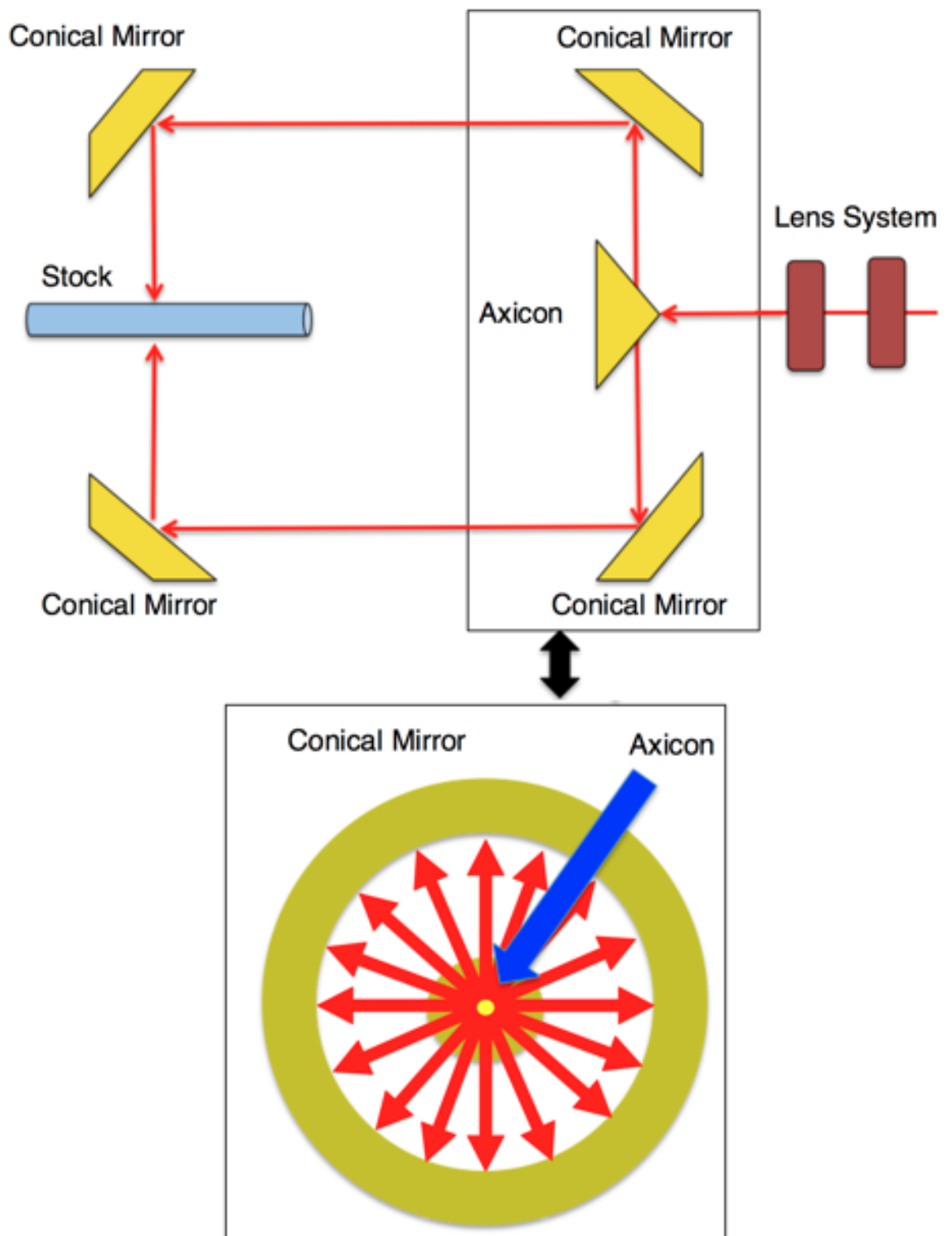


**Figure 3.10:** Illustration of the optical path for the laser beam once it reflects off the axicon.

### 3.2.2 Current configuration and alignment process

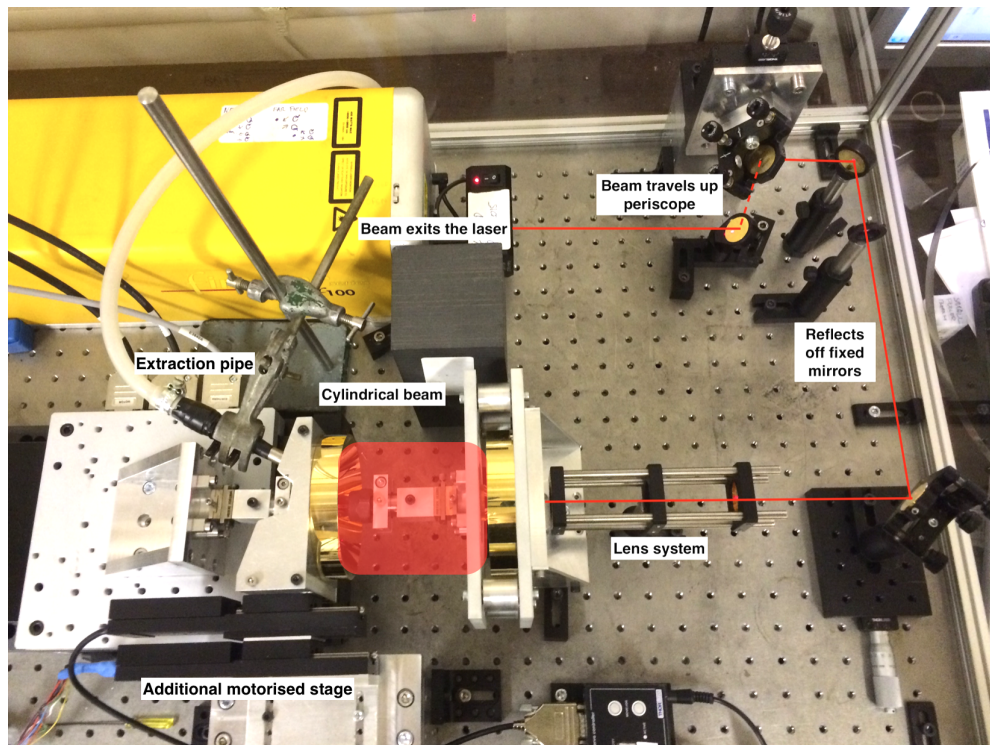


**Figure 3.11:** Layout of the pulling machine in its current form.

Figure 3.11 shows the current configuration of the pulling machine, with the annotations showing the major changes that have been carried out compared to the pulling machine in figure 3.4 and the laser beam path. The addition of another motorised feed stage stacked on top of the original stage was due to the stage not providing enough travel to give enough working space to extract the fibre safely with enough clearance between the fibre and the conical mirror. An extraction pipe was also added to prevent any silica vapour touching the mirror during the pulling process, as a build up of vapour can damage the mirror.

The beam exits the laser and travels up a periscope to the height of the cone mirror. The beam then reflects off two mirrors, one of which is sitting on a horizontal translation stage, and through a lens system. The lenses used are a plano-concave lens with focal length of -100 mm and a positive meniscus lens with focal length 110 mm,

which will be discussed later. Once out of the lens system, the beam hits the axicon and the two conical mirrors finishing at the silica stock.

The motorised stages are programmed via a custom LabVIEW program written by a previous student [57]. This allows the user to control the pulling stage by either reading in a text file containing various velocities, acceleration and time values, or by stating absolute positions to travel to at specified velocities. The feed stage is also controlled via the program by inputting the desired velocity. Laser control through the LabVIEW program has since been added by the author to allow the user to input a desired laser power prior and during the pulling process. The program then returns the laser power to zero at the moment the stage has stopped moving to avoid heating the stock after the fibre has been produced.

It is absolutely essential that all the components on the bench are aligned properly to pull repeatably consistent fibres. The following is the process taken to ensure that the machine is aligned prior to the pulling of fibres:

1. The beam must be parallel to the bench. This assumes that the stage is parallel to the bench. This is critical in ensuring that the centre of the beam hits the centre of the cone mirror. Should the beam come in at an angle to the cone mirror, then the beam will not be distributed equally around the stock, shown in figure 3.12, resulting in uneven heating of the stock and less control over the desired neck shape. By placing an iris with a small aperture, or a target plate as shown in figure 3.13, throughout the optical path, one will be able to see if there is any change in the beam height. The first adjustment for this process will be from the knobs on the kinematic mirror mount at the top of the periscope. This mirror has a pitch, yaw and height adjustments available to allow the beam to travel parallel to the bench until it reaches the second kinematic mirror mount. The second mount will ensure that the beam continues to travel parallel to the bench before it reaches the lenses and the cone mirror. Once the user is satisfied

that the beam is parallel to the bench along the entire optical path, these knobs should not be adjusted again unless there is a significant change in the set up.

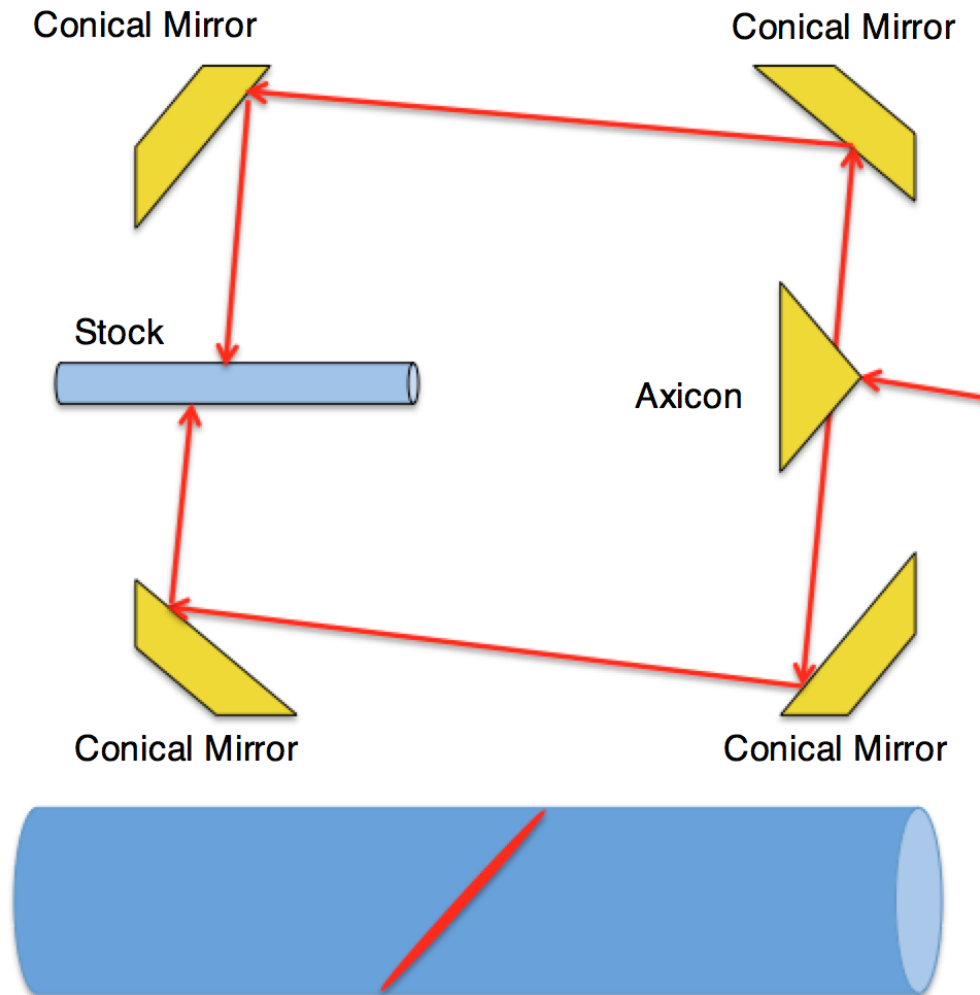


**Figure 3.12:** The beam path and distribution of the beam if the beam hits the tip of the axicon at a slight angle.

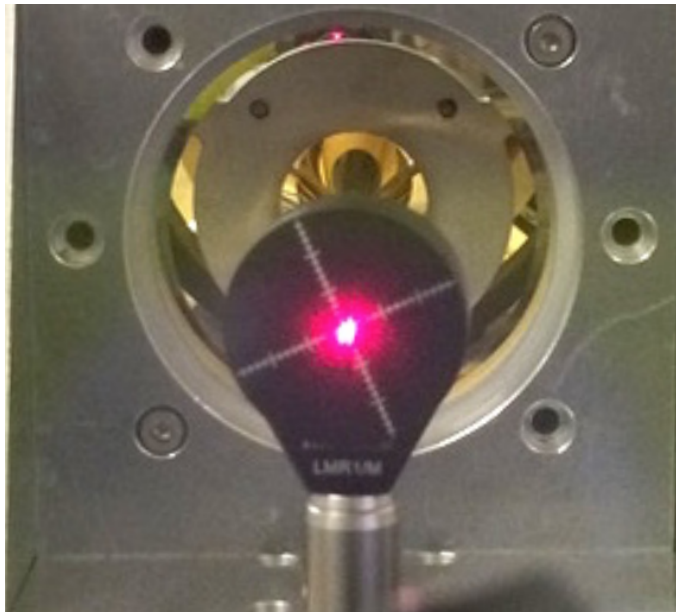


**Figure 3.13:** A target plate placed after the second kinematic mirror mount used to get the beam parallel to the bench.

2. The cone mirror and the two conical mirrors must be perpendicular to the bench. In this set up, the cone mirror and one conical mirror form one unit while the second conical mirror is part of a separate unit. If the cone mirror is not perpendicular to the bench, the user will run into issues with aligning the beam at the stock. As mentioned in the previous step, the user will get an annulus with an even beam distribution if the beam is hitting the centre of the cone, shown in figure 3.14. In the near field, the user might get an annulus similar to figure 3.14, however, there can be a slight variation in the beam distribution that is not easily seen. Should the cone mirror be perpendicular and the user let the alignment beam travel an extra 3 metres for example, if the mirror is not perfectly perpendicular resulting in the beam not hitting the tip of the mirror, then the beam will take a non circular shape, an example of which is shown in figure 3.15. The plate holding the cone mirror must then be adjusted until an evenly distributed annulus appears in the far field to ensure the mirror is in the correct position. However, if the cone mirror is perfectly perpendicular, the annulus should still

be the same shape, as in figure 3.14.

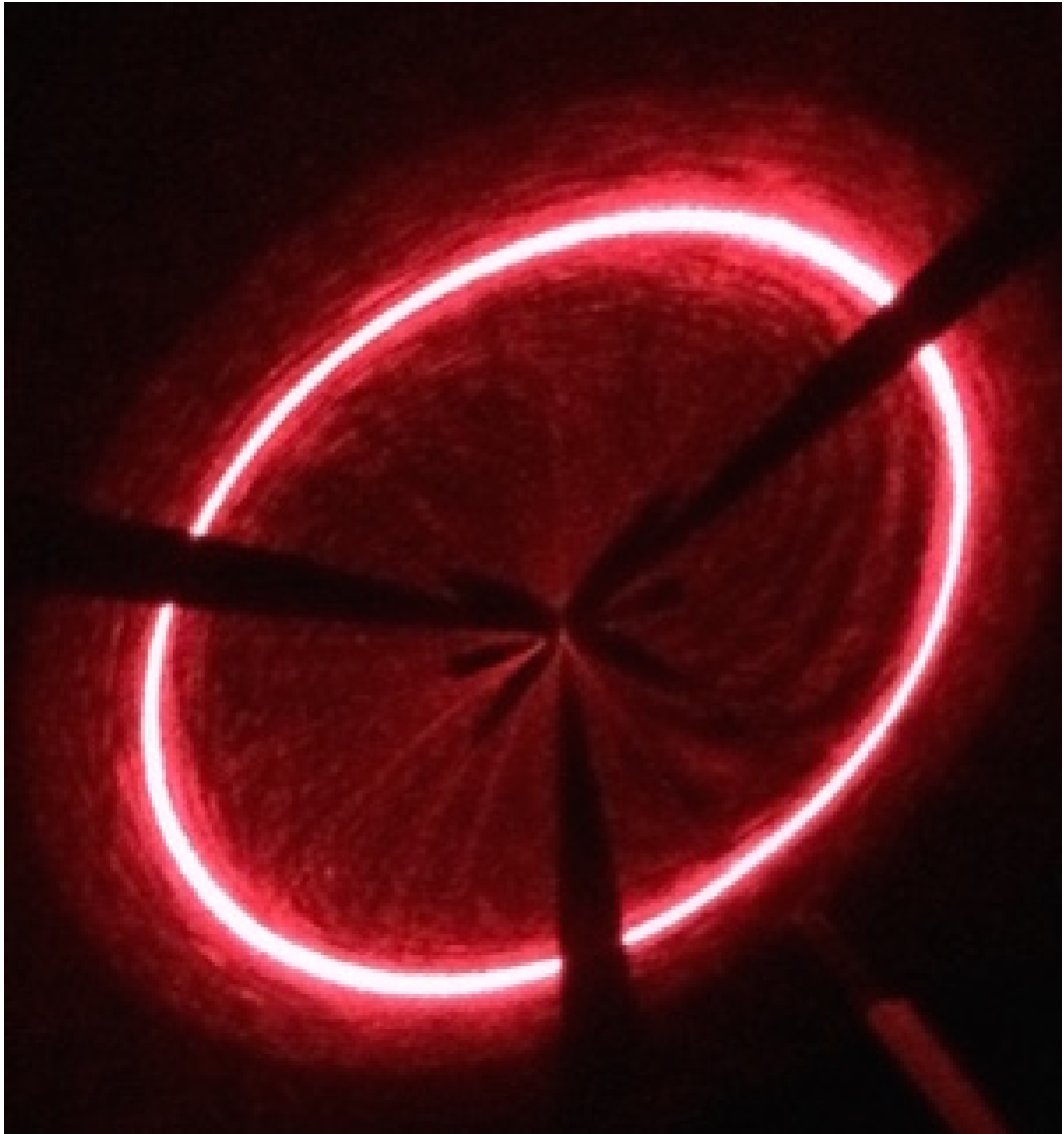


**Figure 3.14:** An annulus seen on a viewing screen immediately after the first conical mirror showing the desired beam distribution indicating the beam hitting the centre of the cone mirror.



**Figure 3.15:** The beam distribution in the far field indicating that the cone mirror is not perfectly perpendicular to the bench.



**Figure 3.16:** The beam distribution in the far field after a slight adjustment indicating the cone mirror is almost in the correct position.

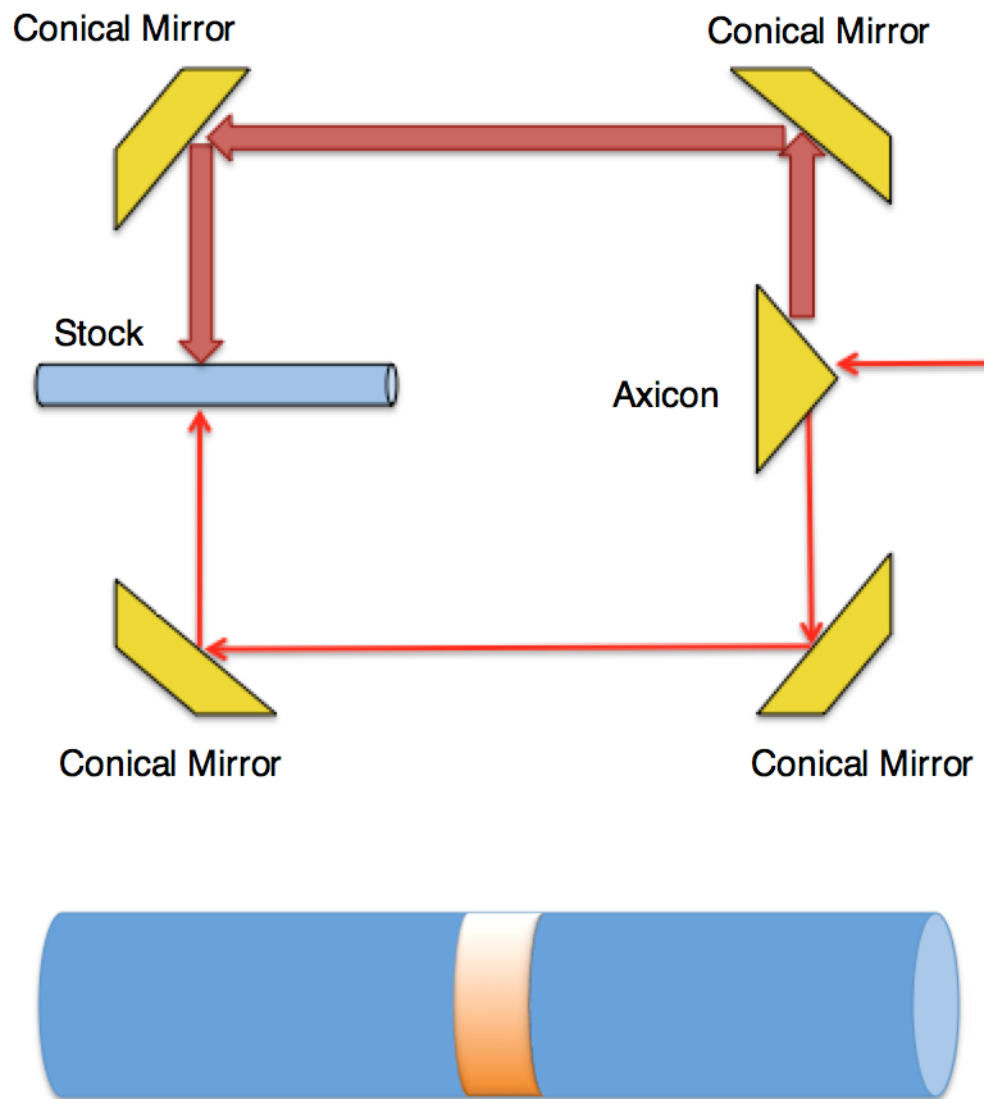


**Figure 3.17:** Illustration of the beam path if the beam hits the cone just above the tip.

3. The beam must hit the centre of the cone mirror. If the beam is perpendicular to the tip of the cone, but hits the cone slightly above the tip, the majority of the beam will be concentrated on the top of the stock. This is illustrated in figure 3.17, where the top of the heated stock, in white, is hotter than the bottom, in orange. By placing a viewing screen after the first conical mirror, the user will see how the beam has been distributed from the cone. If the beam is hitting the cone on the centre, then an annulus will appear with an even distribution of the

laser light. By adjusting the translation stage positions that the two kinematic mirror mounts are attached to, the beam can be moved until this is the case, shown in figure 3.14.

4. The two conical mirrors must be coaxial. If this is not the case, then the beam will not hit the stock around the same plane, but will be spread like an ellipse around the stock similar to the distribution in figure 3.12. By adjusting the position of the feed conical mirror, the user will eventually get the beam around the circumference of the stock, as shown in figure 3.18.



**Figure 3.18:** The ideal distribution of the beam around the silica stock.

5. The beam must hit the centre of the lenses. Alignment tools with crosshairs are put in place for where the lenses are positioned in the cage system. If the beam were to hit the lenses anywhere other than the centre, the beam would hit the stock in an ellipse shape along the stock rather than around a small circumference, again resulting in less control over the fibre shape.
6. The two stock clamps must be coaxial. This can be checked by placing a piece of silica stock into the clamp attached to the conical mirror mount. The user can then move the other clamp, that is attached to the pulling stage, right to the end of the stock. By adjusting the small X-Y translation stages the clamps are mounted onto, the user can make the two clamps coaxial. An alternative method is to place a piece of silica stock into the two clamps, secure tightly and heat up with the laser. As the stock becomes molten, if there is any stress on the stock from the clamps not being coaxial, the stock will move, as shown in figure

3.19, illustrating the magnitude of the misalignment. The user can then move the translation stages to fix the misalignment and repeat the process until the clamps are coaxial.



**Figure 3.19:** A piece of silica stock that has been mis-shapen due to the clamps not being coaxial.

### 3.2.3 Future changes

The puller has been designed in an attempt to make the alignment process as easy as possible. There are however plans for future changes in the hope that these will simplify the process. An example of a possible change is a redesign of the first conical mirror face plate to hold the lens system to form one unit. This would allow an accurate reference point to work from, making lens placement more precise as well as providing extra support for the cage system to help prevent accidental movements and drooping of the rods in the lens system.

As well as making the first mirror mount and lens system one unit, it is planned to make the two conical mirrors mounts one unit. Currently, the two conical mirror mounts and the lens system for the lenses are all independent from each other on the optical bench. Unifying all these components into one unit with a base plate will allow consistent reference points to work from, aiding the user by simplifying the alignment process. Forming one unit for the conical mirrors will ease the task of ensuring that the two mirrors are coaxial so that the beam hits the stock around its circumference.

One possible major change would be to eliminate the mirror adjustments and place the laser directly behind the lenses to decrease the optical path length and create a compact unit. This would require the laser to be placed at the height of the cone mirror and does not leave much room for error with the lack of adjustments available.

## 3.3 Beam Profiling

When using small diameter silica stock for the purpose of pulling small fibres, the laser beam must be concentrated to a small area to heat up the stock successfully. It is therefore necessary to profile the beam of the laser that is being used to discover possible full width half maxima, FWHM, of the beam using various lenses to focus the beam to a small area.

### 3.3.1 Beam Simulation

The first step was to create a simulation of the optical path to find out the beam size at the point where the beam hits the stock and then to determine what lenses could be used to focus the beam down. This was done using a mode matching program called “JAMMT” (Just Another Mode Matching Tool) [58]. Creating a simulation of the optical path and comparing the data obtained through the simulation with that obtained experimentally will mean that should the two sets of data be in a good agreement, the mode matching program can then be used to simulate different lens combinations. By inputting the necessary data about the laser such as its wavelength, beam waist at source and the beam divergence, the user can see the size of the beam over a given beam path.

According to the data sheet [59], the laser has a beam waist of  $3.5 \pm 0.1$  mm and a beam divergence of  $4 \pm 0.2$  mrad at the source. This means that after the beam travels one metre, the beam waist will be approximately 7.5 mm. Lenses can then be added to give a desired beam spot. Due to the size of the optical bench, there was a limit to the number of lenses that could be placed in the beam path as well as where the telescope could sit on the bench. The only practical areas that the telescope could sit was between the final beam line mirror and the cone mirror at the start of the pulling machine or between the two beam line mirrors.

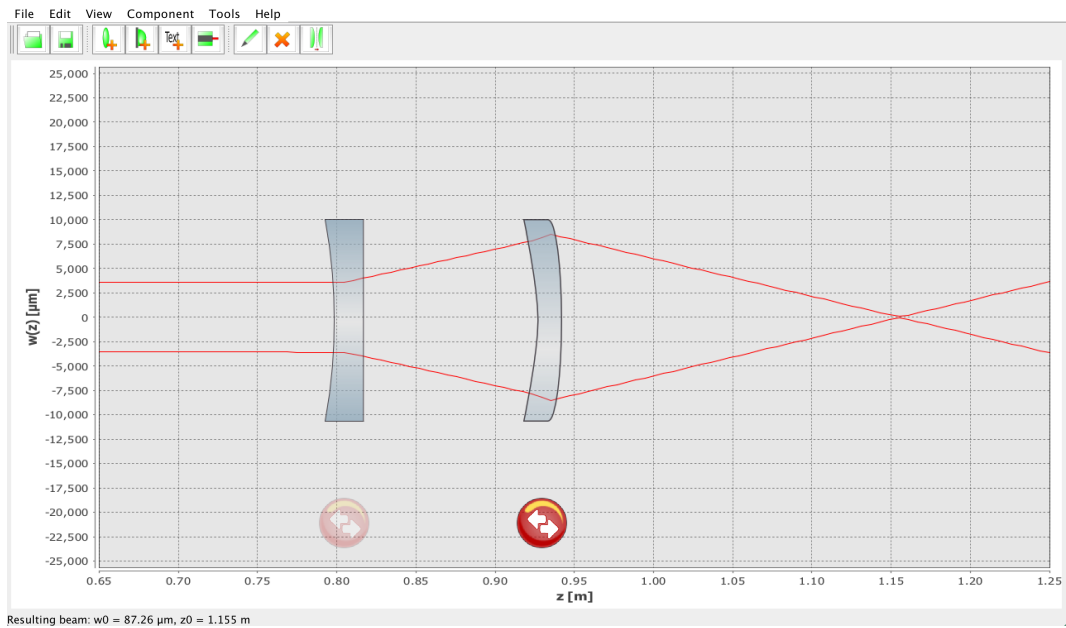


**Figure 3.20:** Simulated lens layout using JAMMT using  $f=-100$  mm plano-concave and  $f=110$  mm positive meniscus lenses with the lenses at 0.805 m and 0.930 m into the beam path and the focus at 1.155 m.

The simulation showed that a plano-concave lens with focal length  $-100$  mm and a positive meniscus lens with focal length  $110$  mm placed  $0.805$  m and  $0.93$  m respectively, should give a beam waist of  $87.26 \mu\text{m}$  at  $1.155$  m, as shown in figure 3.20 and 3.21. More lenses could be added to the system to gradually bring the beam waist down as the beam travels around the bench if a smaller beam waist was desired and might be looked at in the future should bench space increase.

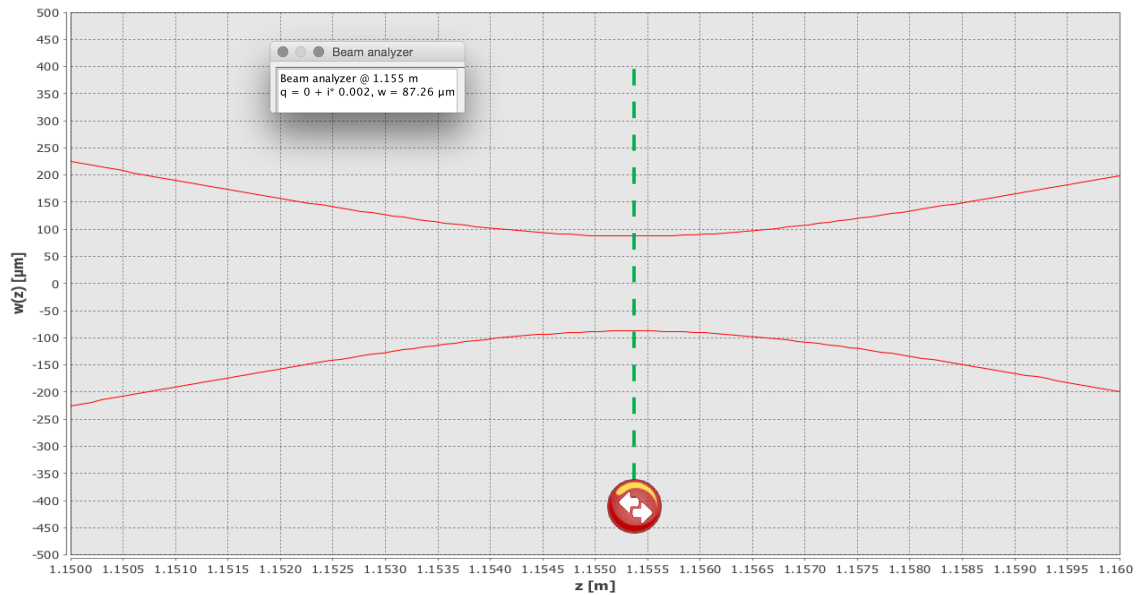


**Figure 3.21:** Data obtained from the JAMMT simulation showing the simulated beam waist of 87.26  $\mu\text{m}$  at an optical path length of 1.155 m.

### 3.3.2 Experiment to measure the beam waist

The experimental set up, shown in figure 3.22, consisted of two power monitors to measure the input and output powers respectively. It is necessary to monitor the input power as the laser power can fluctuate, even after extended periods of use. The main beam passes through a piece of zinc selenide, ZnSe, which is sitting at the Brewster's angle causing a small percentage of the beam being reflected towards the input power meter, while the rest of the beam passes through until it reaches the output power meter. The Brewster's angle is calculated via:

$$\theta = \tan^{-1} \left( \frac{n_2}{n_1} \right) \quad (3.1)$$

where  $\theta$  is the Brewster's angle ( $67.4^\circ$ ),  $n_2$  is the refractive index of the zinc selenide (2.4028) at 10.6  $\mu\text{m}$  [60] and  $n_1$  is the refractive index of air (1) [61].

A chopper is placed in the path to the input detector spinning at 70 Hz modulating the power by breaking up the beam with the input detector connected to a lock in

---

amplifier. In front of the output detector is a 50  $\mu\text{m}$  pinhole, both of which are placed on a horizontal translation stage which allows the pinhole to gradually pass across the beam to allow the power intensity to be measured. Both detectors are connected to a data acquisition device to then send the data to the computer. A custom LabVIEW program was used to read the data and plot it with respect to time for both the input and output voltages.

It is necessary to make sure that the laser beam is parallel to the optical bench to ensure that the beam is coming in perpendicular to the pinhole and the detectors. This was achieved via the use of irises placed along the optical path, all of which are sitting at the same height. Alignment tools, such as mounted beam targets, were also used to ensure that the beam was hitting the middle of the mirrors and the lenses to allow the full range of mirror adjustments available.

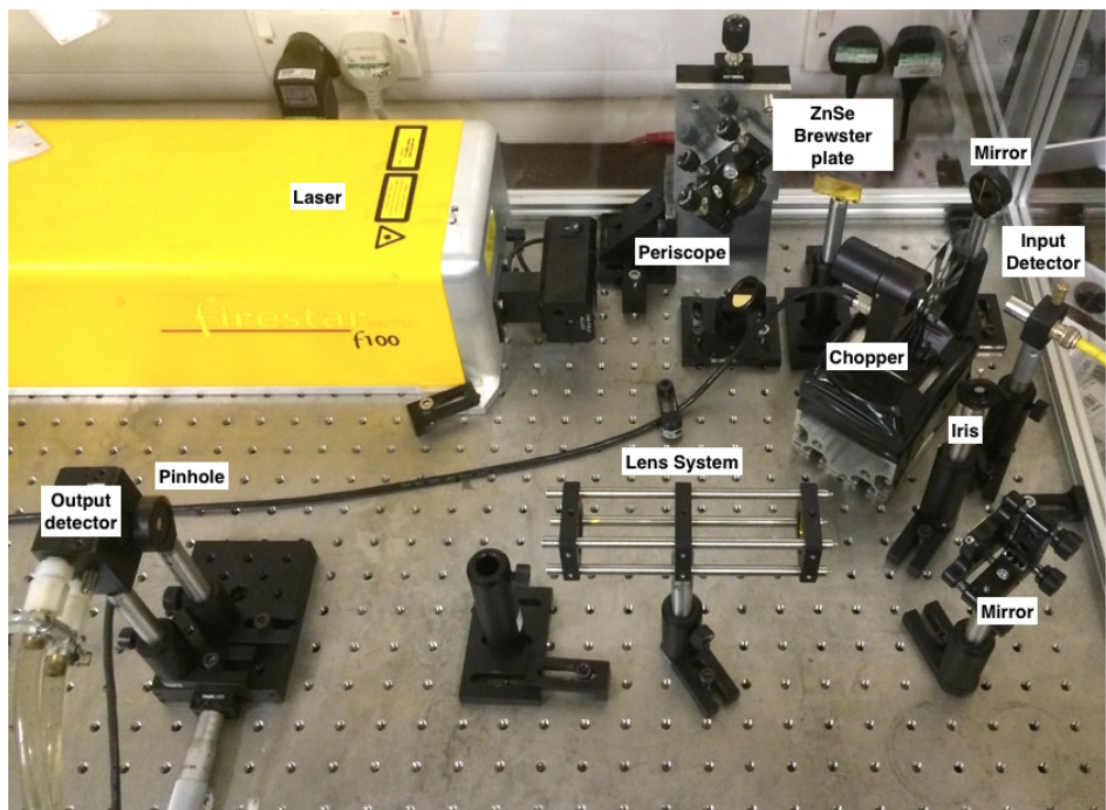
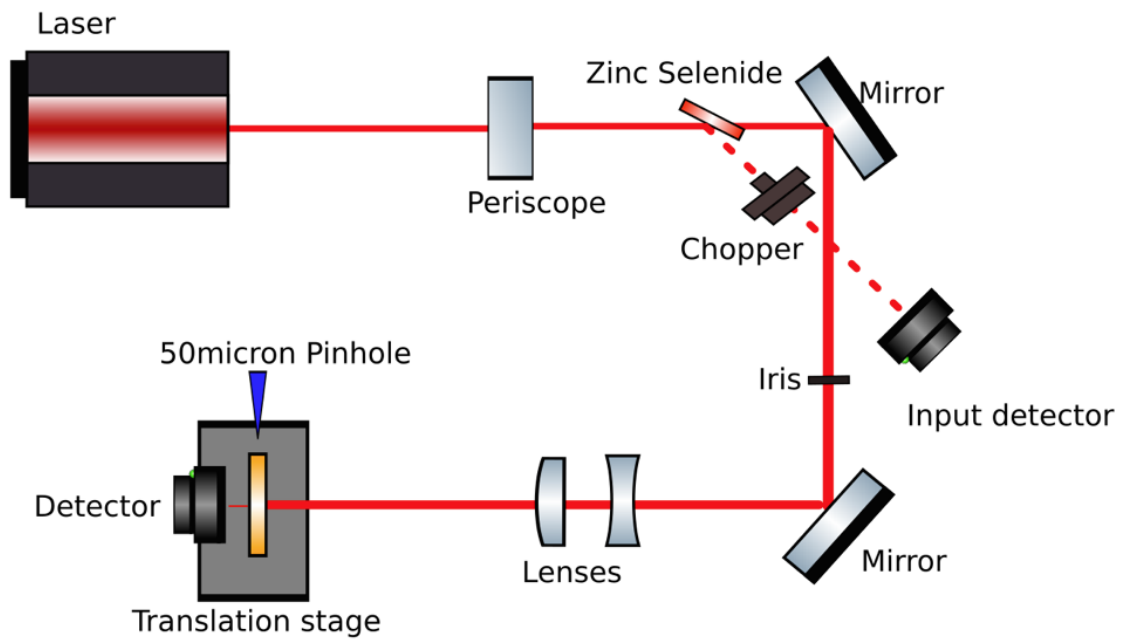


**Figure 3.22:** Illustration of layout of equipment and experimental setup used to take the profile of the laser beam.

### 3.3.3 Experimental results

The laser must be run for a period of time prior to measurements taken due to the power fluctuation experienced from the moment the laser is turned on (cold start). This fluctuation, according to the data sheet, can be in the region of  $\pm 10\%$  for a cold start and  $\pm 6\%$  after two minutes. Here, the laser was run for at least 10 minutes at 10 W prior to measurement to minimise the fluctuations experienced. This power was also chosen to prevent damaging the input detector due to the fact that only the output detector was water cooled. A total of 5 sets of data were taken with each set consisting of three data runs which could then be averaged in the following order: one at the focal point, -2.5 mm, -5 mm, +2.5 mm and +5 mm where the distances are with respect to the predicted focal point. The data runs consisted of 3 complete sets of readings at each position, moving the translation stage by  $0.010\text{ mm} \pm 0.005\text{ mm}$  every 6 seconds with a micrometer. A wait time of 6 seconds was chosen due to the fact that the program used to obtain the data obtained readings every 2 seconds. This meant that every 6 second interval could be averaged over three readings.

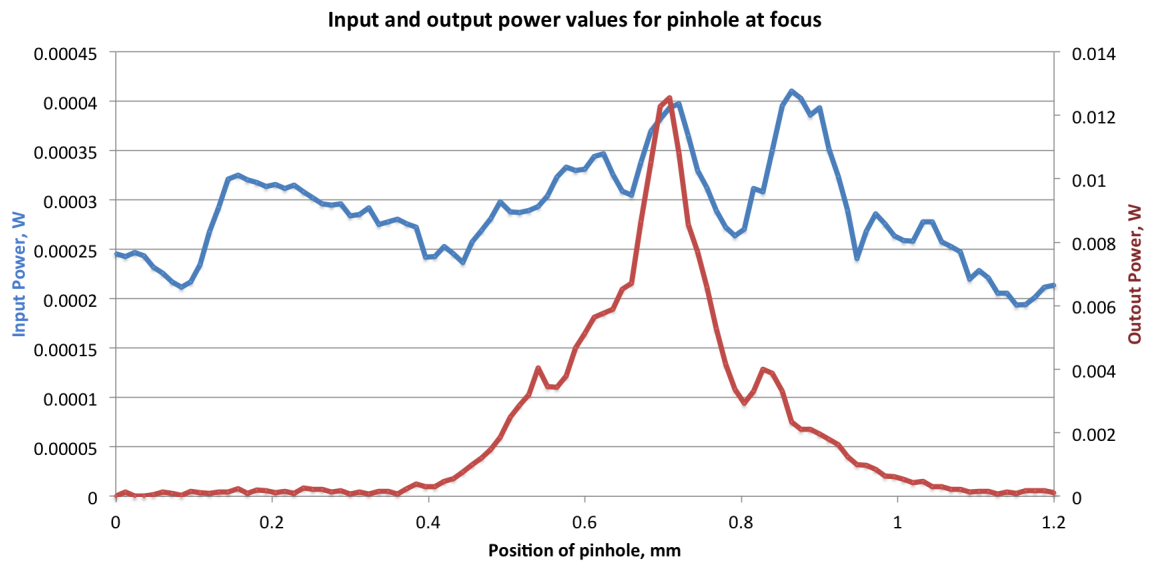


**Figure 3.23:** Three run average showing the input and output power obtained as the beam passes through the 50  $\mu\text{m}$  pinhole at the focus.

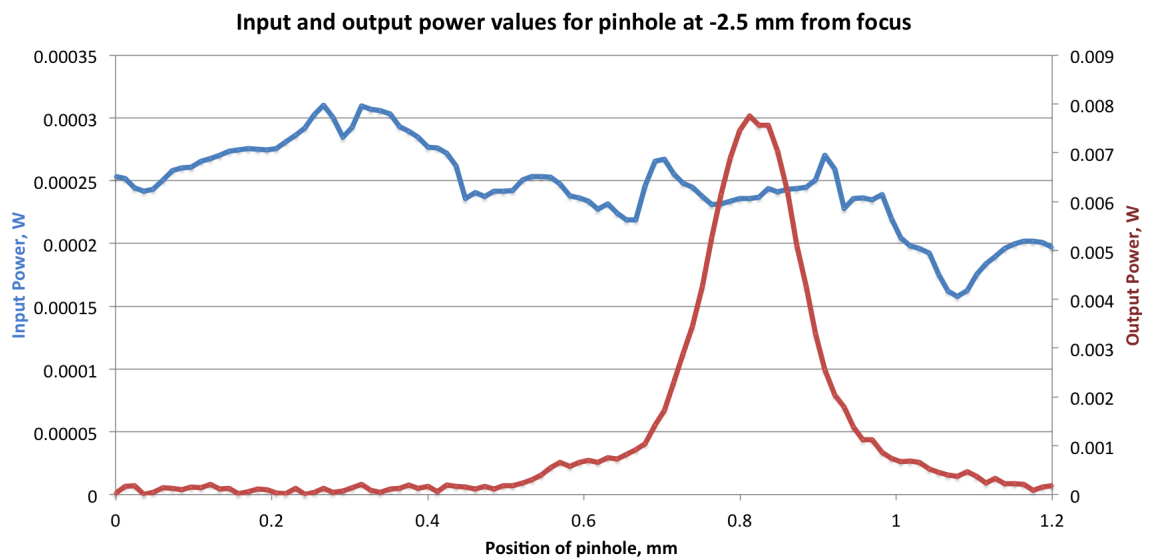


**Figure 3.24:** Three run average showing the input and output power obtained as the beam passes through the 50  $\mu\text{m}$  pinhole, -2.5 mm from focus.

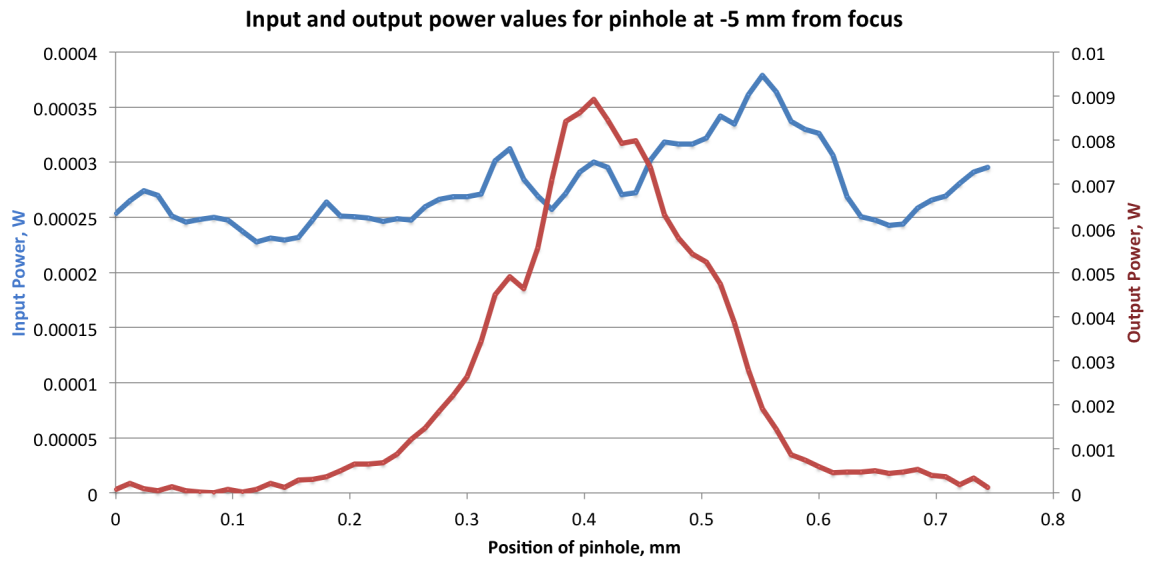


**Figure 3.25:** Three run average showing the input and output power obtained as the beam passes through the 50  $\mu\text{m}$  pinhole, -5 mm from focus

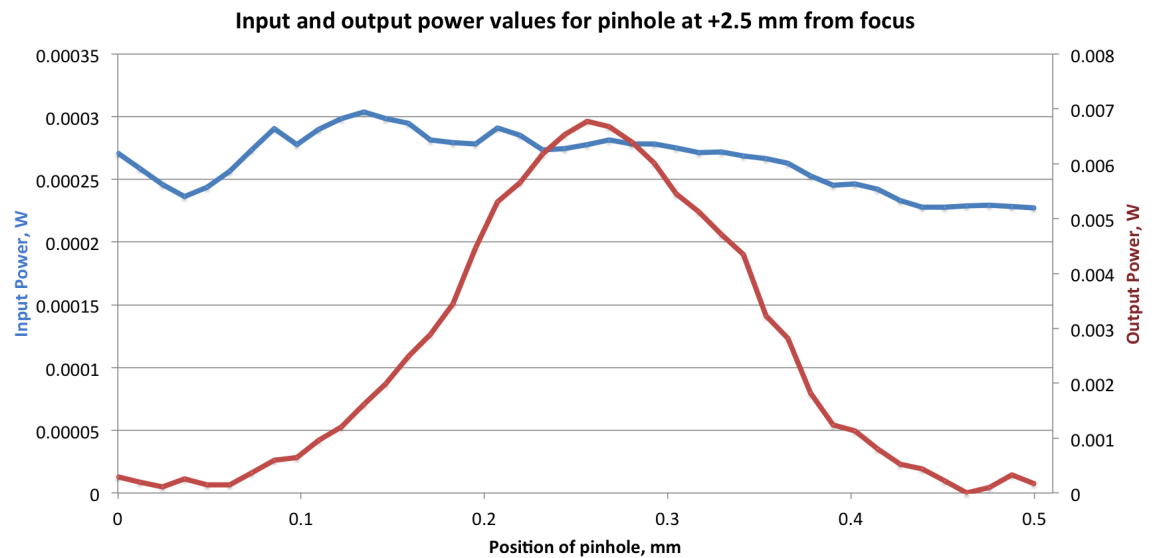


**Figure 3.26:** Three run average showing the input and output power obtained as the beam passes through the 50  $\mu\text{m}$  pinhole, +2.5 mm from focus.

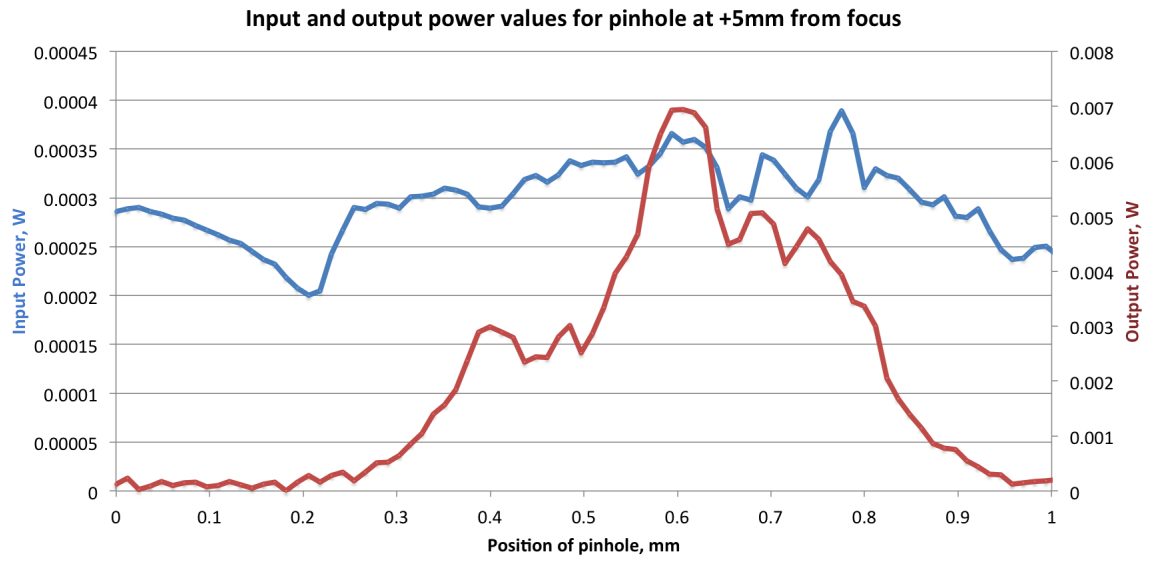


**Figure 3.27:** Three run average showing the input and output power obtained as the beam passes through the 50  $\mu\text{m}$  pinhole, +5 mm from focus.

**Table 3.1:** The FWHM obtained for the 5 different data sets that were obtained.

FWHM (mm) $\pm 0.007$ mm	Pinhole Position (mm)	JAMMT values (mm)	Difference (mm)
0.105	$0.00 \pm 0.25$	0.087	0.018
0.143	$-2.50 \pm 0.35$	0.130	0.013
0.190	$-5.00 \pm 0.43$	0.211	0.021
0.176	$+2.50 \pm 0.50$	0.130	0.046
0.350	$+5.00 \pm 0.56$	0.211	0.139

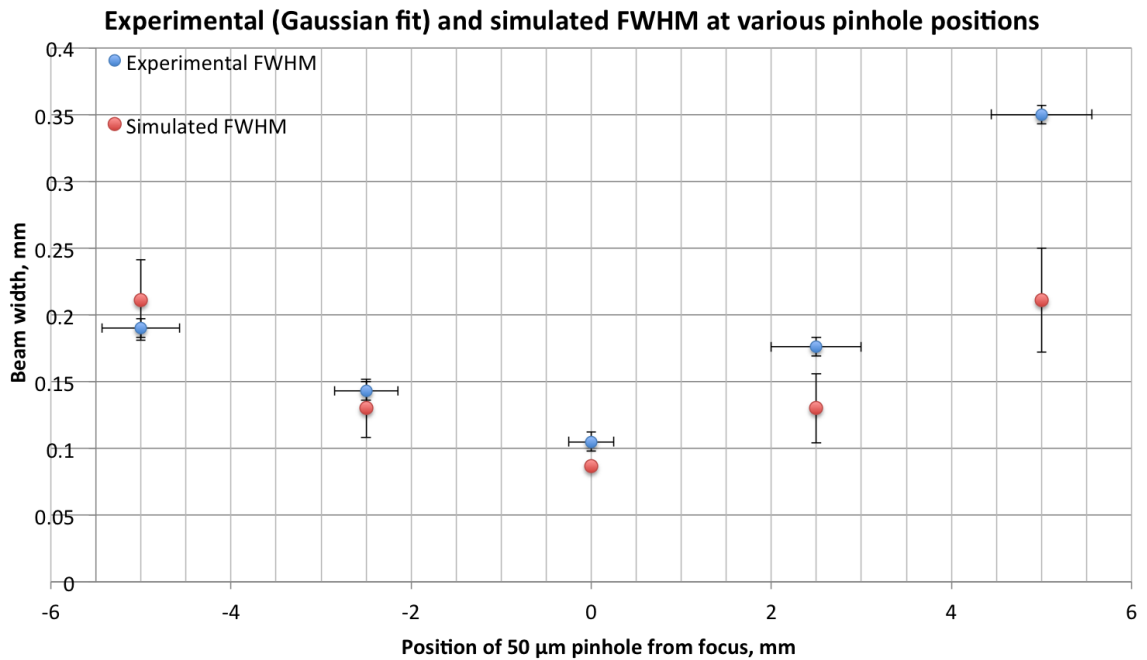


**Figure 3.28:** Simulated and experimental beam waists at the five measured positions.

Table 3.1 shows the FWHM values gained during the 5 data runs, shown in figures 3.23 - 3.25, as well as their corresponding simulated values with both sets of data compared in figure 3.28. The FWHM values were found by fitting a Gaussian to the output data from figures 3.23 - 3.25. One should note that the complete time for the data sets were not exactly the same for every set. This was due to the starting position on the translation stage not being exactly the same for every set as one had to ensure that the beam was not already entering the pinhole at the start of the run.

The data showed that the beam had a beam waist of  $105 \mu\text{m} \pm 7 \mu\text{m}$  when the pinhole was placed in the focal point. The beam intensity for a 10 W beam, using  $I = \frac{P}{A}$ , where  $I$  is the intensity,  $P$  is the laser power and  $A$  is the area of the beam would give a value of  $11.5 \times 10^8 \text{ Wm}^{-2}$  at the focus. This waist value is  $18 \mu\text{m}$  larger than that in the simulation. When placing the pinhole further away from the focal point, the beam waist values were  $176 \mu\text{m}$  and  $350 \mu\text{m}$  which were  $46 \mu\text{m}$  and  $139 \mu\text{m}$  larger than the simulated values respectively. When moving the pinhole closer to the

lenses, the beam waist values were  $143\ \mu\text{m}$  which was  $13\ \mu\text{m}$  larger than the simulated data and  $190\ \mu\text{m}$  which was  $21\ \mu\text{m}$  smaller than the simulated data.

### 3.3.4 Error analysis and conclusion

The experimental horizontal error bars in figure 3.28 are for the position of the pinhole. The first pinhole position, the focus, has an error of  $\pm 0.25\ \text{mm}$  that is a result of the ruler that was used to put the pinhole in position. The error then accumulates for every position after. This error could be reduced by using an X-Y translation stage - X to move the pinhole across the beam and Y to move the pinhole away from the focus. Using a stage like this would mean that moving the pinhole in  $2.5\ \text{mm}$  intervals could be more precise, as well as ensuring the pinhole will move in a straight line as moving it by hand can result in a slight deviation that could result in the pinhole not being perpendicular to the beam. The power meters that were used have an error of  $\pm 0.5\%$  according to the data sheet. The experimental vertical error bars represent the beam width error, which is  $\pm 0.007\ \text{mm}$ , that combines the translation stage error and the power meter error.

The vertical error bars on the simulated data represent the range of beam width values that the simulated data can take due to the error associated with the experimental pinhole position.

It is possible that the focus of the beam was positioned in the region between  $0$  and  $-2.5\ \text{mm}$ , which could be a reason for the experimental beam waist being  $28\ \mu\text{m}$  larger than the simulated value. Using a translation stage that can move in small discrete intervals to move the pinhole in the Y direction in smaller intervals could result in a smaller beam waist as the user could lock down on the position of the focus by taking more data readings in this region.

The movement of the translation stage to move the pinhole across the beam was carried out by hand, with an error of  $0.005\ \text{mm}$ . A metronome was used to keep the

time intervals between data readings consistent with an error of 0.1 %. To decrease the error in moving the pinhole across the beam, a motorised translation stage could be programmed to move at consistent distance and time intervals.

There are some slight differences in the values obtained which was expected when dealing with small values that are delicate to slight variations. The largest difference was 139  $\mu\text{m}$  for run 5. The runs that involved the pinhole positioned such that the path length was increased resulted in the largest deviation between the simulated values. There are several possible reasons for the differences. Though the greatest care was taken to ensure that all the components were placed at the correct distance, the lenses may not be in the centre of their holders resulting in them not being in exactly the same position as the simulation, which will cause a larger beam waist than expected.

An example of this situation is shown in figure 3.29, where the lenses have a separation of 2 cm less than the original simulation and a comparison with the experimental data in figure 3.30. The beam waist at the focus is 105  $\mu\text{m}$  with a beam path length of 1.151 m. The distance between the simulated data and experimental data for -2.5 mm and -5 mm decreases, though +2.5 mm and +5 mm is still large. This asymmetry between the position of the pinhole before and after the focus suggests that the placement of the pin hole for +2.5 mm and +5 mm could be slightly greater than expected. As previously mentioned, a translation stage with small discrete increments would solve this issue.

It was determined that a beam width of  $105 \pm 7 \mu\text{m}$  was sufficiently small enough for the task in hand. This gives a beam intensity of  $11.5 \times 10^8 \text{ Wm}^{-2}$  at the focus. In the future, if a smaller beam width is desired, then more lenses can be placed throughout the optical path, or added to the lens system.

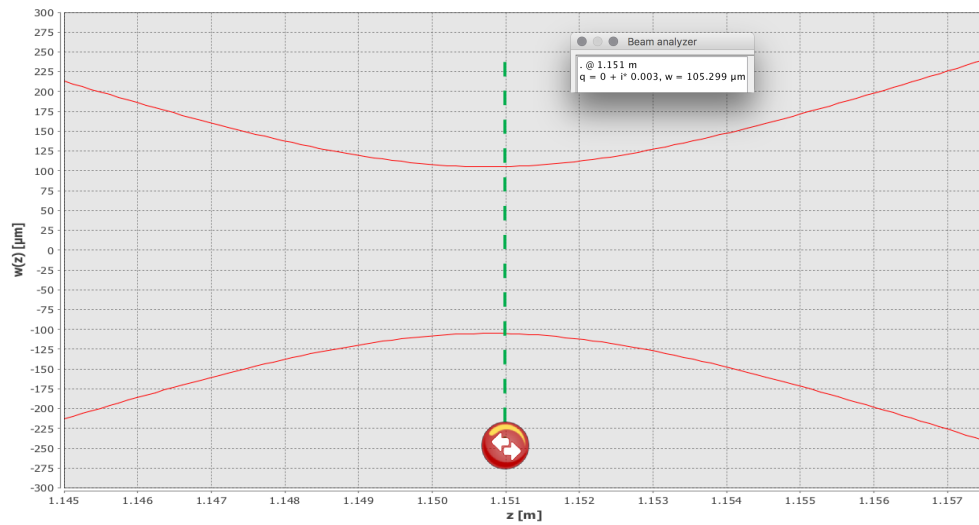


**Figure 3.29:** Alternate simulation with the distance between the lenses 2 cm less than original simulation.

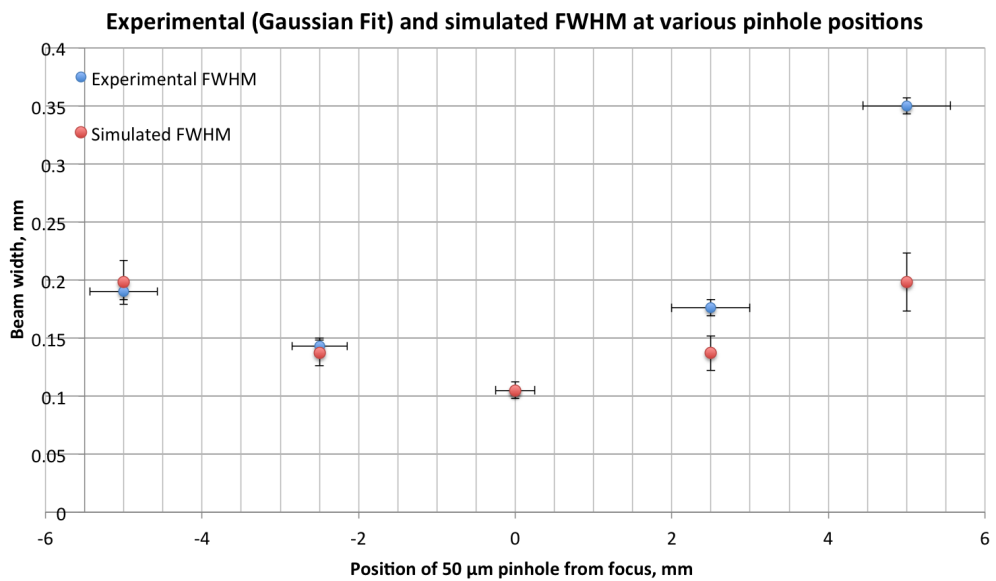


**Figure 3.30:** Alternate simulated and experimental beam waists at the five measured positions.

## 3.4 Characterising the pulling stage

### 3.4.1 Introduction

One of the aims for this project is to see if the current set up can consistently produce repeatable fibres. There are several factors that determine the characteristics of the

fibres produced, see chapter four and five, though the main factor is the precision of the stage's position and velocity that pulls the silica stock to create the fibres. This section looks into the precision of the stage positions over repeated measurements to see how large a variation will occur. The stage is controlled via a LabVIEW program [57] where the user inputs a text file containing three columns of data. The columns contain the velocity, acceleration and travel time values for the pulling stage. This tells the stage to accelerate to the stated velocity and travel at this velocity for the given time period. The position of the stage can be read out after each entry to allow the user to know where the stage was at the time. The user can then calculate the velocity values the stage would have travelled at as well as create a velocity profile to then allow a comparison between the theoretical data and the actual recorded velocity data. Each velocity file was repeated 10 times to give a large set of data values to analyse.

### 3.4.2 Position set 1

Table 3.2 contains the first data set that included a range of increasing and decreasing velocity values to see how the stage behaves when fed a set of rapidly changing velocity values in a short period of time. Table 3.3 contains the calculated distance travelled and accumulated time values for the stage. Note that the final time interval value is zero which is necessary to bring the stage to a safe stop.

**Table 3.2:** The text file entered containing the velocity, acceleration and time values for data set 1.

Velocity (mm s <sup>-1</sup> )	Acceleration (mm s <sup>-2</sup> )	Time (ms)
50	20000	200
180	20000	200
120	20000	300
160	20000	200
20	20000	1000
110	20000	100
0	20000	0

**Table 3.3:** The theoretical data for the stage's velocity, time interval, acceleration time, accumulated time and distance travelled for data set 1. Note the non-integer values for the distance travelled is due to the acceleration time being taken into account.

Velocity (mm s <sup>-1</sup> )	Time interval (ms)	Acceleration time (ms)	Accumulated time (ms)	Distance travelled (mm)
50	200	2.5	202.5	10.063
180	200	6.5	409.0	46.485
120	300	3.0	712.0	82.575
160	200	2.0	914.0	114.615
20	1000	7.0	1921.0	135.105
110	100	4.5	2025.5	146.308
0	0	5.5	2031.0	146.610

Table 3.4 contains a 10 run average of the experimental distance travelled, time interval and accumulated time of the stage. Using the values in table 3.4, one can obtain other values such as the velocity the stage travelled at in this time period, the acceleration time and the change in velocity. Figure 3.31 shows the 10 runs and the calculated theory data that were obtained.

**Table 3.4:** A 10 run average obtained containing the distance travelled, time interval between positions, the accumulated time and velocity values for data set 1.

Distance travelled (mm)	Time interval (ms)	Accumulated time (ms)	Velocity (mm s <sup>-1</sup> )
11.329	231.4	231.4	48.958
48.253	208.1	439.5	177.435
84.972	304.8	744.3	120.470
117.494	203.8	948.1	159.574
138.355	1008.8	1956.9	20.679
149.728	106.2	2063.1	107.098
150.188	0	2068.5	0

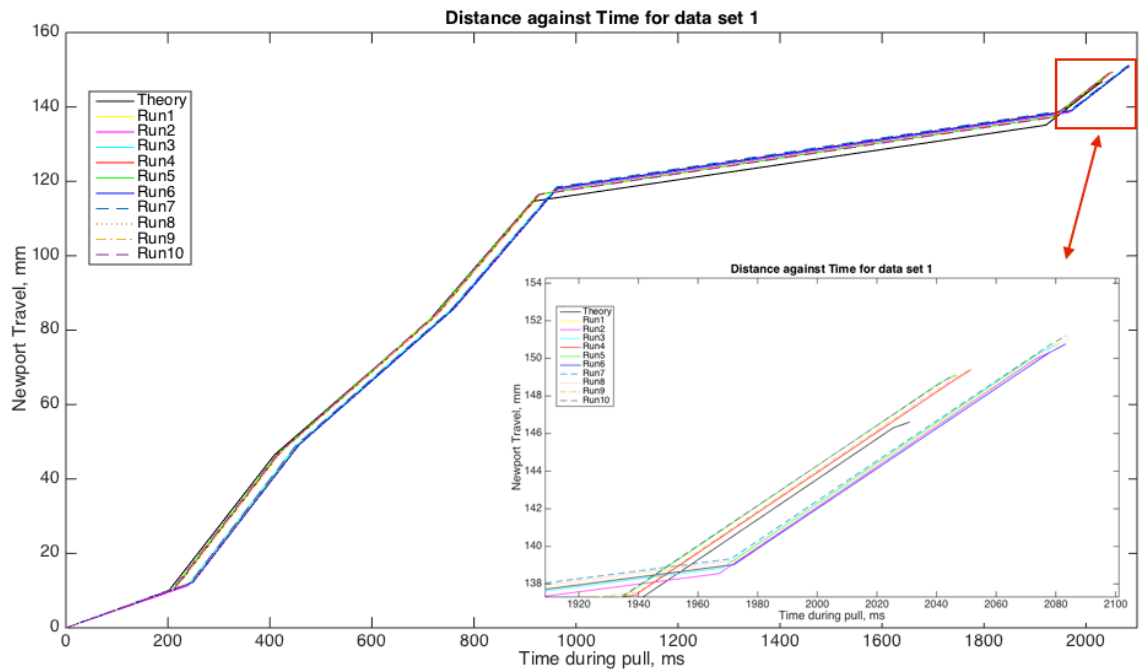


**Figure 3.31:** Distance against time for the 10 runs obtained with data set 1

**Table 3.5:** The position readings for each entry for all 10 runs.

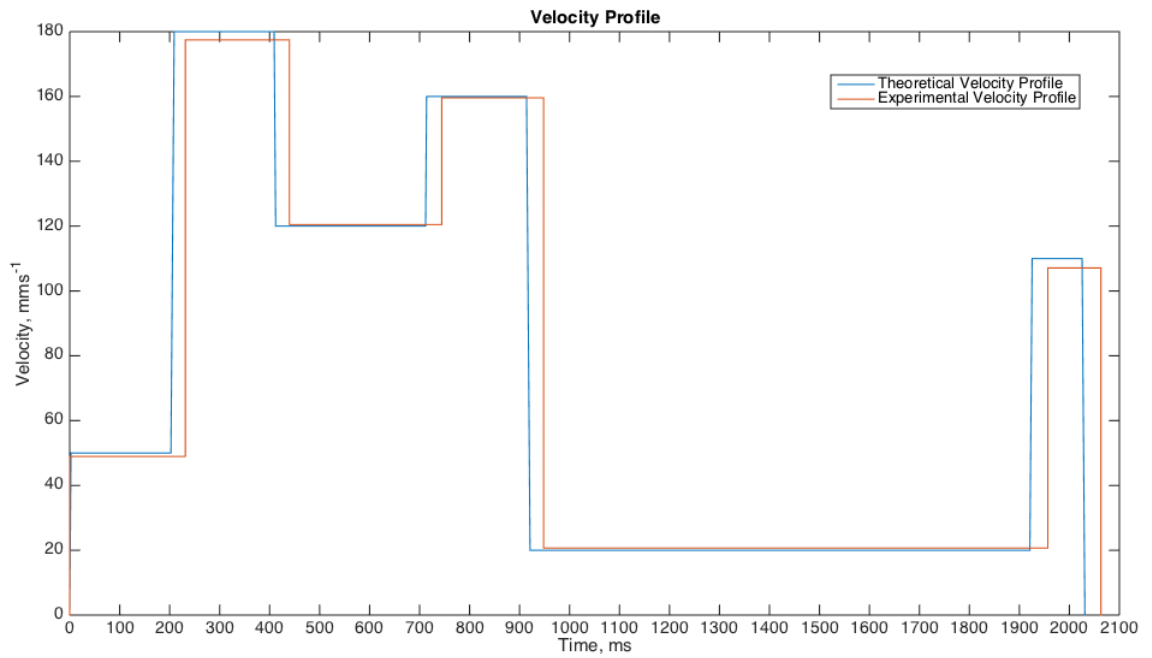
Run 1	Run 2	Run 3	Run 4	Run 5
0	0	0	0	0
11.975	11.400	12.007	10.489	10.276
48.804	48.328	48.869	47.404	47.123
85.576	85.130	85.531	84.072	83.894
118.124	117.706	117.947	116.604	116.471
139.020	138.549	138.844	137.412	137.333
150.416	149.939	150.240	148.848	148.684
150.871	150.353	150.695	149.373	149.113
Run 6	Run 7	Run 8	Run 9	Run 10
0	0	0	0	0
12.238	11.976	12.231	10.482	10.237
49.166	49.007	49.168	47.452	47.213
85.795	85.800	85.825	84.124	83.977
118.196	118.471	118.374	116.675	116.367
139.021	139.334	139.287	137.573	137.172
150.320	150.719	150.595	148.969	148.551
150.761	151.188	151.022	149.425	149.076

Figure 3.32 shows the velocity profile for the pulling stage. Table 3.5 shows the

position readings for every entry for all ten runs. Table 3.6 shows the standard deviation between these position values at each entry and the largest difference between the stage positions at each entry for the data for the 10 runs. The largest difference between stage positions occurs after the first entry of 2.001 mm with a standard deviation of 0.859. The following position readings however have a maximum position difference range between 0.108 mm and 0.281 mm and a standard deviation range of 0.038 and 0.090.

**Table 3.6:** The standard deviation and largest difference value of the stage position for the 10 runs at each entry for data set 1.

Standard Deviation	Largest difference (mm)
0.859	2.001
0.059	0.184
0.066	0.173
0.090	0.281
0.039	0.108
0.042	0.137
0.038	0.111



**Figure 3.32:** The theoretical velocity profile and the 10 run average velocity profile for the pulling stage.

The offset in the first entry is seen in figure 3.32. This offset in the first entry takes the value of 31.4 ms for the 10 run average, with subsequent time offsets taking values between 4 and 8 ms. This delay can be a significant factor when considering high speeds. At high velocities, a delay in velocity change of 30 ms can cause the stage to travel a significantly greater distance than that expected. This can be seen when comparing the distance travelled values in tables 3.2 and 3.4. A simple solution to this issue is to have the first entry a zero value such the following entires would not experience the large offset at the start. This solution was used in the production of the fibres in Chapter 4. However, this was not carried out at this point due to the authors interest to see if this delay will vary depending on starting velocity or if it is a constant.

### 3.4.3 Position set 2

The second data set, shown in table 3.7 focused on a gradual build up to  $10 \text{ mms}^{-1}$  with long intervals between each data entry. Table 3.8 shows the calculated distance the stage would travel as well as the accumulated time.

Table 3.9 contains a 10 run average of the distance travelled, the velocity, time interval and accumulated time of the stage. It was predicted that the slower speed with a gradual build up and longer time intervals would mean that the initial timing offset experienced in the previous set would have a smaller affect on the total distance travelled by the pulling stage, though the value of this initial offset might still be the same. This was the case as the timing offset was 31.2 ms and due to the slow initial velocity, the extra distance travelled was only approximately 50  $\mu\text{m}$ .

**Table 3.7:** The text file entered containing the velocity, acceleration and time values for data set 2.

Velocity ( $\text{mm s}^{-1}$ )	Acceleration ( $\text{mm s}^{-2}$ )	Time (ms)
2	20000	3000
4	20000	3000
6	20000	3000
8	20000	3000
10	20000	3000
0	20000	0

**Table 3.8:** The theoretical data for the stage's velocity, time interval, acceleration time, accumulated time and distance travelled for data set 2.

Velocity ( $\text{mm s}^{-1}$ )	Time interval (ms)	Acceleration time (ms)	Accumulated time (ms)	Distance travelled (mm)
2	3000	0.1	3000	6.000
4	3000	0.1	6000	18.000
6	3000	0.1	9000	36.000
8	3000	0.1	12000	60.000
10	3000	0.1	15000	90.000
0	0	0.5	15000	90.003

**Table 3.9:** The text file obtained containing the distance travelled, time interval between positions, the accumulated time and velocity values for data set 2.

Distance travelled (mm)	Time interval (ms)	Accumulated time (ms)	Velocity ( $\text{mm s}^{-1}$ )
6.054	3031.2	3031.200	1.997
18.059	3002.2	6033.400	3.999
36.070	3003.0	9036.400	5.998
60.084	3002.2	12038.600	7.999
90.099	2002.1	15040.700	9.998
90.115	0	15040.716	0

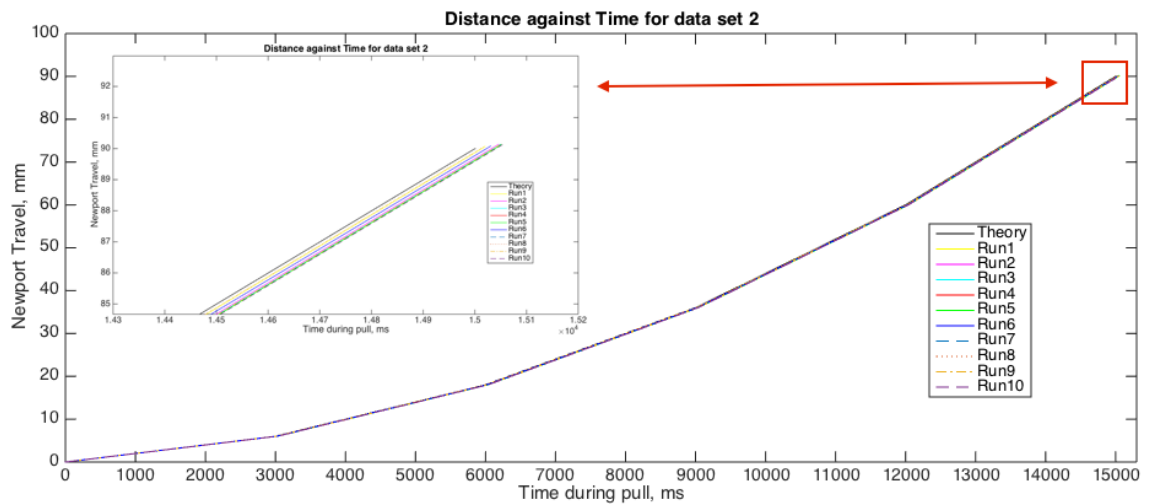


**Figure 3.33:** Distance against time for the 10 runs obtained with data set 2.

Figure 3.33 shows the 10 data runs and the calculated control run for the positions of the stage after each entry. Figure 3.34 shows the theoretical and experimental velocity profiles for the stage. Table 3.10 shows the standard deviation of the position of the stage and the largest difference between the stage positions at each entry for the data for the 10 runs. The first entry again has the largest values for both the standard deviation and the largest position difference of 0.026 and 0.072 mm respectively. The standard deviation for the following entries for the 10 data runs ranged between 0.001 and 0.007 and a maximum position difference 0.005 and 0.022 mm.

**Table 3.10:** The standard deviation and largest difference value of the stage position for the 10 runs at each entry for data set 2.

Standard Deviation	Largest difference (mm)
0.026	0.072
0.001	0.005
0.007	0.022
0.005	0.015
0.003	0.012
0.002	0.007

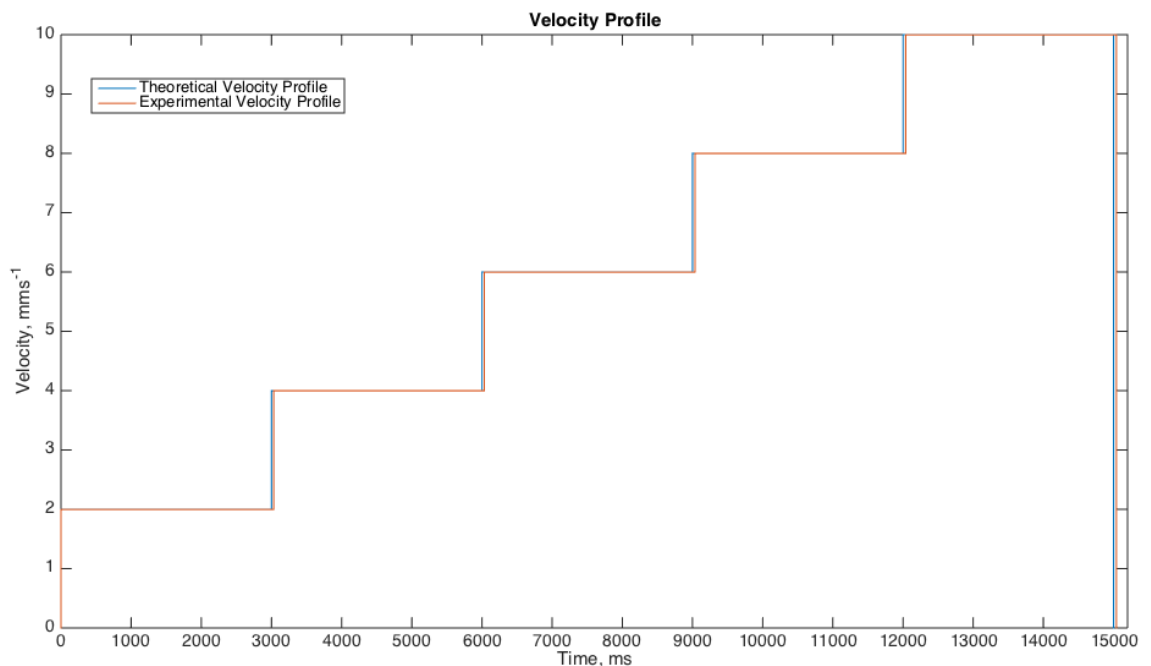


**Figure 3.34:** The theoretical velocity profile and the 10 run average velocity profile for the pulling stage.

### 3.4.4 Position set 3

The third data set followed the same theme as the second set, this time with increased speeds and shorter time intervals between data entries. Tables 3.11 and 3.12 show the third data set and the calculated values respectively. Table 3.13 shows the data obtained over a 10 run average for the distance travelled, velocity, time interval and accumulated time of the stage.

**Table 3.11:** The text file entered containing the velocity, acceleration and time values for data set 3 along with the calculated distances travelled by the stage.

Velocity (mm s <sup>-1</sup> )	Acceleration (mm s <sup>-2</sup> )	Time (ms)
20	20000	500
40	20000	500
60	20000	500
80	20000	500
100	20000	500
0	20000	0

**Table 3.12:** The theoretical data for the stage's velocity, time interval, acceleration time, accumulated time and distance travelled for data set 3.

Velocity (mm s <sup>-1</sup> )	Time interval (ms)	Acceleration time (ms)	Accumulated time (ms)	Distance travelled (mm)
20	500	1	500	10.010
40	500	1	1000	30.020
60	500	1	1500	60.030
80	500	1	2000	100.040
100	500	1	2500	150.050
0	0	5	2500	150.300

**Table 3.13:** The text file obtained containing the distance travelled, time interval between positions, the accumulated time and velocity values for data set 3.

Distance travelled (mm)	Time interval (ms)	Accumulated time (ms)	Velocity (mm s <sup>-1</sup> )
10.742	542.0	542.00	19.820
30.837	503.2	1045.20	39.934
60.981	503.4	1548.60	59.882
101.179	502.9	2051.50	79.932
151.522	502.3	2555.80	99.828
151.992	0	2560.79	0

Figure 3.35 shows the 10 data runs and the calculated control run for the positions

of the stage after each entry. Figure 3.36 shows the velocity profile obtained for this data set. Table 3.14 shows the standard deviation of the position of the stage and the largest difference between the stage positions at each entry for the data for the 10 runs. Unlike the previous two data sets, the first entry had the lowest standard deviation and the smallest maximum difference in stage position instead of the largest. The first entry still however still had a time offset, 42 ms in this instance, further indicating that this is intrinsic to the method of operation. The standard deviation of each entry for the 10 runs had a range between 0.038 and 0.253 and a largest position difference between 0.132 and 0.731 mm. It should be noted that the large standard deviation and position difference value in the final entry was due to run 7 traveling for slightly longer, approximately 9 ms longer than the other runs. This data set has the largest standard deviation in the final two entries, which can be attributed to the final entries in run 7.

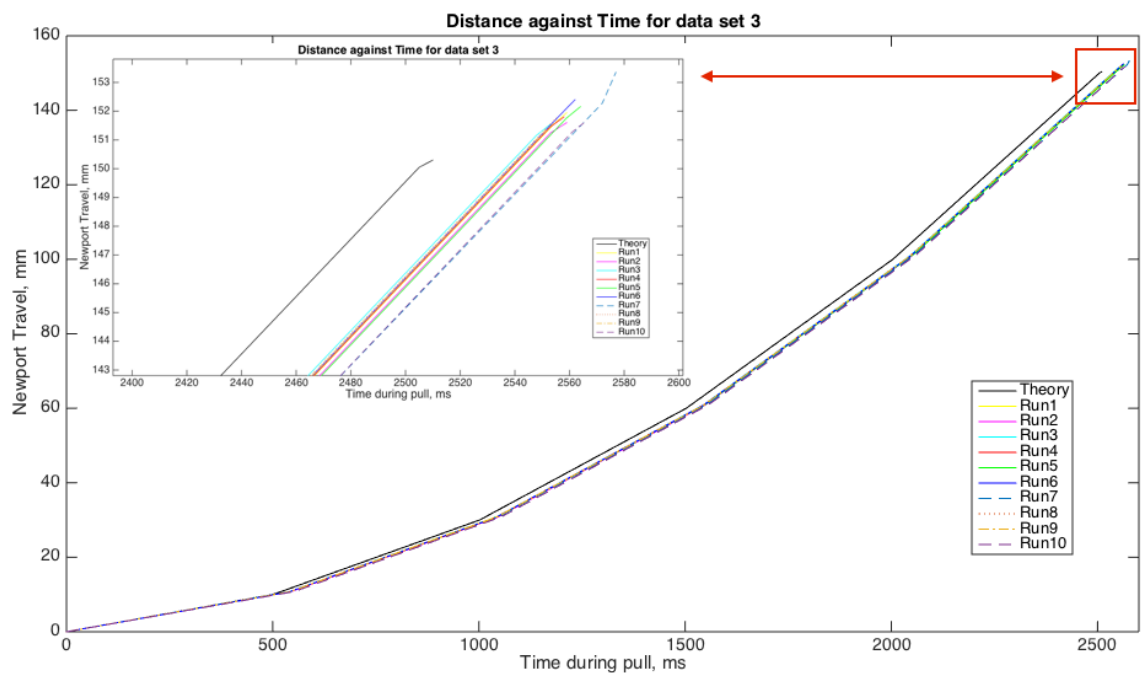


**Figure 3.35:** Distance against time for the 10 runs obtained with data set 3.

**Table 3.14:** The standard deviation and largest difference value of the stage position for the 10 runs at each entry for data set 2.

Standard Deviation	Largest difference (mm)
0.038	0.132
0.086	0.286
0.053	0.146
0.069	0.207
0.253	0.731
0.218	0.725

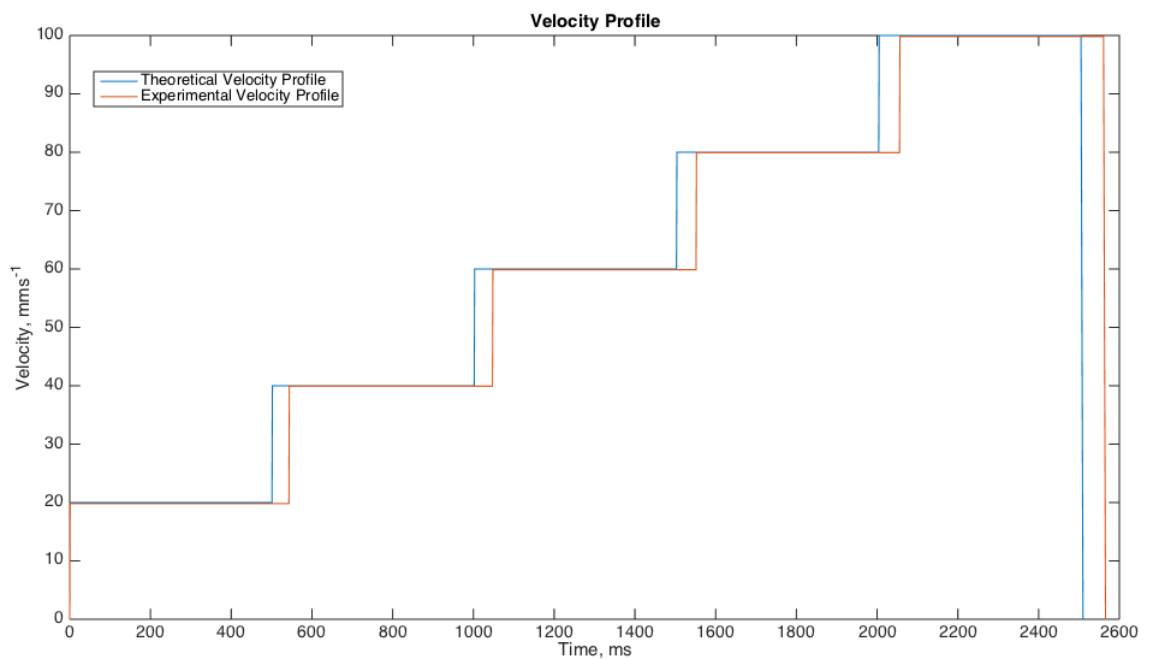


**Figure 3.36:** The theoretical velocity profile and the 10 run average velocity profile for the pulling stage.

### 3.4.5 Improvements and conclusion

It was found that the first entry of the velocity file uploaded to LabVIEW would involve a time delay, ranging between 31.2 and 42.0 ms. This can be avoided by making the first entry a value that moves the stage a negligible amount for a time greater than the delay. Time delays for following entries would vary, however the delays would all be less than 10 ms. Data set 1 ranged between 3.8 and 8.8 ms where the velocity would increase and decrease rapidly. Data set 2 ranged between 2.1 and 3.0 ms and data set

3 ranged between 2.3 and 3.4, though the velocity in these two sets would gradually increase.

The time offset in the first entry would also cause the total travel distance to be greater than the calculated travel distance. Data set 1, 2 and 3 had an average longer travel distance of 3.578 mm, 0.112 mm and 1.692 mm. This however can be eliminated by the method mentioned previously of having a negligible velocity value for the first entry.

In the future, an independent position encoder will be installed to give position measurements out with the LabVIEW program to ensure that the internal encoder is giving out true positional values. This allow the two obtained velocity values of the stage to be calculated and compared. A timing program will be added as well to monitor the timing of each loop iteration to ensure the program is running as efficiently as possible.

# Chapter 4

## Fibre production - one stage pull

The aim of this pulling machine is to produce small diameter ( $\leq 20 \mu\text{m}$ ) fibres for use in advanced gravitational wave prototype detectors. This chapter will focus on fibres that were produced via 1 stage pulls, meaning that the pulling process is completed through the use of one velocity profile to pull the silica stock to the desired diameter. The fibres produced from the pulling machine are then profiled to determine the shape and diameter of the fibres, then put into a destructive strength tester to determine the ultimate breaking stress of the fibres. The shaping of the fibres required a lot of development over several batches of fibres. Therefore only a few select batches of fibres produced will be discussed in full detail covering the full profile and strength testing analysis.

### 4.1 Absolute position pull method

The first set of fibres were produced without the use of a velocity profile, as discussed in the previous chapter, but through the use of instructing the pulling stage to move to an absolute position at a set speed and acceleration. This was an opportunity to investigate the fibres that would be produced when using the stage's maximum velocity and acceleration values,  $500 \text{ mms}^{-1}$  and  $26,000 \text{ mms}^{-2}$  respectively. In this

case, 3 different lengths of fibres were chosen to investigate: 10 cm, 15 cm and 20 cm. Each set of fibres would consist of 3 fibres to allow comparisons for within each length set.

#### 4.1.1 Fibre pulling procedure

The fused silica stock used had a diameter of approximately 2mm and was heated up using the 100 W CO<sub>2</sub> laser until it is sufficiently hot enough to proceed with the pull, as shown in figures 4.1 and 4.2. The stage would then move to the stated position to produce a fibre. Once the fibre has been pulled successfully, the feed mirror is moved by its motorised stage towards the first conical mirror mount to allow two metal rods to be connected to either end of the fibre clamps to create a ‘fibre cartridge’. The use of a fibre cartridge [62], shown in figure 4.3, allowed safe transportation of the fibre around the laboratory for characterisation purposes. To extract the fibre once the fibre cartridge is in place, the LabVIEW program that is controlling the stages is turned off, and the grub screws holding the clamps are loosened. Turning off the LabVIEW program cuts the power to the pulling stage, allowing the user to manoeuvre the stage by hand to then slide out the fibre clamps from their holders.

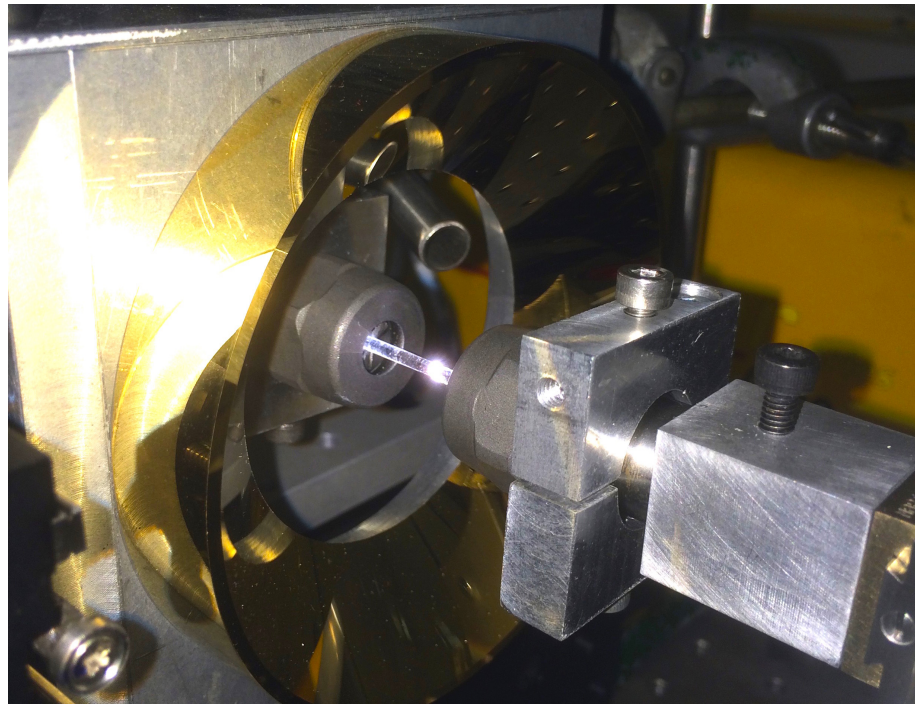


**Figure 4.1:** The silica stock being heated by the CO<sub>2</sub> laser.

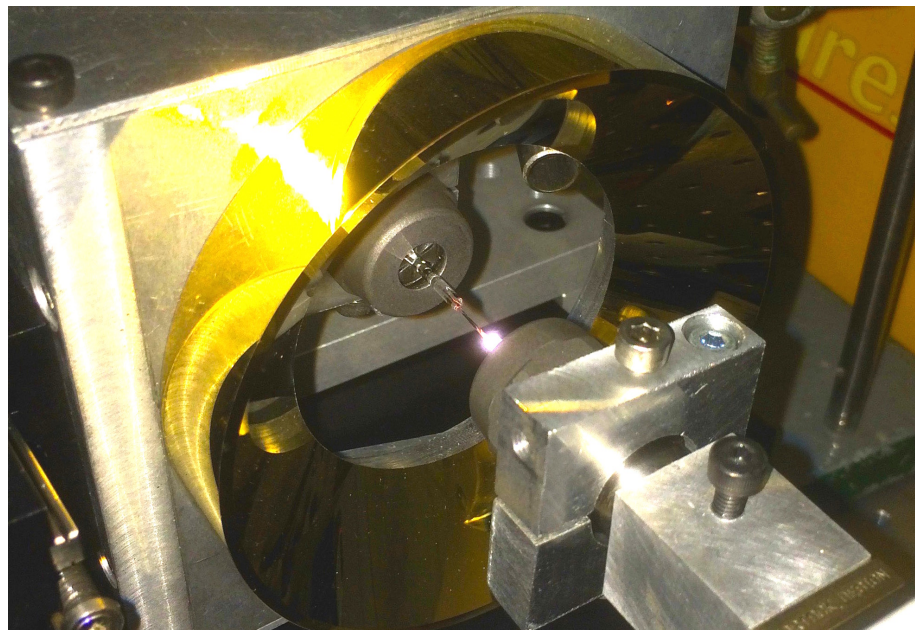


**Figure 4.2:** The pulling stage beginning the pull of a fibre.

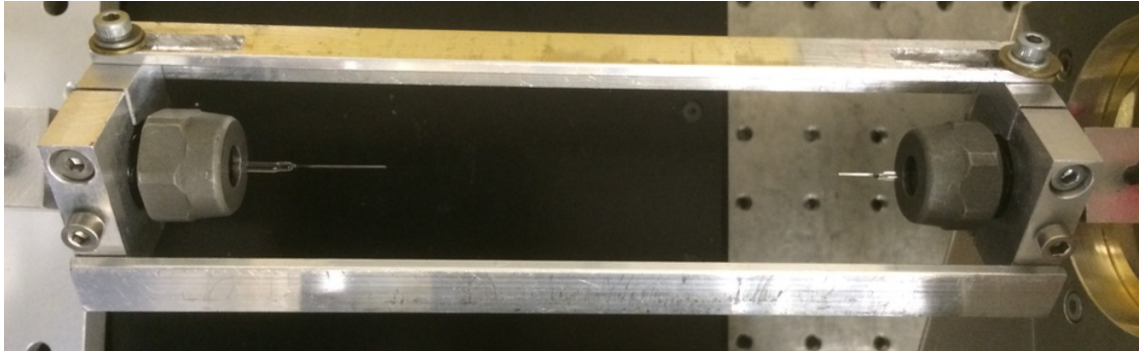


**Figure 4.3:** The fibre cartridge that is used to transport the silica fibre around the laboratory.

### 4.1.2 Fibre profiles and analysis

Once the fibres have been produced, their geometries are profiled using a fibre profiler [63], shown in figure 4.4. This profiler works by imaging the fibre using 2 cameras, one with low magnification and another with high magnification and calculates the width of the fibre through a shadow sensing measurement of the edge positions. The low magnification was used to profile the thick end section of the stock and the high magnification camera was used to profile the thin central section. While using the high magnification camera, the user can set the distance between the data points along the fibre.

As the profiler was not designed to profile such thin fibres, the profiler had to be calibrated to help gauge the error that would be applicable to the measurement of the thin fibre diameters. This was achieved by profiling a length of wire with a width of  $25 \pm 1.25 \mu\text{m}$ . Using the high magnification camera, 10 readings were taken, shown in table 4.1, and the difference between the profiler and stated width were calculated. This resulted in a systematic error of 15 % and a scaling ratio of 0.869 that was applied to the profiler.

**Table 4.1:** The profiler data for a length of wire with a diameter of  $25 \pm 1.25$   $\mu\text{m}$

Profiler wire diameter ( $\mu\text{m}$ )	Wire diameter ( $\mu\text{m}$ )	Profiler Average ( $\mu\text{m}$ )
28.82	$25 \pm 1.25$	28.759
28.79		
28.73		
28.69		
28.73		
28.75		
28.84		
28.78		
28.74		
28.72		

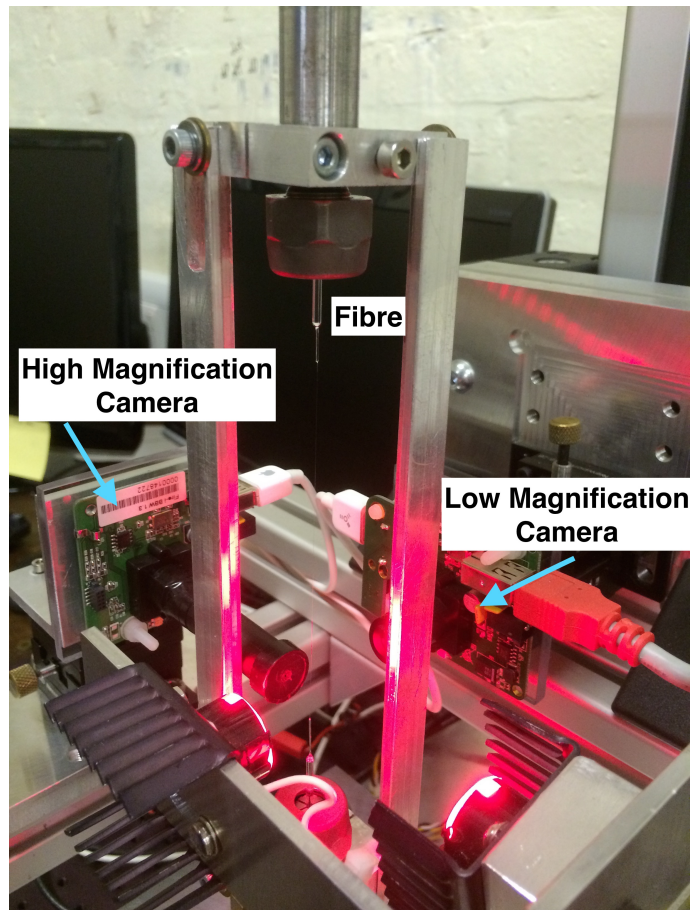


**Figure 4.4:** The fibre profiler used to find the width of the fibres produced.

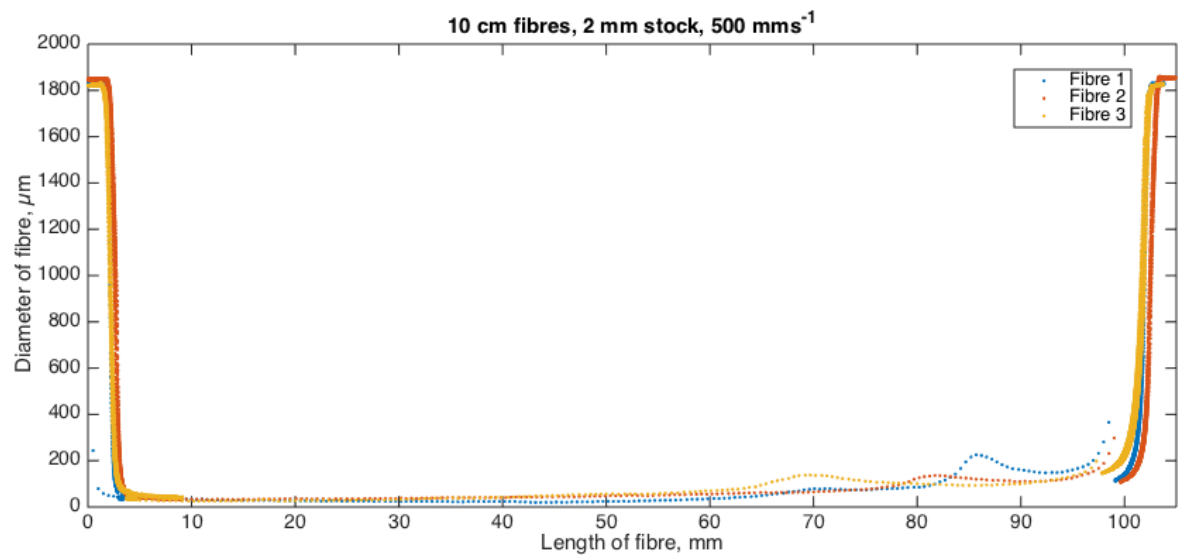


**Figure 4.5:** Profiles of three 10 cm long fibres.

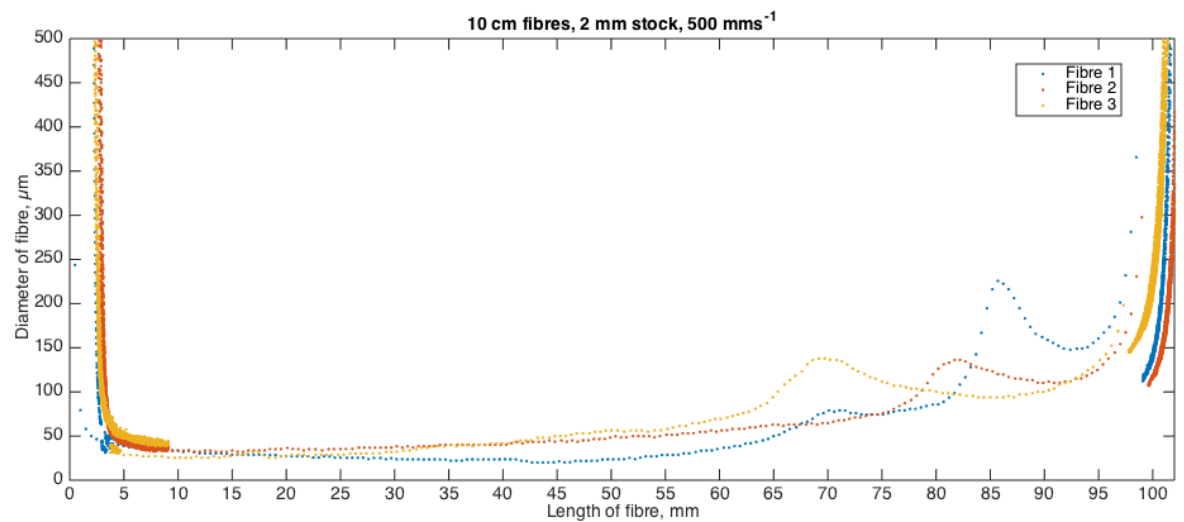


**Figure 4.6:** A zoomed in graph of the three 10 cm long fibre profiles.

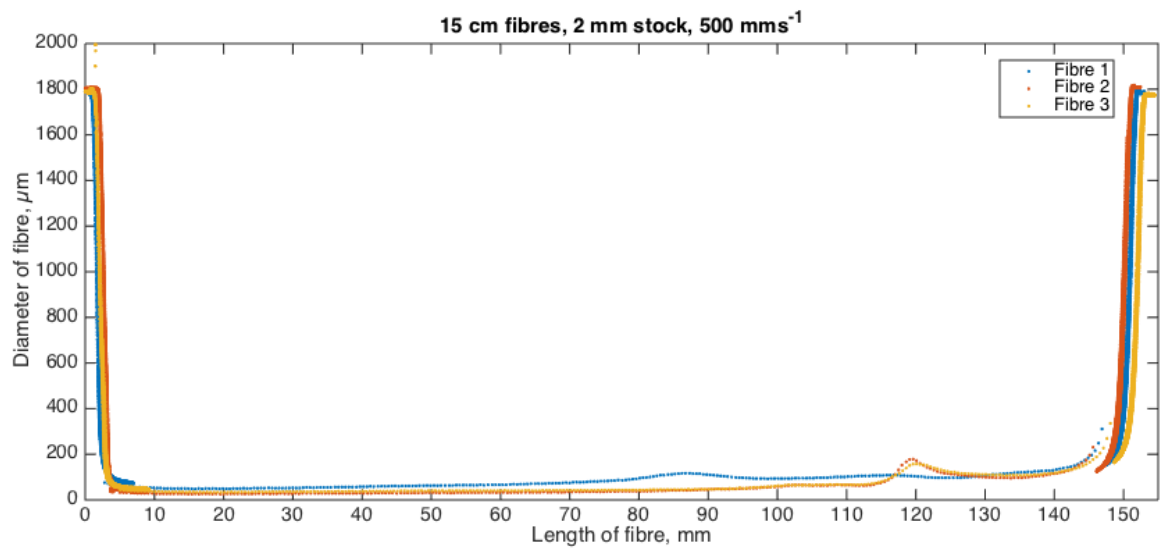


Figure 4.7: Profiles of three 15 cm long fibres.

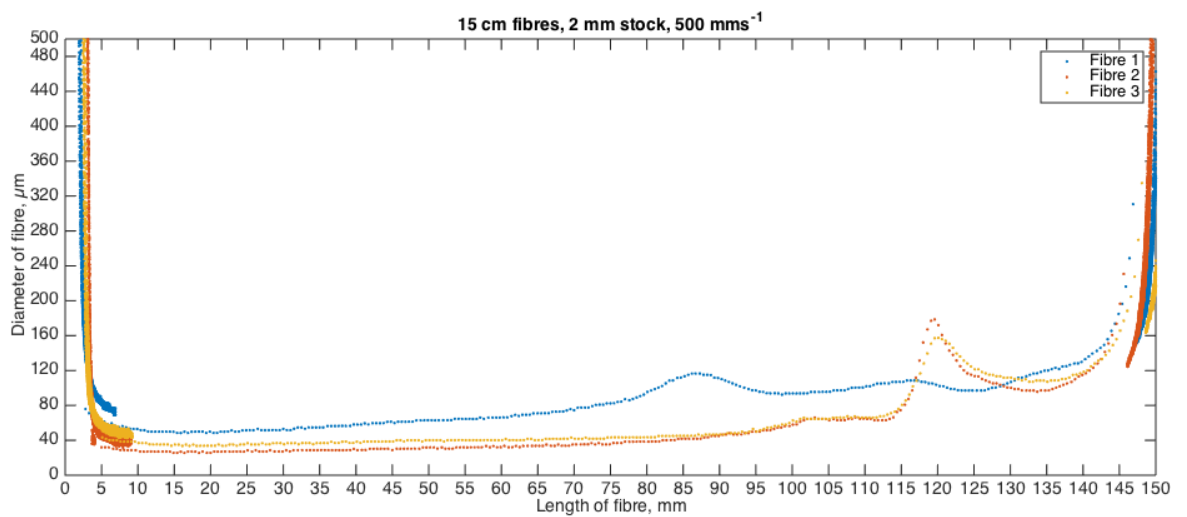


Figure 4.8: A zoomed in graph of the three 15 cm fibre profiles.

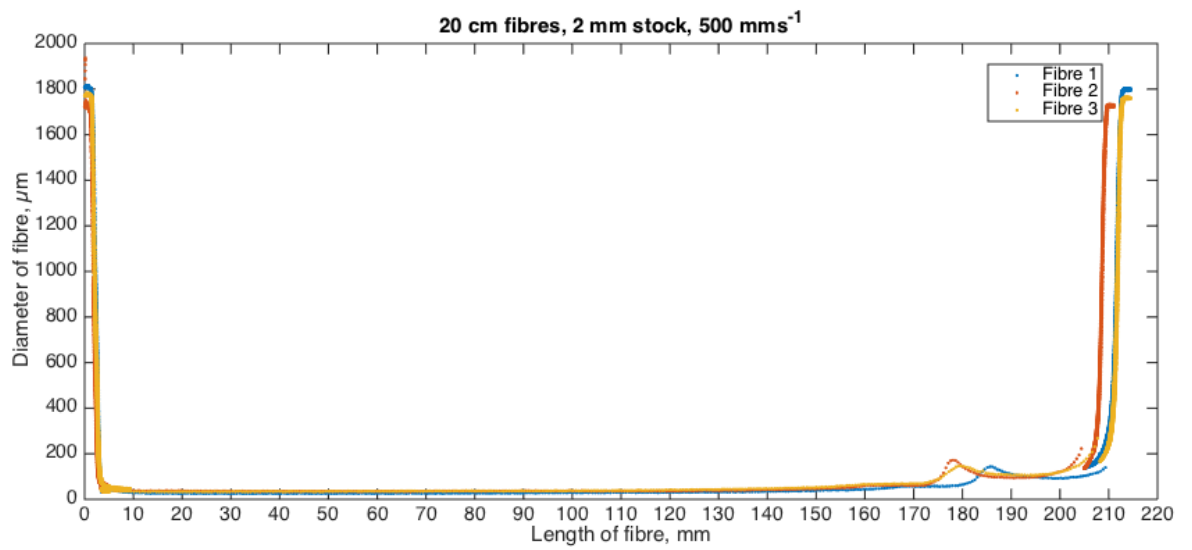


Figure 4.9: Profiles of three 20 cm long fibres.

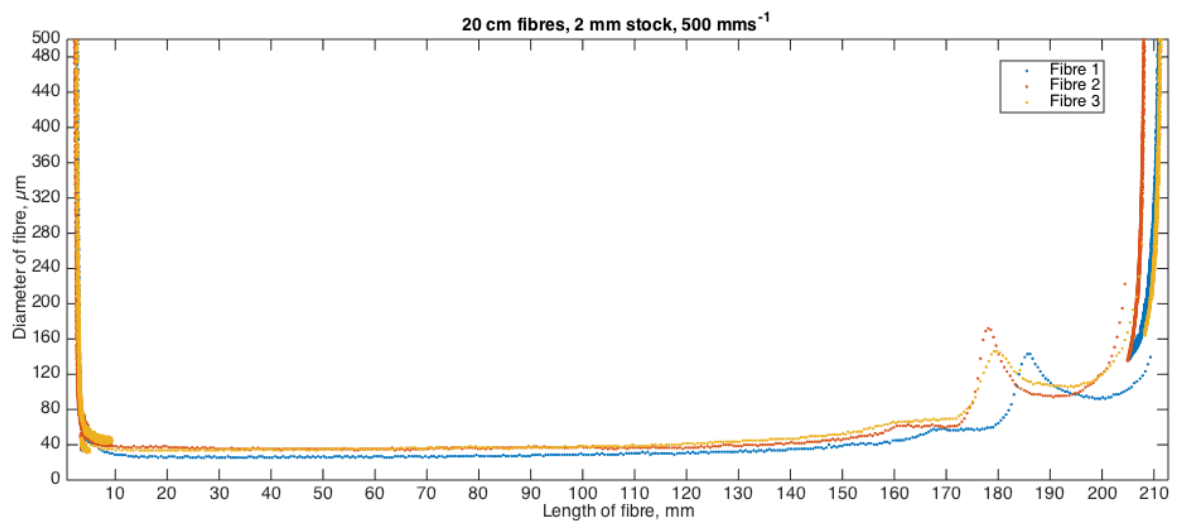


Figure 4.10: A zoomed in graph of the three 20 cm fibre profiles.

Figures 4.5 to 4.6 show the fibre profiles for the 10 cm fibres, figures 4.7 to 4.8 show the fibre profiles for the 15 cm fibres and figures 4.9 to 4.10 show the fibre profiles for the 20 cm fibres. On the graph, the left hand side of the fibre is the end that is stationary during the pull and the right hand side of the fibre is the end that is on the pulling stage. This will be the case for all fibre profile graphs in this thesis. Using the method of moving the stage straight to an absolute position at maximum velocity and acceleration result in fibres that are far from uniform along their length. The fibres appear to taper down as the pull proceeds and share a similar artefact of having a large bump on the right hand side of the graph. The point at where this bump appears varies, with the exception of fibres two and three in both the 15 cm and 20 cm batches, where they appeared in the same region. Through further investigation, it appeared that this bump would occur if the stage was initially accelerated quickly to a high velocity. If the velocity was gradually increased instead of a fast acceleration to the high velocity, the user would have greater control over the fibre shape to eliminate this bump.

**Table 4.2:** The minimum values of the fibre diameters that were pulled via the absolute position method.

Fibre Batch	Fibre Number	Fibre Minimum Diameter ( $\mu\text{m}$ )
10cm	1	20
10cm	2	32
10cm	3	25
15cm	1	48
15cm	2	26
15cm	3	34
20cm	1	25
20cm	2	34
20cm	3	31

Table 4.2 shows the minimum diameters of the fibres after profiling. These values have a large variation to them, with the biggest difference being between fibre 1 and fibre 2 from the 15 cm batch, with a difference of 22  $\mu\text{m}$ . Since the aim of this pulling machine is to produce thin, repeatable and uniform fibres, it is clear that pulling fibres via an absolute position move at one velocity is not a suitable method. This was however expected.

## 4.2 Velocity profile pull method

The set of fibres that will be discussed in this section were produced using a velocity profile, similar to that discussed in the previous chapter. The aim of this was to see how thin and repeatable a fibre can be when produced with a one stage pull.

### 4.2.1 Velocity profile for the fibre pull

The fibres produced in this section were created using the velocity profile in table 4.3. It consisted of sharp high velocity changes at high accelerations and extremely short time intervals designed to push the stage and the LabVIEW program in its current form to its limit. To counter the time offset that was experienced in the previous chapter with regards to the first entry of the velocity data, a velocity value of  $0.01 \text{ mm s}^{-1}$  was used for a time of 960 milliseconds. This time value was chosen as the previous results indicated a delay ranging from 30 to 40 milliseconds meaning that the main part of the pull should commence after 1000 milliseconds, as shown in table 4.4. This would result in a fibre theoretically being produced in 535 milliseconds and with a length of 93 mm.

**Table 4.3:** The text file entered containing the velocity, acceleration and time values for the 1 stage pull.

Velocity (mm s <sup>-1</sup> )	Acceleration (mm s <sup>-2</sup> )	Time (ms)
0.01	20000	960
50	20000	50
55	20000	50
60	20000	75
70	20000	100
120	20000	150
380	20000	10
400	20000	10
420	20000	10
440	20000	10
460	20000	10
480	20000	10
490	20000	50
0	20000	10

**Table 4.4:** The theoretical data for the stage's velocity, time interval, acceleration time, accumulated time and distance travelled for the velocity profile. Note the predicted 40 ms delay is taken into account.

Velocity (mm s <sup>-1</sup> )	Time interval (ms)	Acceleration time (ms)	Accumulated time (ms)	Distance travelled (mm)
0.01	1000	0.0005	1000.0005	0.010
50	50	2.50	1052.50	2.572
55	50	0.25	1102.75	5.323
60	75	0.25	1178.00	9.823
70	100	0.53	1278.53	16.826
120	150	2.63	1431.16	34.892
380	10	13.68	1454.84	40.471
400	10	1.05	1465.89	44.481
420	10	1.05	1476.94	48.692
440	10	1.05	1488.00	53.102
460	10	1.05	1499.05	57.713
480	10	1.05	1510.10	62.524
490	50	0.53	1560.63	87.026
0	0	24.50	1595.13	93.028

### 4.2.2 Fibre profiles and analysis

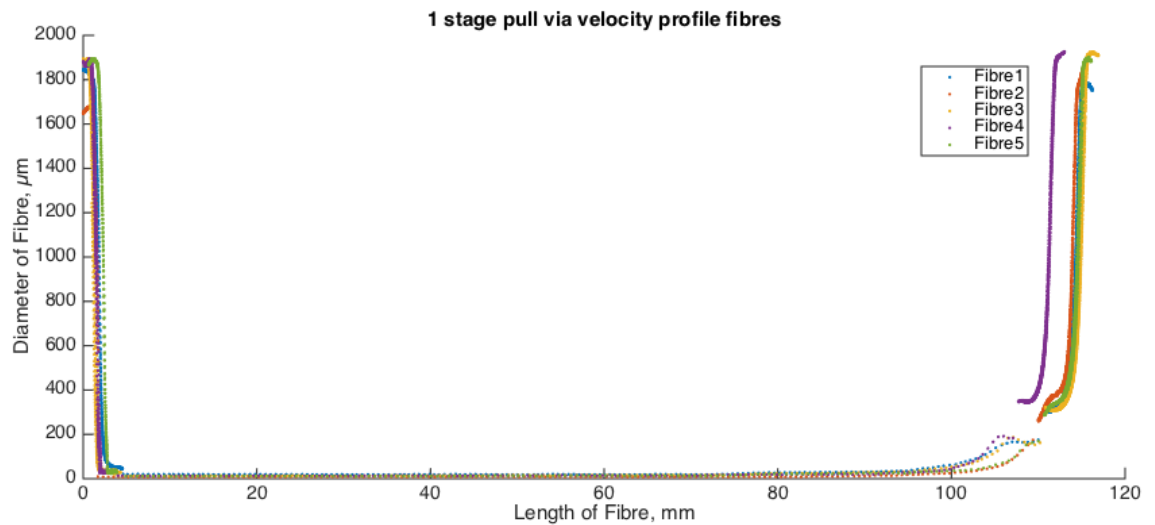


**Figure 4.11:** The profile of 5 fibres pulled with the velocity profile in table 4.3.

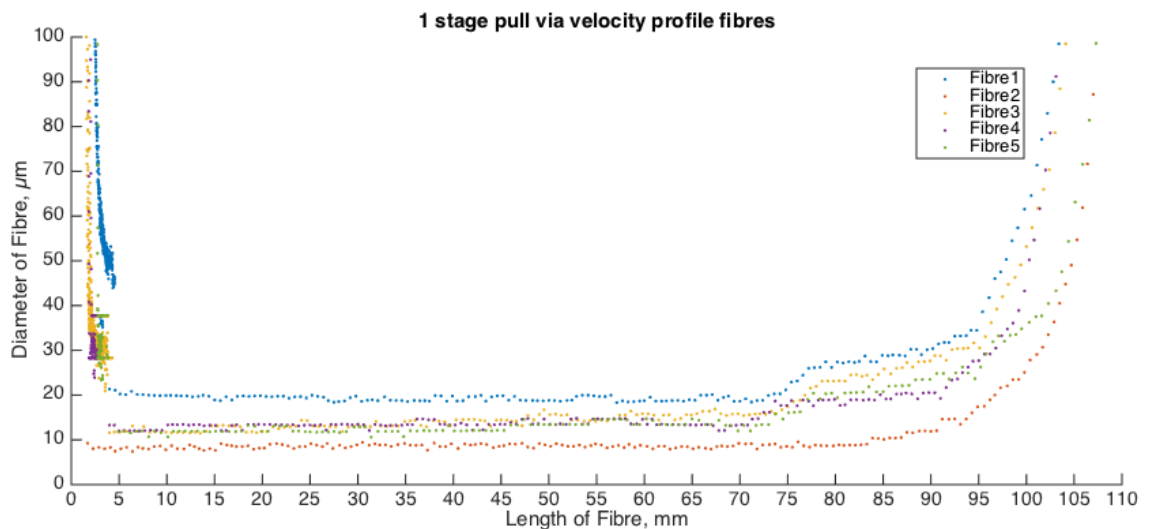


**Figure 4.12:** A zoomed in image of figure 4.11.

Figures 4.11 to 4.12 show the profiles for the 5 fibres that were produced using the velocity profile stated in table 4.3. The minimum diameter of the fibres are shown in table 4.5. It should be noted that the build up of data points between 0 mm and 5 mm in the bottom left corner and the lack of data points between 105 mm and 110 mm were due to profiling techniques where the data switched from the low magnification

camera to the high magnification camera.

In figure 4.12, there is a slight variation that can be observed in the width of the fibre. This can be attributed to the fact that as the fibres are being profiled, the camera position needs to change to keep the fibre in focus. As these fibres are a lot thinner than the fibres that the profiler was designed for, it is more difficult to maintain focus on the fibre. This then leads to the slight variation seen as the fibres being in focus is subjective to the user profiling the fibres. Taking the standard deviation of the data points between 5 mm and 70 mm for each fibre in figure 4.12 gave the random error in the data due to the issue of keeping the fibre in focus. This error, converted to a percentage, is applied to the minimum diameter values of the fibres in table 4.5. This process of calculating the error was also applied to the fibres in the following chapter. The length of the fibre was measured by monitoring the start and end positions of the pulling stage with an error of  $\pm 0.005$  mm.

**Table 4.5:** The minimum diameter values and length of the fibres that were pulled.

Fibre Number	Fibre Minimum Diameter ( $\mu\text{m}$ )	Length of fibre (mm) $\pm 0.005$ mm
1	$18.3 \pm 0.6$	112.753
2	$7.4 \pm 0.4$	112.649
3	$11.5 \pm 1.5$	112.155
4	$12.0 \pm 0.7$	109.469
5	$10.6 \pm 1.0$	111.454

**Table 4.6:** The text file obtained containing the 5 run average distance travelled, time interval between positions, the accumulated time and velocities values for the velocity profile.

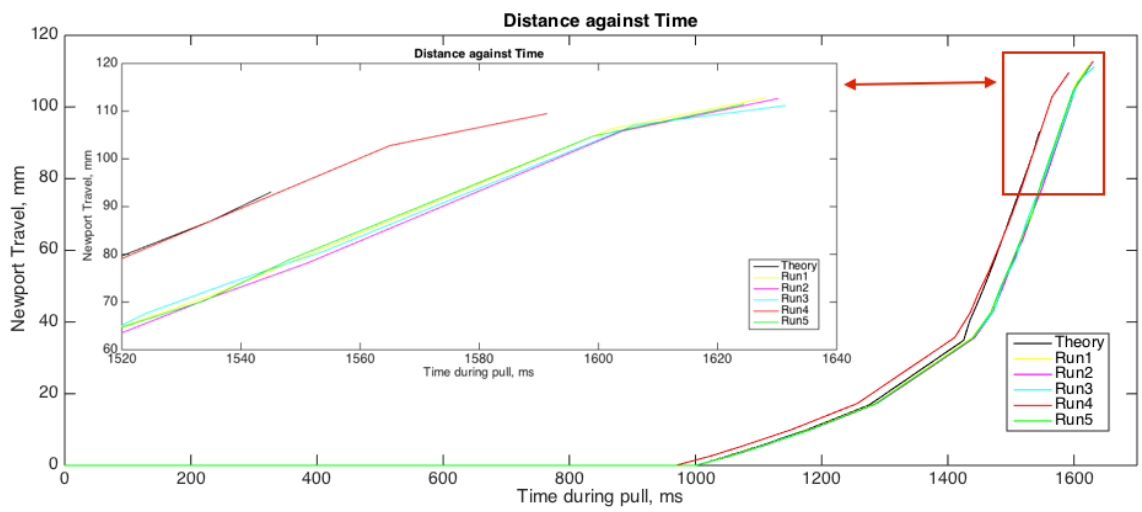
Distance travelled (mm)	Time interval (ms)	Accumulated time (ms)	Velocity ( $\text{mm s}^{-1}$ )
0.010	993.8	993.8	0.010
2.591	54.2	1048.0	47.619
5.479	52.2	1100.2	55.324
10.092	77.2	1177.4	59.763
17.230	102.4	1279.8	69.709
35.561	154.2	1434.0	118.874
42.756	29.6	1463.6	245.036
50.032	15.6	1479.2	465.195
56.384	16.4	1495.6	390.375
63.760	16.0	1511.6	461.025
70.995	16.4	1528.0	442.383
78.573	15.4	1543.4	493.942
105.329	51.8	1595.2	516.490
111.496	0	1595.2	0

All the fibres produced met the aim of having a thin section of width  $< 20 \mu\text{m}$ , but there was a range in minimum widths as shown in table 4.5. The thickest fibre was fibre 1 with a minimum diameter of  $18.3 \pm 0.6 \mu\text{m}$  and the thinnest was fibre 2 with a minimum diameter of  $7.4 \pm 0.4 \mu\text{m}$ . Fibres 3 to 5 had similar profiles with their minimum diameter ranging between  $10.6$  and  $12.0 \pm 1.0$  and  $0.7 \mu\text{m}$  respectively.

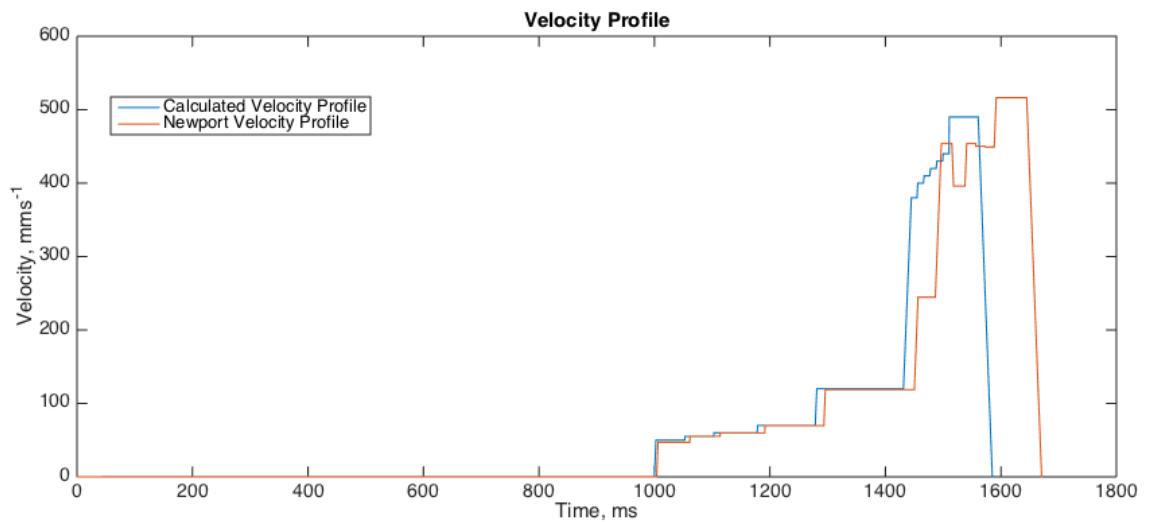
The predicted length of the fibres was  $93 \text{ mm}$ , however the fibres that were produced were significantly longer than this, ranging between  $109.469$  and  $112.753 \text{ mm}$  in length as shown in table 4.6 and figure 4.13. This can be attributed to the time intervals between entries, especially at the higher velocities. For example, if the stage is traveling at  $442 \text{ mm s}^{-1}$  for  $6.4 \text{ ms}$ , the stage would travel  $2.82 \text{ mm}$ . With the number of entries the loop in the LabVIEW program needs to go through, these small additions to the travel length will add up.

Figure 4.14 shows the theoretical velocity profile of the stage and a 5 run average

velocity profile from the position data obtained from the stage's encoder.



**Figure 4.13:** Distance against time for the pulling stage for each of the five fibre entires.



**Figure 4.14:** Theoretical velocity profile and 5 run average velocity profile used to create 1 stage fibres.

**Table 4.7:** The standard deviation and largest difference value of the stage position for the 5 fibres at each entry.

Standard Deviation	Largest difference (mm)
0.000	0.000
0.021	0.047
0.055	0.133
0.056	0.140
0.044	0.119
0.094	0.265
0.198	0.491
1.181	3.256
1.393	3.644
2.429	6.645
2.340	6.525
2.002	5.253
1.650	4.255
1.336	3.284

The stage does not seem to follow the build up in velocity when attempting to complete the entries for  $380 \text{ mm s}^{-1}$  onwards, shown in figure 4.14. The standard deviation of the position for the stage for all 5 fibre production runs is given in table 4.7. The standard deviation is small for velocities below  $120 \text{ mm s}^{-1}$ , but jumps up after  $380 \text{ mm s}^{-1}$ . This suggests it may be more favourable to run the stage at lower velocities with slightly longer time intervals.

This effect could be due to the fact that the LabVIEW program may not be able to keep up with writing out the position of the stage in the short time intervals (10 ms) in quick succession during the pull. A future solution to this is to install an independent position encoder that will read out the position of the stage. Comparing the two sets of data for the position of the stage during the pull will indicate where the problem lies.

Fibre four is noticeable for being the shortest of the five fibres produced. Looking at figure 4.13, there is one entry in the velocity profile, just after 1400 ms, where the

stage travels less than the other four fibres. The reason for this can be due to the fact that the stage might be traveling at a lower velocity compared to the other four as it seems to be following the path of the control data.

The sudden change in diameter that can be observed in figure 4.12 in the region 70 - 80 mm can be attributed to the sharp change in velocity between  $120 \text{ mm s}^{-1}$  and  $380 \text{ mm s}^{-1}$ . Fibre 2 however does not exhibit this behaviour, and through out the development of this velocity profile was the only fibre not to show this change in diameter. The reason for this is unknown, but could be due to a slight difference in the stock diameter at both ends of the fibre. By looking at figure 4.11, the stock at the stationary end has a diameter approximately 0.2 mm less than that on the pulling end. In the future, larger batches could be produced to see if this is more common, or if it just happened to be a one off.

### 4.2.3 Strength testing

The next stage of fibre characterisation is to strength test the fibres. This is achieved by placing a fibre into a strength testing apparatus [64], shown in figure 4.15, that will exert a force on a fibre until the fibre snaps. The clamps at either end of the fibre are placed into holders, one attached to a load cell and the other to a plate attached to a stepper motor. The stepper motor then pulls the plate down, causing the fibre to stretch, thus exerting a force on the load cell. The force applied to the load cell is then read out on a digital reader and the readings recorded until the fibre snaps.

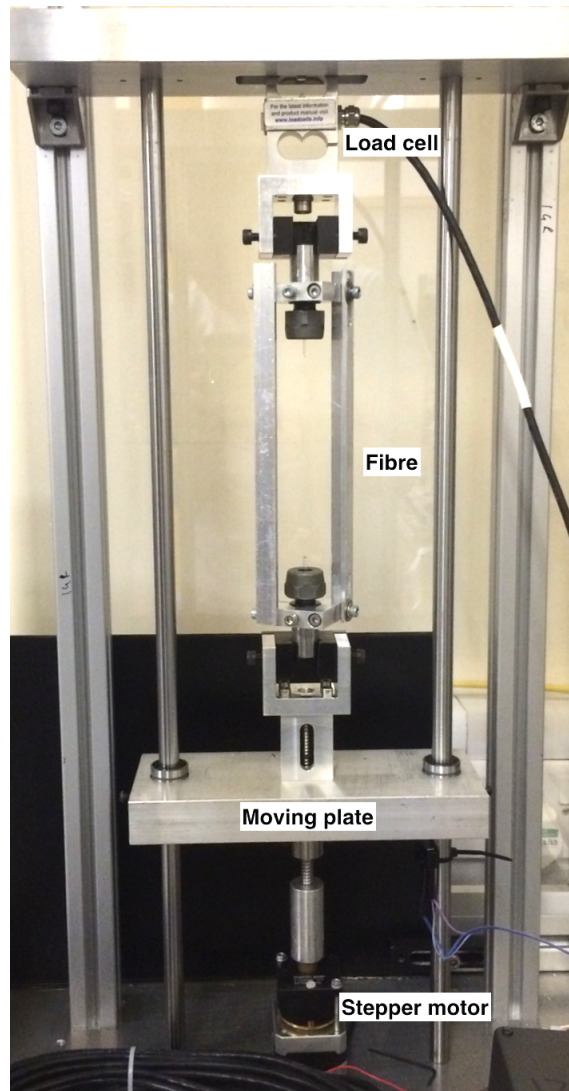


**Figure 4.15:** The strength tester used to break the silica fibres.

**Table 4.8:** The breaking force and breaking stress values for the five fibres.

Fibre Number	Breaking Force (N) $\pm 0.25\%$	Breaking Stress (Pa)
1	$1.599 \pm 0.004$	$6.05 \pm 0.39 (\times 10^9)$
2	$0.010 \pm 0.001$	$2.26 \pm 0.26 (\times 10^8)$
3	$0.422 \pm 0.001$	$4.07 \pm 0.53 (\times 10^9)$
4	$0.444 \pm 0.001$	$3.91 \pm 0.47 (\times 10^9)$
5	$0.334 \pm 0.001$	$3.78 \pm 0.35 (\times 10^9)$

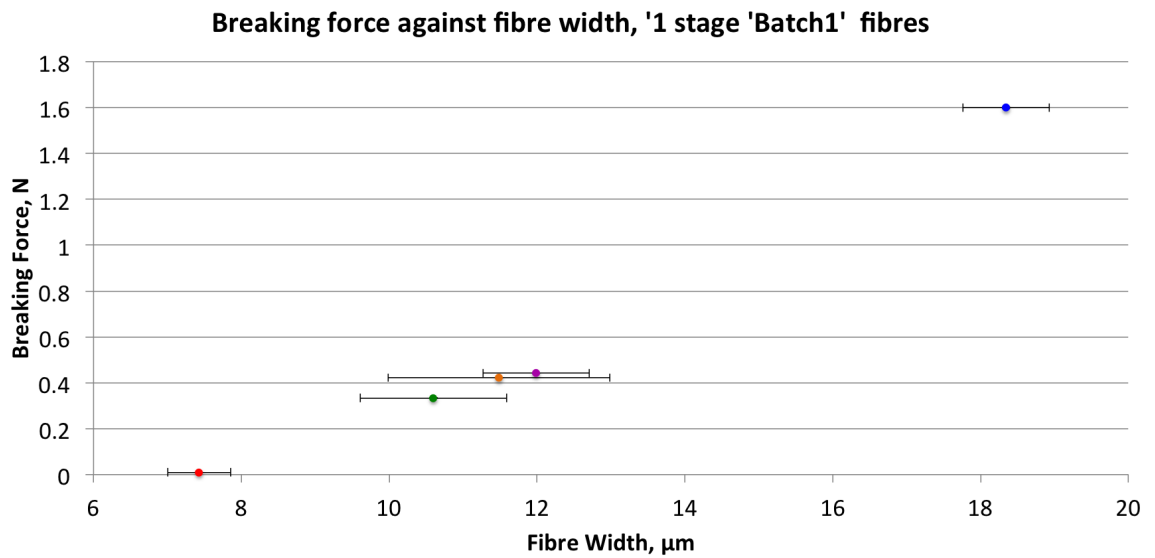


**Figure 4.16:** The force required to break all five fibres.

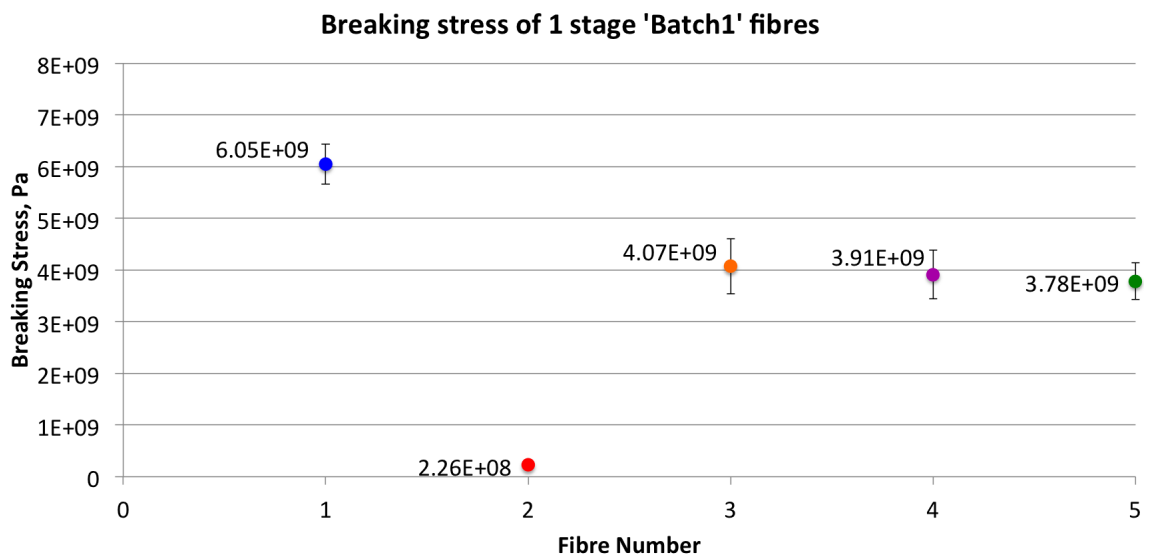


**Figure 4.17:** The calculated breaking stress of all five fibres.

Table 4.8 shows the breaking force and breaking stress values and their associated errors for the five fibres. It should be noted that fibres 2 and 5 have a calculated error value for the breaking force that is smaller than labeled (0.00002 N and 0.0008 N respectively), however the digital readout only goes to 0.001 intervals. Figure 4.16 shows the force that was required to break the fibres. Note the error bars for the breaking force are too small to be seen. Figure 4.17 shows the maximum breaking

stress,  $\sigma$ , for each fibre, which is calculated via:

$$\sigma = \frac{F}{A_{min}} \quad (4.1)$$

where  $F$  is the force required to break the fibre and  $A_{min}$  is the cross sectional area of the fibre at its thinnest point. The error associated with the breaking stress,  $\delta\sigma$ , is calculated by combining the error in the minimum area of the fibre and the error in the load cell:

$$\frac{\delta\sigma}{\sigma} = \sqrt{\left(\frac{\delta F}{F}\right)^2 + \left(\frac{\delta A_{min}}{A_{min}}\right)^2} \quad (4.2)$$

where  $\sigma$  is the breaking stress,  $F$  is the force on the load cell,  $\delta F$  is the error in the load cell,  $A_{min}$  is the minimum area of the fibre and  $\delta A_{min}$  is the error in the area.

Fibre one had the largest breaking force and stress of the five fibres with 1.599 N and  $6.05 \times 10^9$  Pa respectively. Fibre two was the weakest, only reaching 0.01 N and  $2.26 \times 10^9$  Pa for the breaking force and stress respectively. Fibres three to five shared similar values, as expected due to their similar fibre profiles, ranging between 0.334 - 0.444 N and  $3.78 - 4.07 \times 10^9$  Pa for the breaking force and stress respectively.

It is not possible to know where exactly along the fibre the breakage occurs from due to the destructive nature of the failure. The addition of a high speed camera in the future to monitor the fibre will allow the user to find the exact moment and location of the break.

It has been shown [65] that through the process of laser polishing, the fibres could potentially increase in strength, resulting in higher breaking forces and stresses required to destroy the fibres. Laser polishing is the process where the laser beam heats up the stock until its molten and moving the feed mirror at a very slow speed along the stock and back prior to the pulling of the fibre. This gets rid of surface impurities in the stock, thus potentially increasing the strength of fibres produced. This will be investigated in the future.

#### 4.2.4 Young's Modulus

The last stage of fibre characterisation that was carried out was to calculate the Young's modulus of the fibres. Young's modulus,  $Y$ , can be defined by:

$$Y = \frac{\textit{Stress}}{\textit{Strain}} \quad (4.3)$$

where the stress is defined in equation 4.1, and the strain,  $\epsilon$ , is defined as:

$$\epsilon = \frac{\Delta L}{L} \quad (4.4)$$

where  $\Delta L$  is the total extension of the fibre and  $L$  is the length of the fibre. The error for the strain of the fibre,  $\delta\epsilon$ , can be expressed as:

$$\frac{\delta\epsilon}{\epsilon} = \sqrt{\left(\frac{\delta\Delta L}{\Delta L}\right)^2 + \left(\frac{\delta L}{L}\right)^2} \quad (4.5)$$

The error associated with the Young's modulus,  $\delta Y$  can be defined by:

$$\frac{\delta Y}{Y} = \sqrt{\left(\frac{\delta\sigma}{\sigma}\right)^2 + \left(\frac{\delta\epsilon}{\epsilon}\right)^2} \quad (4.6)$$

This can only be applied if the fibre is a uniform width, but this is not the case as seen in figures 4.11 - 4.12. Therefore, to calculate the Young's modulus, the fibre must be broken down into equal segments of varying widths, as shown in figure 4.18. The lengths of the segments,  $L_n$  was determined from the separation of data points from the high magnification camera on the profiler.

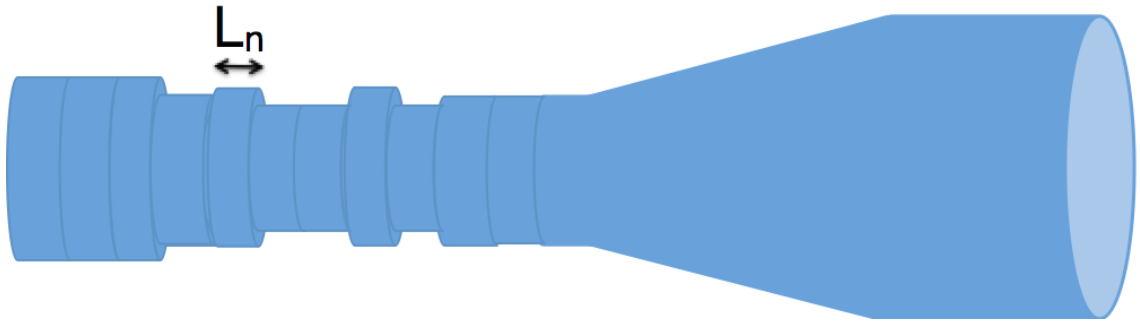


**Figure 4.18:** Illustration of a fibre and the central section broken down into lengths,  $L_n$ , with differing diameters along the fibre.

The extension of each segment,  $\Delta L_n$ , can be calculated via:

$$\Delta L_n = \frac{L_n F}{Y A_n} \quad (4.7)$$

where  $A_n$  is the area of the segment and all other symbols hold prior meanings. The total extension of the fibre can then be calculated via:

$$\sum_{i=1}^n \Delta L_n = \sum_{i=1}^n \frac{L_n F}{Y A_n} \quad (4.8)$$

When the fibre breaks in the strength tester, the extension of the fibre was measured by measuring the distance between the top plate and the bottom plate before the strength testing process began and once the fibre breaks. The Young's modulus value can be obtained when the condition is met that the calculated summation of the extension of each fibre segment is equal to that of the experimental measured fibre extension.

Figure 4.19 and table 4.9 shows the Young's modulus values obtained for all five fibres. Again, the error in the Young's modulus values are dominated by the error in the fibre diameter from the breaking stress calculation.

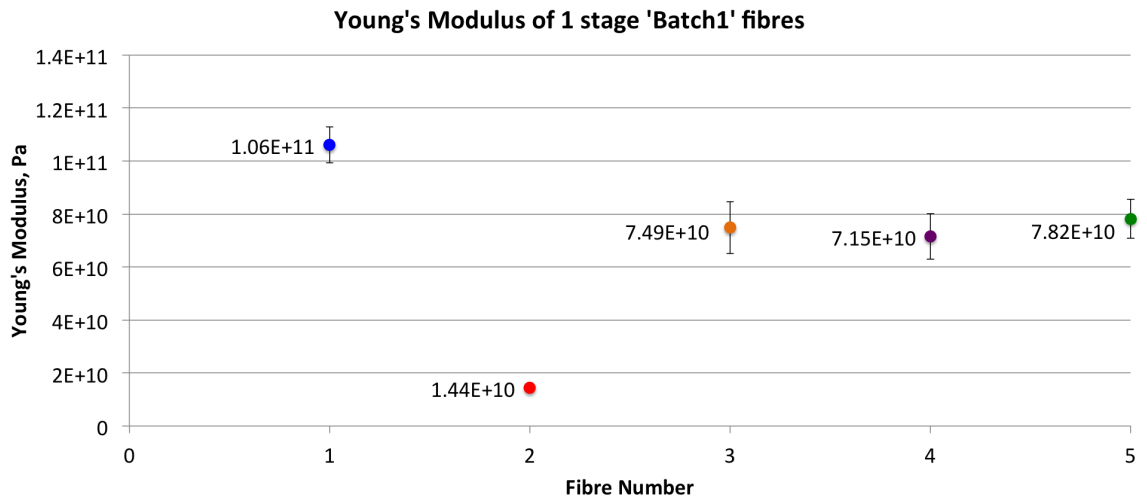


**Figure 4.19:** Young's modulus values obtained for the five fibres.

**Table 4.9:** The Young's modulus values for the five fibres.

Fibre Number	Young's modulus (Pa)
1	$106.0 \pm 6.8 (\times 10^9)$
2	$14.4 \pm 1.7 (\times 10^9)$
3	$74.9 \pm 9.8 (\times 10^9)$
4	$71.5 \pm 8.6 (\times 10^9)$
5	$78.2 \pm 7.3 (\times 10^9)$

The literature value for the Young's modulus of bulk fused silica is 73 GPa [66]. It is thought that once the diameter of the fibre goes below a certain thickness, the Young's modulus will increase as it changes from bulk characteristics to surface characteristics. Fibres one and two show values for the Young's modulus that differ greatly from this value, however fibres three - five have values that lie within the range of the literature value, when error is taken into account, with an average value of  $74.9 \pm 14.9$  GPa.

### 4.2.5 Analysis and conclusion

The aim of this section was to pull fibres that would have a central thin diameter  $< 20 \mu\text{m}$  and was achieved for all five fibres. The velocity profile used to produce the fibres created fibres that on average was 18.5 mm longer than predicted. This was due to the time intervals between each entry taking milliseconds longer than desired meaning the stage travels longer distances in each entry. The velocity values obtained from the pulling stage will require further investigation to determine whether or not the values calculated are accurate, as there is a large variation of velocity values when the velocity profile reaches  $380 \text{ mm s}^{-1}$  and beyond. This will be achieved by installing an independent position encoder that could then be compared to the internal encoder of the pulling stage to determine where the problem lies. The use of high velocities could be avoided by utilising a two stage pull down. This will be discussed in the next chapter.

The fibres were measured to have a range of breaking stress values, the largest value being  $6.05 \times 10^9 \text{ Pa}$  and the smallest being  $2.26 \times 10^8 \text{ Pa}$ . As fibre two had a breaking stress value that was much smaller than the rest of the fibres, it is thought that it may have had a possible defect. This defect could have been caused either through accidental contact or through experiencing additional heating from the laser at the end of the pull. Tokmakov et al [67] found that heating of the neck and stock at the end of a fibre can result in an increase in thermal stress of the fibre. This can result in a fibre that can be weaker than other fibres that are produced. Fibres three to five shared similar values ranging between  $3.78$  and  $4.07 \times 10^9 \text{ Pa}$ . The Young's modulus also had a wide range with fibre one's value of  $106 \text{ GPa}$  and fibre two's value of  $14.4 \text{ GPa}$ . Fibre two has both the lowest breaking stress and Young's modulus out of the five fibres produced. It is unclear whether or not these two results are correlated and will require further investigation in the future. Fibres three to five again shared similar

---

values, averaging 74.9 GPa. The strength of the fibres could potentially be increased through the technique of laser polishing the silica stock prior to the pull [65]. The effect of this will be investigated in the future.

# Chapter 5

## Fibre production - two stage pull

The previous chapter showed that when trying to command the stage to move at high velocities for short time periods, the stage can overrun by a significant distance as well as having a large difference between calculated and theoretical velocity values for the stage. This chapter is going to focus on creating fibres using a two stage pull method. This consists of firstly pulling down the initial stock to a smaller diameter stock and then pulling a fibre from the new diameter stock. This will allow thin fibres to be produced without going up to high velocities and extremely short time intervals. One of the main advantages of two stage pulls instead of one is that it will give the user the benefit of creating stock to an appropriate diameter to interface easily with the fibre attachment.

### 5.1 Batch 1 fibres

#### 5.1.1 Velocity profile

There are two separate velocity profiles that were used in two stage pulls, shown in table 5.1, and calculated distance values are shown in table 5.2. The first stage will initially pull the stock down from approximately 1900  $\mu\text{m}$  to 700  $\mu\text{m}$  over a length 7.6 mm.

The feed mirror during the first stage pull moved at a velocity of  $1 \text{ mm s}^{-1}$ . The feed mirror was moved to the middle of the new stock. The second stage then pulls a thin fibre from this stock, with the feed mirror moving at  $0.1 \text{ mm s}^{-1}$ . The determination of the feed mirror velocities was from pulling various fibres using different velocities. It was found that the faster the feed mirror moves in the second stage of the pull, the thicker the fibres were as there would be more molten stock to pull from. The fibre produced from the second stage should have a predicted length of 92.878 mm.

**Table 5.1:** The text file entered containing the velocity, acceleration and time values for the 2 stage pull.

First Stage		
Velocity ( $\text{mm s}^{-1}$ )	Acceleration ( $\text{mm s}^{-2}$ )	Time (ms)
0.1	20000	930
1	20000	100
2	20000	100
3	20000	100
4	20000	100
5	20000	100
6	20000	1000
0	20000	0
Second Stage		
Velocity ( $\text{mm s}^{-1}$ )	Acceleration ( $\text{mm s}^{-2}$ )	Time (ms)
0.1	20000	140
10	20000	100
20	20000	100
30	20000	100
40	20000	100
50	20000	100
60	20000	100
70	20000	100
160	20000	400
0	20000	0

**Table 5.2:** The theoretical data for the stage's velocity, time interval, acceleration time, accumulated time and distance travelled for the velocity profile. Note a 40 ms time delay is taken into account for the first entries of each stage.

First Stage				
Velocity (mm s <sup>-1</sup> )	Time interval (ms)	Acceleration time (ms)	Accumulated time (ms)	Distance travelled (mm)
0.1	970	0.005	970.005	0.097
1	100	0.05	1070.055	0.197
2	100	0.05	1170.105	0.397
3	100	0.05	1270.155	0.697
4	100	0.05	1370.205	1.097
5	100	0.05	1470.255	1.597
6	1000	0.05	2470.305	7.597
0	0	0.30	2470.605	7.598
Second Stage				
Velocity (mm s <sup>-1</sup> )	Time interval (ms)	Acceleration time (ms)	Accumulated time (ms)	Distance travelled (mm)
0.1	180	0.005	2650.61	7.616
10	100	0.50	2751.11	8.618
20	100	0.50	2851.61	10.620
30	100	0.50	2952.11	13.623
40	100	0.50	3052.61	17.625
50	100	0.50	3153.11	22.628
60	100	0.50	3253.61	28.630
70	100	0.50	3354.11	35.633
160	400	4.50	3758.61	99.836
0	0	8.00	3766.61	100.475

### 5.1.2 Fibre profiles and analysis

Figures 5.1 - 5.2 show the fibre profiles for the five fibres that were produced using the velocity profile in table 5.1. Table 5.3 shows an average of the five fibre pulling stage positions and table 5.4 show the minimum diameter and lengths of the fibres produced from 'Batch 1'. The errors stated in the table are calculated using the same method as discussed in the previous chapter.

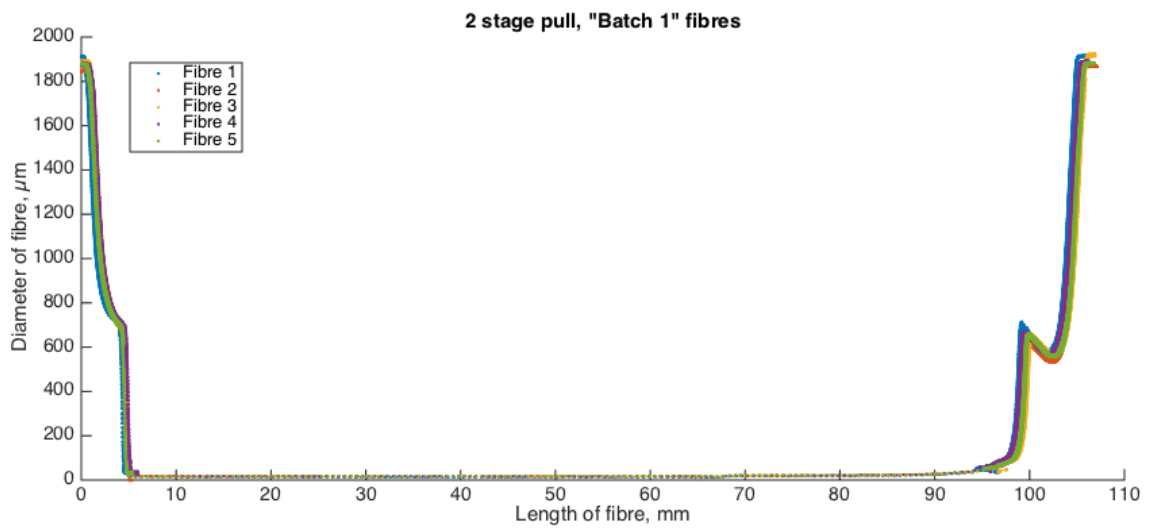


**Figure 5.1:** Profiles of the five fibres from 'Batch 1'.

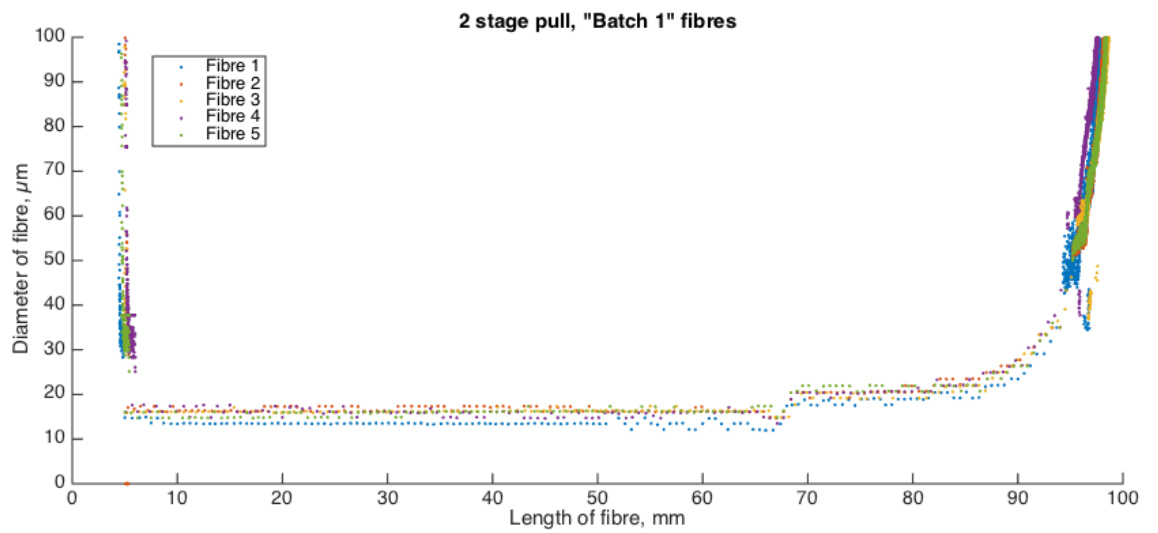


**Figure 5.2:** Close up of figure 5.1.

**Table 5.3:** The text file obtained containing the 5 run average distance travelled time interval between positions, the accumulated time values and velocities for the velocity profile.

First Stage			
Distance travelled (mm)	Time interval (ms)	Accumulated time (ms)	Velocity ( $\text{mm s}^{-1}$ )
969.2	0.100	969.2	0.097
1071.4	0.792	102.2	0.178
1175.0	2.177	103.6	0.403
1277.2	2.980	102.2	0.707
1379.8	3.969	102.6	1.115
1482.0	4.979	102.2	1.623
2484.8	5.997	1002.8	7.648
Second Stage			
Distance travelled (mm)	Time interval (ms)	Accumulated time (ms)	Velocity ( $\text{mm s}^{-1}$ )
7.664	164.8	2650.4	0.097
8.670	102.0	2752.4	9.861
10.700	103.0	2855.4	19.702
13.745	102.0	2957.4	29.859
17.829	102.4	3059.8	39.881
22.916	101.8	3161.6	49.973
29.046	102.6	3264.2	59.743
36.176	102.0	3366.2	69.907
100.897	406.4	3772.6	159.255
101.796	0	3772.6	0

**Table 5.4:** The minimum diameter values and length of the fibres from ‘Batch 1’.

Fibre Number	Fibre Minimum Diameter ( $\mu\text{m}$ )	Length of fibre (mm) $\pm 0.005$ mm
1	$11.98 \pm 0.57$	94.127
2	$14.68 \pm 0.59$	94.191
3	$14.83 \pm 0.38$	94.128
4	$13.51 \pm 0.86$	93.945
5	$14.70 \pm 0.72$	94.347

It is interesting to note from table 5.3 that the stage had an average time delay

15.2 ms less than that predicted for the first entry of the second stage. This difference in delay however only resulted in a 3  $\mu\text{m}$  difference in stage travel.

All five fibres produced were similar in minimum diameter, unlike the one stage pulls discussed in the previous chapter. The thinnest fibre had a minimum diameter of  $11.98 \pm 0.57 \mu\text{m}$  and the thickest was  $14.83 \pm 0.38 \mu\text{m}$ . All the fibres were of a similar length, with the largest difference in length of 0.402 mm between fibres four and five.

As with the previous set of fibres, this set of fibres were longer than predicted. In this case however, the fibres were only an average of 1.27 mm longer. This is much less than the 18.5 mm longer fibres that were produced previously, indicating that the lower velocities can help minimise the overrun.

There are two artefacts of interest in the fibre profiles; one in the region around 100 mm and the other between 65 - 70 mm. The first one results from the first stage of the pull down. From experience of shaping the fibres, it was determined that this would occur due to the first stage of the fibre not being long enough to flatten out. A profile of the stock width can be seen in figure 5.3. It is clear that the region from which the fibre pull in the second stage begins is between 6 mm and 10 mm.

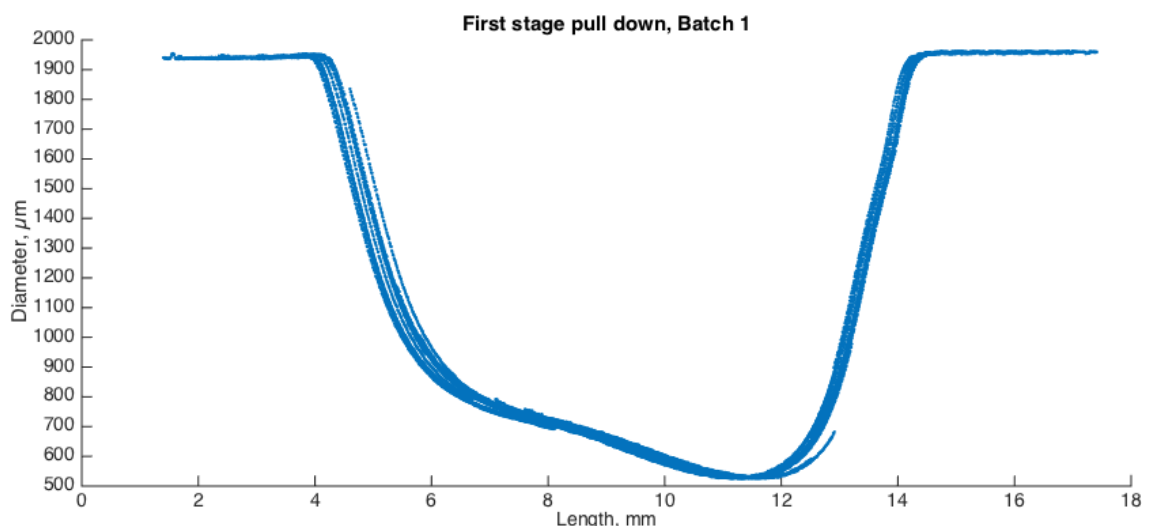


**Figure 5.3:** A profile of the silica stock after the first pull down for ‘Batch 1’.

To eliminate this dip for the future set of fibres, the first stage pull down was made

longer until the stock flattens out so that the second stage can be pulled from a flat section. The second artefact is similar to the one discussed in the previous chapter and occurs from the sharp increase in velocity occurring around 3250 ms, seen in figure 5.5.

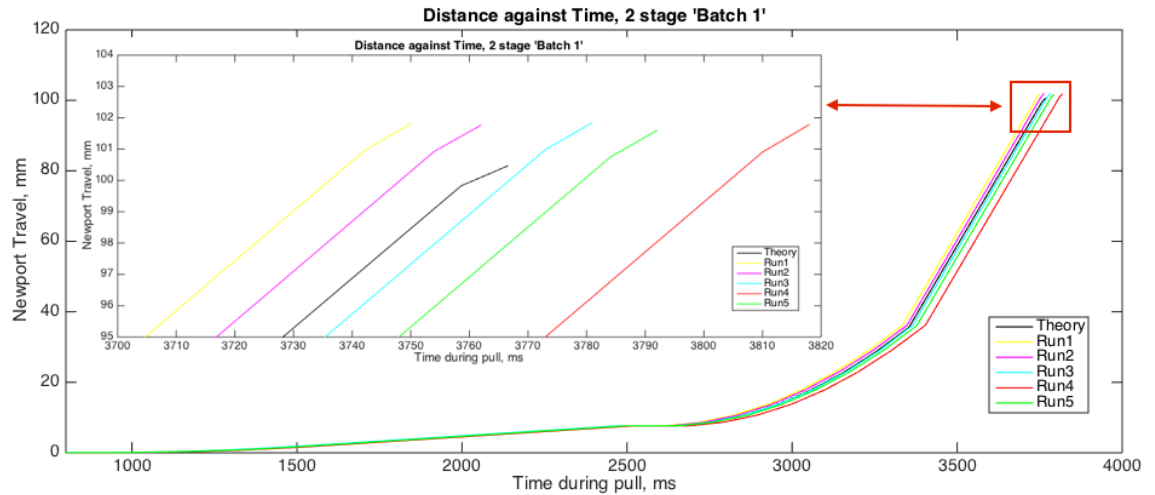


**Figure 5.4:** Distance against time for all 5 fibre pulls.

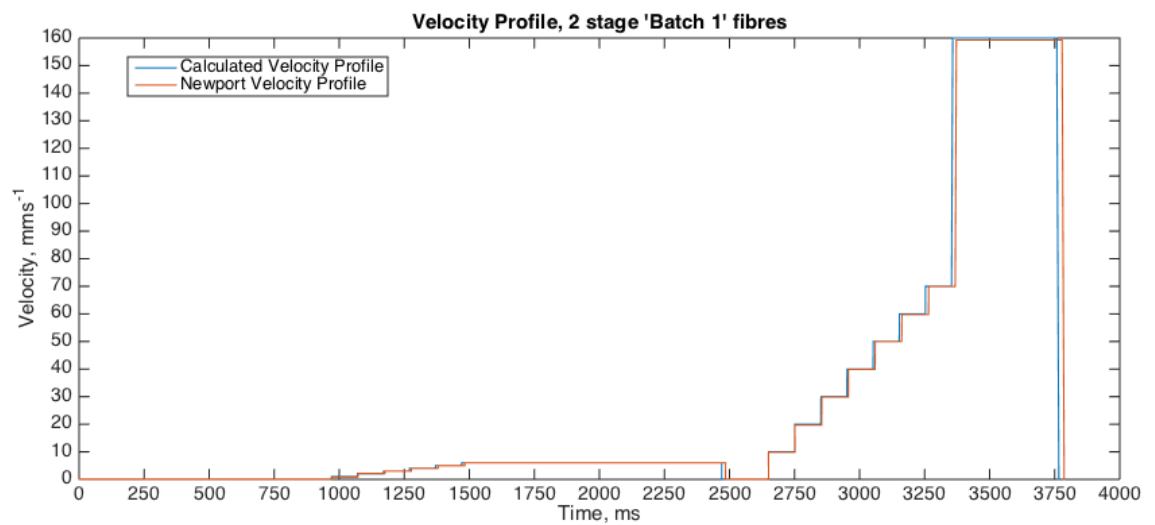


**Figure 5.5:** Velocity profile for the two stages for the 'Batch 1' fibres.

Figure 5.5 shows the velocity profile that was used to produce the fibres and figure 5.4 show the travel distance of the stage against time for all five fibre pulls, as well as the predicted values. This shows a tighter grouping than compared to the previous set of fibres, as can be seen in table 5.5 where the standard deviation and largest difference

values for each stage position is shown.

It was found that once the second stage had finished, the fibres that were produced would be slack and not held under tension. It was thought that this could occur from the sudden deceleration from  $160 \text{ mm s}^{-1}$  to a stop, resulting in recoil in the clamps. A possible solution to this was to have the final entries after the fast movement to be small non zero velocity values to help stabilise the fibre, and is explored in the next batch of fibres later in this chapter.

**Table 5.5:** The standard deviation and largest difference value of the stage position for the 5 fibres at each entry of ‘Batch 1’.

Standard Deviation	Largest difference (mm)
0.002	0.005
0.002	0.006
0.006	0.014
0.005	0.015
0.005	0.014
0.006	0.013
0.007	0.013
0.007	0.017
0.007	0.017
0.007	0.019
0.007	0.020
0.008	0.022
0.015	0.039
0.022	0.049
0.024	0.054
0.041	0.114
0.049	0.126
0.093	0.248
0.114	0.399

### 5.1.3 Strength testing and Young’s modulus

The strength testing procedure for these fibres was the same as described in the previous chapter. Figures 5.6, 5.7 and table 5.6 show the values obtained for the breaking force and breaking stress of all five fibres from ‘Batch 1’. The error bars associated with both figures 5.6 and 5.7 stem from the error in the fibre width from the profiler. It was

found that the breaking force of the five fibres averaged was  $0.582 \pm 0.001$  N and the breaking stress to be  $3.8 \pm 0.8$  GPa. The largest difference between breaking forces occurred between fibres one and two, with a difference of 0.206 N. The fibres that were produced were, again, not laser polished. However this will be added in the future and could potentially increase the strength of the fibres.

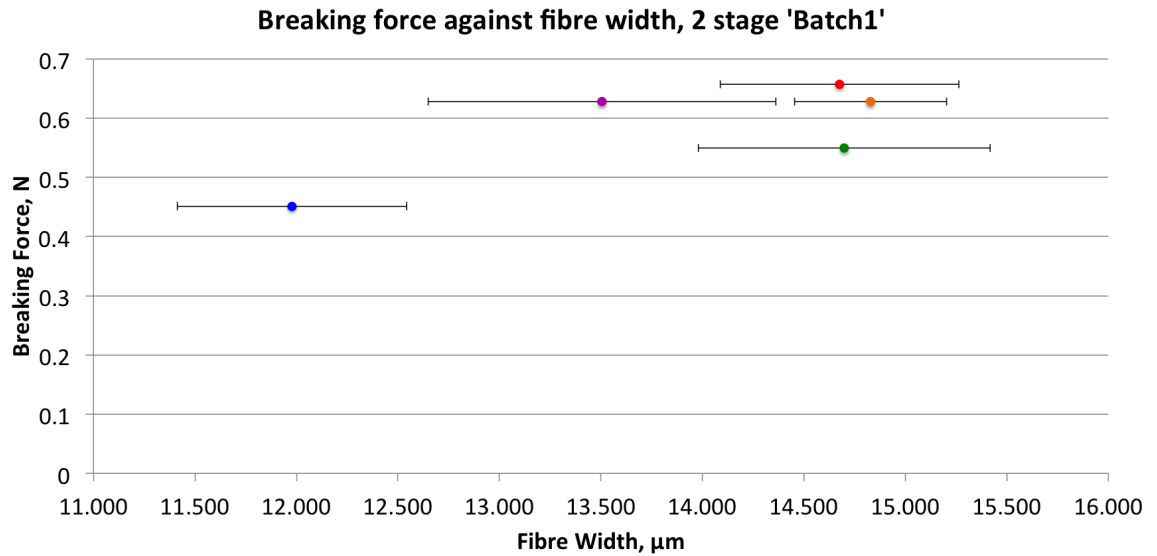


**Figure 5.6:** Breaking force values for all five fibres from 'Batch 1'.

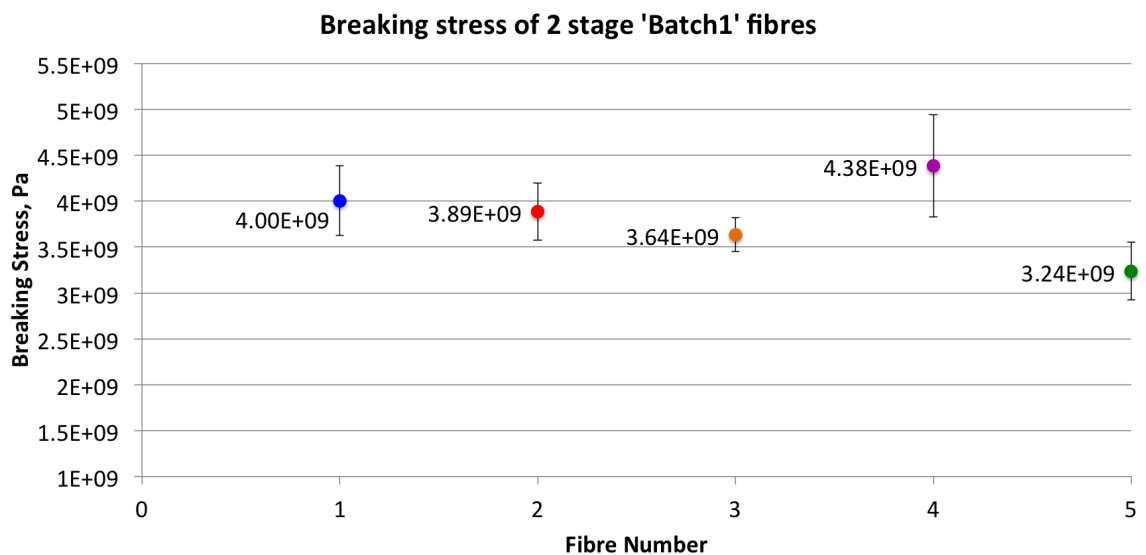


**Figure 5.7:** Breaking stress values for all five fibres from 'Batch 1'.

**Table 5.6:** The breaking force and breaking stress values for the five fibres in ‘Batch 1’.

Fibre Number	Breaking Force (N) $\pm 0.25\%$	Breaking Stress (Pa)
1	$0.451 \pm 0.001$	$4.00 \pm 0.38 (\times 10^9)$
2	$0.657 \pm 0.002$	$3.89 \pm 0.31 (\times 10^9)$
3	$0.627 \pm 0.002$	$3.64 \pm 0.18 (\times 10^9)$
4	$0.627 \pm 0.002$	$4.38 \pm 0.56 (\times 10^9)$
5	$0.549 \pm 0.001$	$3.24 \pm 0.32 (\times 10^9)$

Figure 5.8 and table 5.7 show the Young’s modulus values obtained via the method described in the previous chapter.

**Table 5.7:** The Young’s modulus values for the five fibres in batch 1.

Fibre Number	Young’s modulus (Pa)
1	$76.4 \pm 7.2 (\times 10^9)$
2	$75.4 \pm 6.1 (\times 10^9)$
3	$74.3 \pm 3.8 (\times 10^9)$
4	$75.6 \pm 9.6 (\times 10^9)$
5	$65.1 \pm 6.5 (\times 10^9)$

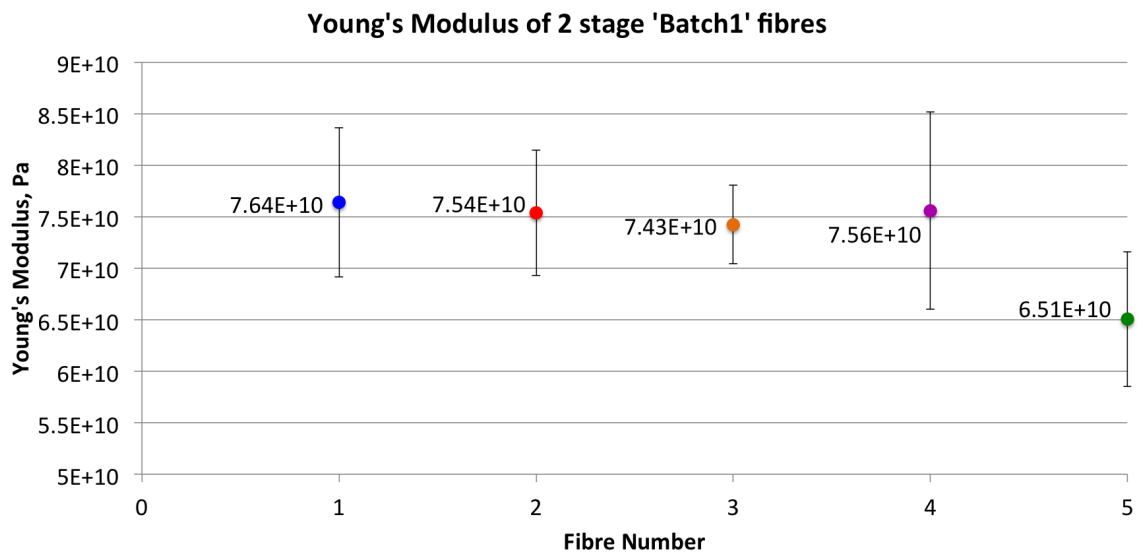


**Figure 5.8:** Young’s modulus values for all fibres from ‘Batch 1’.

The Young's modulus values obtained had a five fibre average of  $73.4 \pm 15.5$  GPa, which is in good agreement with the literature value of bulk fused silica.

#### 5.1.4 Analysis

The aim of this section was to produce thin fibres with a two stage pull and to compare the stage positions obtained with the previous set of stage positions from the last set of fibres. The production of thin fibres was successful with a two stage pull, with the fibres ranging in minimum diameter from 11.9 - 14.8  $\mu\text{m}$ . It turned out however that the first pull down was not long enough as the stock did not even out in width over a long length, but in fact was tapering down. This can be fixed by making the first stage pull longer.

The fibres produced were slightly longer than expected, averaging a value of 1.27 mm longer than the theoretical value. This was a vast improvement over the previous set of fibres where the fibres were 18.5 mm longer than predicted, indicating that the use of lower velocities can help decrease the over run experienced. The fibres after production were found to be a bit slack. It is thought that this could be solved by making the final velocities after the fast movement a small non zero value to help stabilise the fibre before bringing the stage to a halt.

The positions of the stage during the pull were found to be repeatably consistent with each other, as shown by the standard deviation values in table 5.5. This was a great improvement from the previous set of fibres, indicating that the user will have greater accuracy and control over the fibres with lower velocities. This is a major benefit of a two stage pull instead of a one stage pull.

The breaking force and stress of the fibres had an average value of  $0.582 \pm 0.001$  N and  $3.8 \pm 0.8$  GPa respectively. This gives the fibres an average Young's modulus value of  $73.4 \pm 15.5$  GPa with is in good agreement with the literature value of bulk fused silica. It is thought that the Young's modulus may increase once below a certain

thickness as it changes from bulk fused silica characteristics to surface characteristics. Though at this point this has not been experience, it is planned to create thinner fibres to explore this parameter space.

## 5.2 Batch 2 fibres

After the success of producing thin fibres from a two stage pull, there were immediate improvements that could be made. These improvements were aimed to be achieved in the second batch of fibres produced. The main improvement that had to be met was to make the first stage pull down longer to give a longer length of stock to pull from that was of a constant width. This would allow the fibre to be extracted via laser cutting with long enough ends to weld on to. Another improvement was to remove the issue of the fibre slopping at the end of the second stage pull. It was thought this could be eliminated by introducing low velocity entries after the  $160 \text{ mm s}^{-1}$  before bringing the stage to a stop. The stock in this batch of fibres were also laser polished to see if any difference is made to the strength of the fibres produced. A 7 mm region of the silica stock was laser polished over a time of 350 seconds.

### 5.2.1 Velocity profile

The velocity profile used is shown in table 5.8 and the theoretical distance values shown in table 5.9.

**Table 5.8:** The text file entered containing the velocity, acceleration and time values for the 2 stage pull, with the new entries in bold.

First Stage		
Velocity (mm s <sup>-1</sup> )	Acceleration (mm s <sup>-2</sup> )	Time (ms)
0.1	20000	930
1	20000	100
2	20000	100
3	20000	100
4	20000	100
5	20000	100
6	20000	4000
0	20000	0
Second Stage		
Velocity (mm s <sup>-1</sup> )	Acceleration (mm s <sup>-2</sup> )	Time (ms)
0.1	20000	140
10	20000	100
20	20000	100
30	20000	100
40	20000	100
50	20000	100
60	20000	100
70	20000	100
160	20000	400
<b>10</b>	<b>20000</b>	<b>100</b>
<b>5</b>	<b>20000</b>	<b>300</b>
0	20000	0

**Table 5.9:** The theoretical data for the stage’s velocity, time interval, acceleration time, accumulated time and distance travelled for the velocity profile for ‘Batch 2’. Note a 40 ms time delay is taken into account for the first entries of each stage.

First Stage				
Velocity (mm s <sup>-1</sup> )	Time interval (ms)	Acceleration time (ms)	Accumulated time (ms)	Distance travelled (mm)
0.1	960	0.005	960.005	0.096
1	100	0.05	1060.055	0.196
2	100	0.05	1160.105	0.396
3	100	0.05	1260.155	0.696
4	100	0.05	1360.205	1.096
5	100	0.05	1460.255	1.596
6	4000	0.05	5460.305	25.596
0	0	0.30	5460.605	25.597
Second Stage				
Velocity (mm s <sup>-1</sup> )	Time interval (ms)	Acceleration time (ms)	Accumulated time (ms)	Distance travelled (mm)
0.1	180	0.005	5640.61	25.613
10	100	0.50	5741.11	26.615
20	100	0.50	5841.61	28.618
30	100	0.50	5942.11	31.620
40	100	0.50	6042.61	35.623
50	100	0.50	6143.11	40.625
60	100	0.50	6243.61	46.628
70	100	0.50	6344.11	53.630
160	400	4.50	6748.61	117.833
10	100	7.50	6856.11	119.395
5	300	0.25	7156.36	120.896
0	0	0.25	7156.61	120.896

It was predicted that due to the pulling time extension in stage one, the stock diameter used for the stage two pull will be more uniform than that of ‘Batch 1’. It would also result in a thinner stock as the extended pull means that the silica would no longer be tapered, giving the possibility of producing thinner fibres. Two additional velocity commands, 10 mm s<sup>-1</sup> and 5 mm s<sup>-1</sup>, were inserted after the 160 mm s<sup>-1</sup> entry

in the second stage. This was hoped to remove the issue of the fibre being slack after the pull has been completed by stabilising the fibre before coming to a stop. The feed mirror velocity during the two stages remains the same as previous. It was predicted that the fibre would have a length of 95.3 mm.

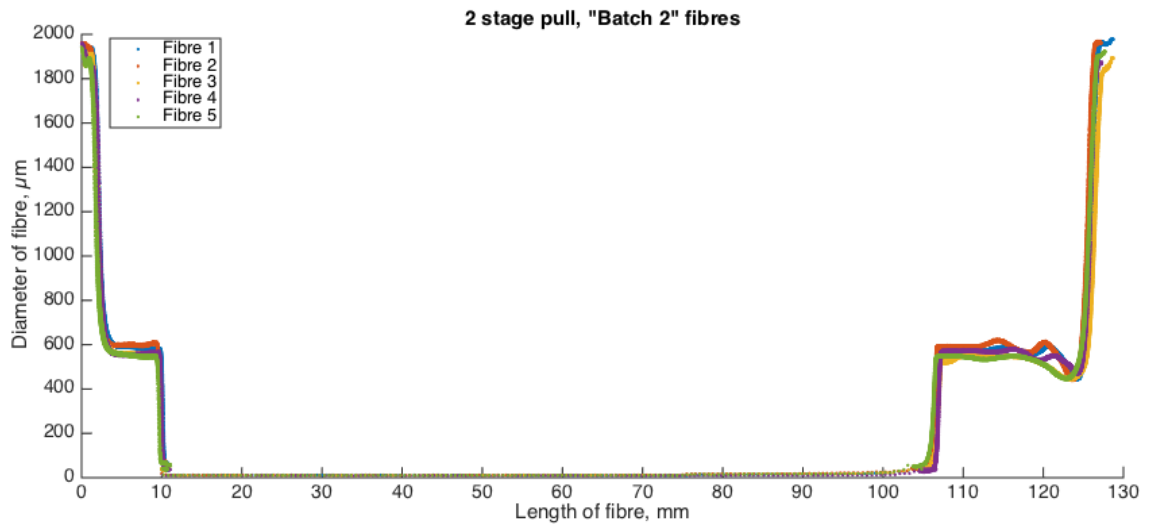
### 5.2.2 Fibre profiles and analysis

Figures 5.9 - 5.10 show the profile of five fibres that were produced from ‘Batch 2’. The minimum diameter of the fibres are given in table 5.10. The fibres produced all had a minimum diameter less than that in ‘Batch 1’. This can be attributed to the fact that the stock after stage one was thinner than that from ‘Batch 1’. There is a slight variation in the diameter of the stock from the first stage pull, ranging between 550  $\mu\text{m}$  to 600  $\mu\text{m}$ . This was due to the process of laser polishing which altered the diameter of the original stock. The laser would drift in power resulting in some areas of the stock vaporising, thus decreasing the diameter of the stock. This decrease in stock diameter was unexpected and will be solved in the future by installing a laser power stabiliser system.

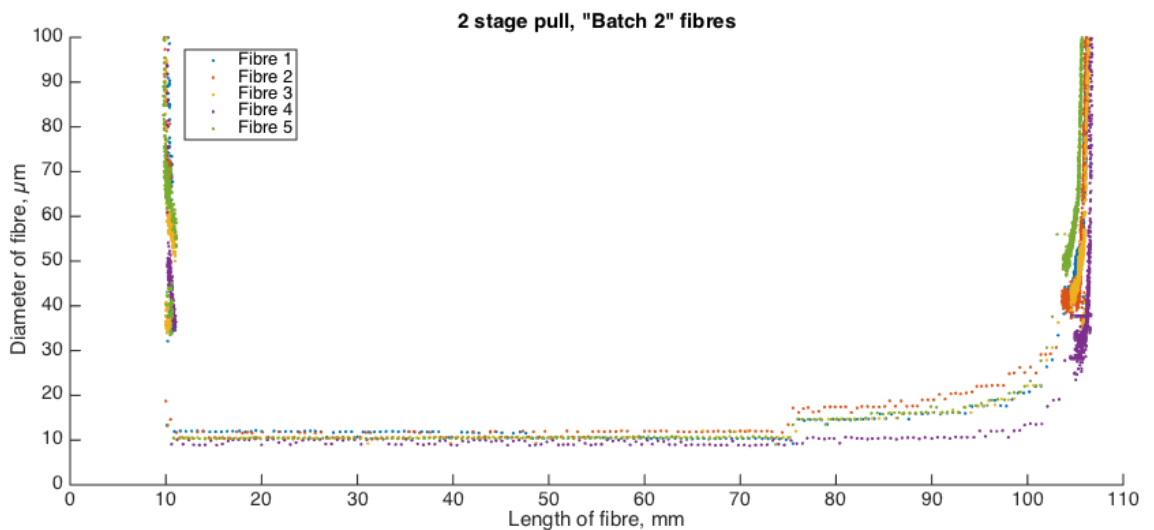
The fibres produced in this batch were thinner than that in ‘Batch 1’. The fibres produced ranged in minimum diameter between  $8.72 \pm 0.61 \mu\text{m}$  and  $10.34 \pm 0.66$ . The artefact that appears in figure 5.10 is the same artefact that shows up in figure 5.2.

**Table 5.10:** The minimum diameter values and length of the fibres from ‘Batch 2’.

Fibre Number	Fibre Minimum Diameter ( $\mu\text{m}$ )	Length of fibre (mm) $\pm 0.005$ mm
1	$9.25 \pm 0.76$	96.528
2	$10.34 \pm 0.66$	96.554
3	$9.25 \pm 0.35$	96.579
4	$8.72 \pm 0.61$	96.625
5	$9.05 \pm 0.21$	96.624



**Figure 5.9:** Profile of the fibres produced from 'Batch 2'.



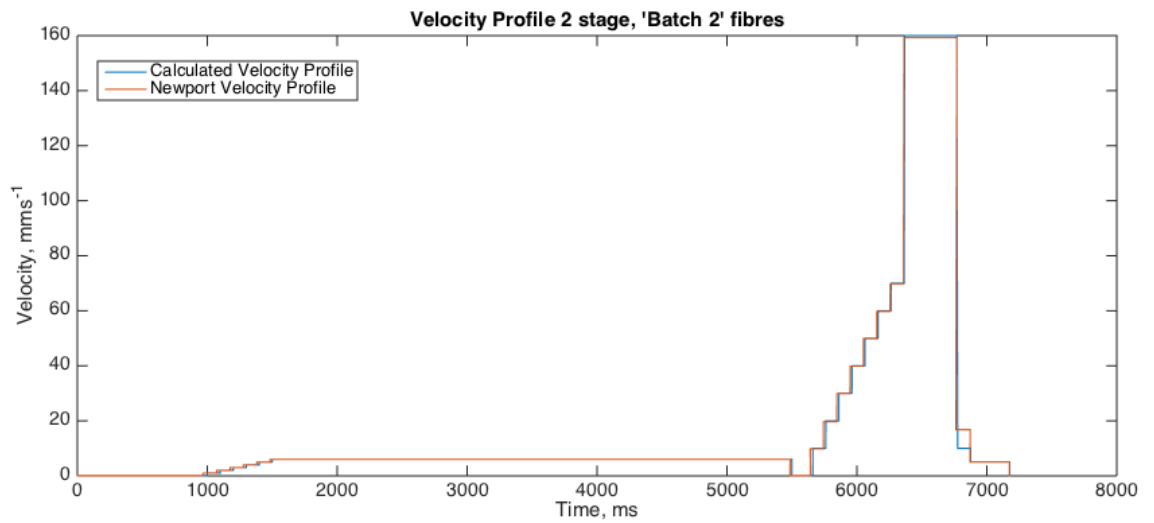
**Figure 5.10:** Close up of figure 5.9.

Table 5.11 show the five run average for the stage positions during the two stage pull and figure 5.11 shows the velocity profile that was used to produce the fibres of 'Batch 2'. The first entry for the second stage was again shorter than predicted, with a difference of 24 ms resulting in an average difference of 2  $\mu\text{m}$  with the predicted travel for this entry. It is noticeable that the first velocity entry after  $160 \text{ mm s}^{-1}$  had an average value of  $16.8 \text{ mm s}^{-1}$  when the text file entry was  $10 \text{ mm s}^{-1}$ . The reason for this was unknown, as the deceleration time was an average of 7.2 ms meaning this

the stage still decelerating can be ruled out. This will require further investigation as previous velocity profiles that involved similar sharp drops in velocity did not show this behaviour. The fibres were 1.35 mm longer than the predicted value. This is also 0.079 mm greater overrun than ‘Batch 1’ fibres, but again a significant improvement from the one stage pulls. Table 5.12 show the standard deviation of each position for the 5 runs and the largest difference between the positions. As with ‘Batch 1’, the position values at each velocity change is significantly closer together for the five runs than the one stage pulls.

**Table 5.11:** The text file obtained containing the 5 run average distance travelled, time interval between positions, the accumulated time and velocity values for the velocity profile.

First Stage			
Distance travelled (mm)	Time interval (ms)	Accumulated time (ms)	Velocity ( $\text{mm s}^{-1}$ )
0.096	966.2	966.2	0.100
0.200	107.0	1073.2	0.976
0.404	102.2	1175.4	1.994
0.709	102.4	1277.8	2.979
1.117	102.8	1380.6	3.972
1.627	102.2	1482.8	4.992
25.638	4002.4	5485.2	5.999
25.648	0	5485	0
Second Stage			
Distance travelled (mm)	Time interval (ms)	Accumulated time (ms)	Velocity ( $\text{mm s}^{-1}$ )
25.663	156.0	5641.2	0.098
26.669	102.2	5743.4	9.838
28.695	102.8	5846.2	19.710
31.746	102.0	5948.2	29.918
35.821	102.2	6050.4	39.873
40.908	102.0	6152.4	49.868
47.026	102.4	6254.8	59.751
54.162	102.2	6357.0	69.819
118.873	406.2	6763.2	159.309
120.714	109.6	6872.8	16.796
122.238	302.2	7175.0	5.042
122.245	0	7175.0	0



**Figure 5.11:** The velocity profile used to produce the fibres in ‘Batch 2’.

**Table 5.12:** The standard deviation and largest difference value of the stage position for the 5 fibres at each entry of ‘Batch 2’.

Standard Deviation	Largest difference (mm)
0.001	0.003
0.007	0.017
0.007	0.018
0.007	0.018
0.008	0.018
0.009	0.022
0.012	0.028
0.012	0.029
0.012	0.030
0.013	0.032
0.013	0.030
0.018	0.048
0.025	0.060
0.027	0.065
0.021	0.054
0.040	0.105
0.046	0.124
0.048	0.113
0.047	0.109
0.047	0.108

### 5.2.3 Strength testing and Young's modulus

The strength testing procedure that was carried out for these fibres was the same as described in the previous chapter. Figures 5.12, 5.13 and table 5.13 show the values for the breaking force and breaking stresses of all five fibres. The five fibres managed to average a breaking force and stress of 0.265 N and 3.846 GPa respectively. This is a similar average breaking stress value as that found in 'batch 1'. Since the average minimum fibre diameter values between 'batch 1' and 'batch 2' differed due to the laser polishing process, it is not a fair comparison to compare the breaking stress values between the two sets of fibres to come to a meaningful conclusion with regards to how much of an improvement the introduction of laser polishing brought. Further investigation will be needed to confirm this and will be carried out in the future.

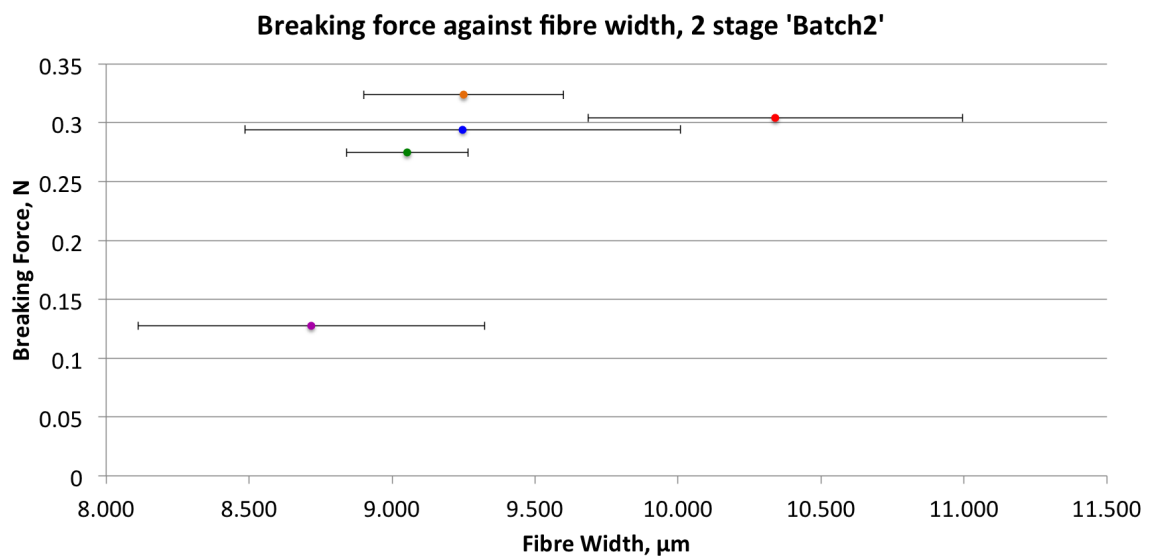


**Figure 5.12:** The force required to break each fibre in 'Batch 2'.

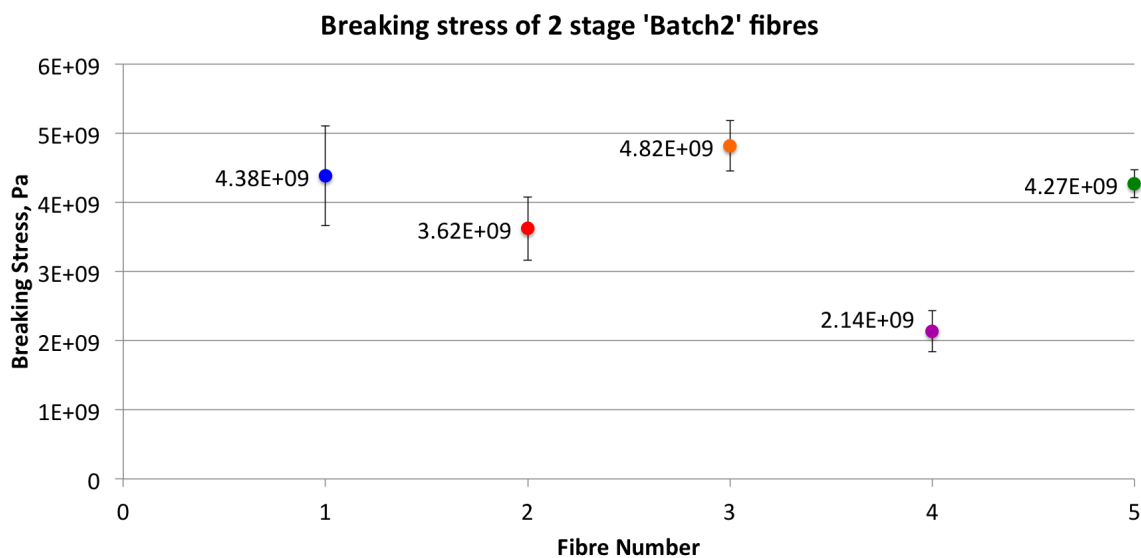


**Figure 5.13:** The breaking stress of all the fibres in ‘Batch 2’.

**Table 5.13:** The breaking force and breaking stress values for the five fibres in ‘Batch 2’.

Fibre Number	Breaking Force (N) $\pm 0.25\%$	Breaking Stress (Pa)
1	$0.2940 \pm 0.0007$	$4.38 \pm 0.72 (\times 10^9)$
2	$0.3040 \pm 0.0007$	$3.62 \pm 0.46 (\times 10^9)$
3	$0.3240 \pm 0.0008$	$4.82 \pm 0.36 (\times 10^9)$
4	$0.1280 \pm 0.0003$	$2.14 \pm 0.30 (\times 10^9)$
5	$0.2750 \pm 0.0007$	$4.27 \pm 0.20 (\times 10^9)$

Figure 5.14 and table 5.14 shows the Young’s modulus that was calculated for each of the fibres from ‘Batch 2’. The Young’s modulus was calculated the same way as previously with the same error in the value as explained previously. The Young’s modulus for four of the five fibres was larger than that of the literature value of bulk fused silica, ranging between 75.1 GPa and 87.0 GPa. Fibre four which was the exception, with a Young’s modulus of 54.0 GPa, will be discussed in detail in section 5.2.4.

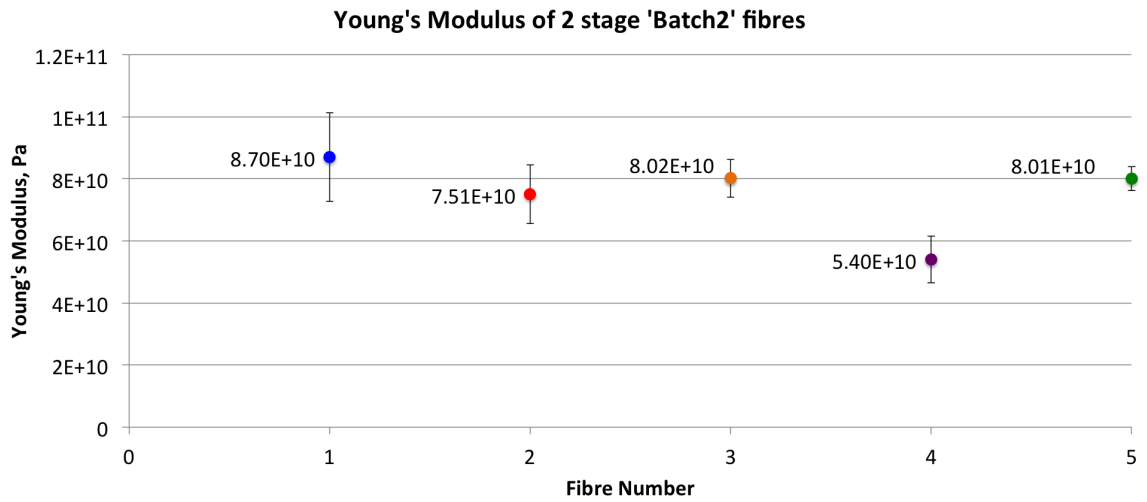


**Figure 5.14:** Young's modulus values for all fibres from 'Batch 2'.

**Table 5.14:** The Young's modulus values for the five fibres in 'Batch 2'.

Fibre Number	Young's modulus (Pa)
1	$87.0 \pm 14.3 (\times 10^9)$
2	$75.1 \pm 9.5 (\times 10^9)$
3	$80.2 \pm 6.1 (\times 10^9)$
4	$54.0 \pm 7.5 (\times 10^9)$
5	$80.1 \pm 3.9 (\times 10^9)$

### 5.2.4 Analysis

The aim of this section was to produce thin fibres from a two stage pull, from a thinner and longer stock that was produced from the first stage. This was achieved by increasing the length of the time for the final velocity entry for the first stage pull down. This allowed the stock to reach a constant diameter from which the second stage of the pull can be commenced.

The fibres that were produced ranged in diameters between  $8.72 \pm 0.61$  and  $10.34 \pm 0.66 \mu\text{m}$ , which was approximately  $3 \mu\text{m}$  less than the thinnest fibre that was pulled from 'Batch 1', though the second stage velocities were the same for both batches. This was due to the fact that the stock that was produced from the first stage was

thinner than that of the previous batch, allowing the thinner fibres to be produced. As with all the other fibres, the lengths were longer than predicted. Here, the fibres were 1.35 mm longer than predicted, though this is still a vast improvement from the one stage fibres that were 18.5 mm longer than predicted. It is seen that this overrun can be minimised via the use of lower velocities which can produce thin fibres if the stock pulled from the first stage is sufficiently small enough.

The addition of two low velocity entries at the end of stage two solved the issue of fibre slackness at the end of the pull. The fibres produced were held under tension in the clamps with no noticeable movement occurring during the extraction process.

Fibre ‘four’ stood out in this batch due to it having the lowest breaking stress and Young’s modulus values out of the five fibres. The reason for this correlation is unclear and can only be speculated at this point until further investigation is carried out. For this fibre, there was an interesting observation noted during the strength testing process. The rate at which the force applied to the load cell increased at a much lower rate than all the other four fibres tested. It is possible that there may have been a defect in the neck of the fibre that could have been caused from a timing issue with the laser shut off, as illustrated in figure 5.15. This occurs when the pulling stage is stationary once the pull has been completed, but the laser is still on heating the one section of the fibre. This deformation at the end of the pull was common when the laser was controlled manually instead of through the LabVIEW programme. As the strength tester was extending the fibre, it is possible that this region started to straighten out, resulting in the total extension of the fibre falling in the similar range value as the rest of the fibres, shown in table 5.15, but breaking at a much lower breaking value as this deformation would compromise the strength of the fibre. This could be an explanation for the low breaking force and low Young’s modulus value.

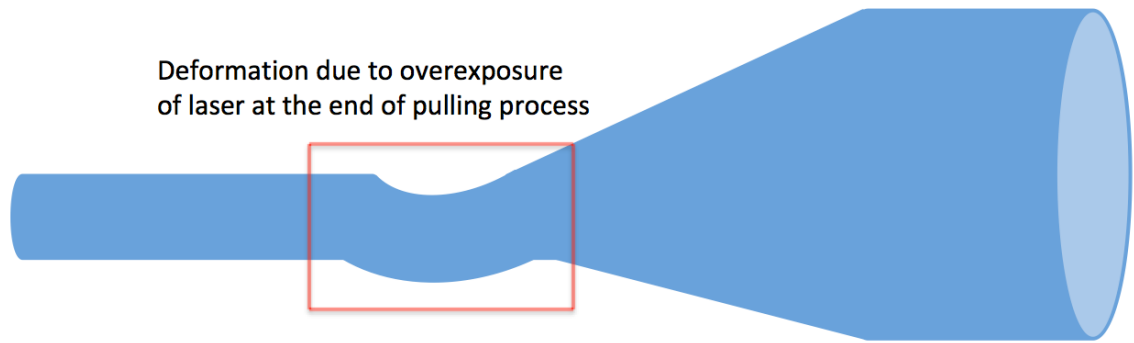


**Figure 5.15:** An illustration of a deformation that can occur at the end of the pulling process due to overexposure of the laser when the pulling stage is stationary.

**Table 5.15:** The total measured extension values for the five fibres in ‘Batch 2’ at point of fibre breakage.

Fibre Number	Total Extension (mm)
1	$2.72 \pm 0.01$
2	$2.95 \pm 0.01$
3	$3.53 \pm 0.01$
4	$2.80 \pm 0.01$
5	$2.94 \pm 0.01$

The average breaking stress of the fibres was found to be  $3.9 \pm 1.0$  GPa, though this was brought down slightly due to one of the fibres, fibre ‘four’, having a breaking stress significantly lower than the other four. If this fibre was ignored, the average breaking stress of the four fibres would be  $4.3 \pm 1.0$  GPa. This would be an improvement from the previous batch of fibres and could possibly be attributed to the fact that the silica stock was laser polished prior to any pulls commencing. However, further investigation will need to be carried out between fibres of similar diameter and with a lower diameter error to determine how much of an improvement is made to make a meaningful comparison between unpolished and polished fibres. There is also potential for this breaking stress to increase by increasing the polishing time of the silica stock, and will also be investigated in the future.

---

The Young's modulus of the five fibres was found to have a five fibre average value of  $75.3 \pm 20.0$  GPa. If fibre 'four' is ignored again, the average Young's modulus value would be  $80.6 \pm 18.3$  GPa. It is possible that the Young's modulus of fused silica may increase once below a certain diameter as the properties change from bulk to surface characteristics. Due to the large error in the Young's modulus value, further investigation must be carried out to see if the Young's modulus value does increase for fibres with a diameter of  $\leq 10$   $\mu\text{m}$ , as found with the fibres tested in this section, by profiling the fibres with a profiler with a greater magnification than used in this thesis.

# Chapter 6

## Conclusion

This thesis was aimed at building and developing the new small diameter silica fibre pulling machine based on the concept of the current aLIGO silica fibre pulling machine, with the goal of producing fibres repeatably that could have a diameter less than 20  $\mu\text{m}$ . This was achieved as all the fibres produced in this thesis had a minimum diameters that was less than 20  $\mu\text{m}$ .

Fibres that were pulled via a one stage velocity profile had a minimum diameter ranging between 7.4 and  $18.3 \pm 0.4$  and  $0.6 \mu\text{m}$  respectively. The breaking stress values obtained from these fibres ranged between  $2.26 \pm 0.26 \times 10^8$  Pa and  $6.05 \pm 0.39 \times 10^9$  Pa. The Young's modulus was then calculated to range between  $14.4 \pm 1.7$  GPa and  $106.0 \pm 6.8$  GPa. The fibres produced were also 18.5 mm longer than predicted. This large range in values was likely due to the stage traveling at velocities that differed from the programmed velocity profile as high velocities and extremely short time scales were chosen to push the stage to the limits of its capabilities. The main error in all the values stems from the error in the fibre width from the fibre profiler. This profiler was not designed to profile fibres this thin, and will be upgraded in the near future to allow this error to be reduced.

Fibres that were pulled via a two stage velocity profile showed more promise. One

---

of the main benefits of a two stage pull was the freedom of the user to create stock after the first stage to a diameter of their choosing to suit what the fibre would be welded to. As the fibres were being pulled from a smaller stock, it meant that the stage could travel at lower velocities. In this case, the maximum velocity experienced in the two stage method was  $160 \text{ mm s}^{-1}$ , where as in the one stage pull, the maximum velocity was  $490 \text{ mm s}^{-1}$ . This meant that the stage travel could be more predictable, increasing the repeatability of the fibres produced.

The first batch of fibres pulled from a two stage method had a minimum diameter ranging between  $11.98$  and  $14.83 \pm 0.57$  and  $0.38 \mu\text{m}$  respectively. The breaking stress values obtained from these fibres ranged between  $3.24$  and  $4.38 \pm 0.32$  and  $0.56 \text{ GPa}$  respectively. The Young's modulus was then calculated to range between  $65.1$  and  $76.4 \pm 6.5$  and  $7.2 \text{ GPa}$  respectively. The average values for the breaking stress and Young's modulus was  $3.8 \pm 0.8 \text{ GPa}$  and  $73.4 \pm 15.5 \text{ GPa}$  respectively. This Young's modulus value is in good agreement with the literature value of bulk fused silica. The fibres in this case however were only  $1.27 \text{ mm}$  longer than predicted. This is  $17.23 \text{ mm}$  less than experience with the one stage pulled fibres.

The second batch of fibres pulled from a two stage method had a minimum diameter ranging between  $8.72$  and  $10.34 \pm 0.61$  and  $0.66 \mu\text{m}$  respectively. These were the thinnest fibres that were produced in this thesis. The breaking stress values obtained for these fibres ranged between  $2.14$  and  $4.82 \pm 0.30$  and  $0.36 \text{ GPa}$  respectively. The Young's modulus calculated for these fibres ranged between  $54.0$  and  $87.0 \pm 7.5$  and  $14.3 \text{ GPa}$  respectively. As with the first batch, the fibres produced were only  $1.35 \text{ mm}$  longer than predicted. The large range in values in this batch can be attributed to one fibre that broke at a breaking stress that was much lower than the rest of the fibres in this batch, possibly due to accidental damage or defect to the fibre during production. If that fibre was ignored, the average values for the breaking stress and Young's modulus would be  $4.3 \pm 1.0 \text{ GPa}$  and  $80.6 \pm 18.3 \text{ GPa}$  respectively.

There is still a lot of work to be completed to fully characterise the thin fibre's properties, such as the mechanical loss and thermoelastic loss associated with the fibres. Larger batches of fibres could be investigated to extend the work carried out in this thesis to observe a greater range of breaking stress and Young's modulus values, as well as comparing the profiles that are obtained from the fibres. There are also improvements that can be made to the pulling machine to aid the stability and long term alignment of the components on the bench. Future work to be carried out in the near future will include:

- Modifications to the components on the bench to aid the long term stability of the pulling machine.
- A thermal imaging camera will be added to observe the distribution of the laser beam to the stock to aid in alignment of the beam.
- The installation of a higher magnification camera on the profiler to allow thin fibres to be profiled with greater accuracy.
- The installation of a high speed camera for the strength tester to monitor the thin fibres to find out where the thin fibres break.
- A position encoder on the strength tester will monitor the extension of the fibre without physically having to measure the extension, resulting in more accurate readings.

# Bibliography

- [1] A. Einstein, “Näherungsweise integration der feldgleichungen der gravitation,” *Sitzungsberichte der Königlich Preussischen Akademie der Wissenschaften Berlin*, pp. 688–696, 1916.
- [2] A. Einstein, “Zur elektrodynamik bewegter körper,” *Annalen de Physik*, vol. 17, pp. 891–921, 1905.
- [3] I. Newton, *Philosophiae naturalis principia mathematica*. Londini, 1687.
- [4] B. J. Setterfield, “Zero point energy and relativity,” in *Proceedings of the 19th Natural Philosophy Alliance Conference*, vol. 9, p. 528, 2012.
- [5] B. F. Schutz and F. Ricci, “Gravitational waves, sources and detectors.” <http://arxiv.org/abs/1005.4735>, May 2000.
- [6] M. Pitkin, S. Reid, S. Rowan, and J. Hough, “Gravitational wave detection by interferometry (ground and space),” *Living Reviews in Relativity*, vol. 14, no. 5, pp. 8–23, 2011.
- [7] A. Einstein, “Über gravitationswellen,” *Sitzungsberichte, Preussische Akademie der Wissenschaften*, pp. 154–167, 1918.
- [8] B. S. Sathyaprakash and B. F. Schutz, “Physics, astrophysics and cosmology with gravitational waves,” *Living Reviews in Relativity*, vol. 12, no. 2, pp. 18–19, 2009.

- 
- [9] G. M. Harry, “Advanced ligo: the next generation of gravitational wave detectors,” *Classical and Quantum Gravity*, vol. 27, pp. 1–12, 2010.
- [10] B. W. Carroll and D. A. Ostlie, *An Introduction to Modern Astrophysics*. Pearson Education inc., second ed., 2007.
- [11] B. F. Schutz, “Gravitational-wave sources,” *Classical and Quantum Gravity*, vol. 13, pp. A228–A229, 1996.
- [12] R. A. Hulse and J. H. Taylor, “Discovery of a pulsar in a binary system,” *The Astrophysical Journal*, vol. 195, pp. L51–L53, January 1975.
- [13] J. H. Taylor, L. A. Fowler, and P. M. McCulloch, “Measurements of general relativistic effects in the binary pulsar psr1913+16,” *Nature*, vol. 277, pp. 437–440, February 1979.
- [14] J. M. Weisberg and J. H. Taylor, “Relativistic binary pulsar b1913+16: Thirty years of observations and analysis,” *ASP Conference Series*, vol. 328, p. 4, 2005.
- [15] B. F. Schutz, “Determining the hubble constant from gravitational wave observations,” *Nature*, vol. 323, pp. 310–311, 1986.
- [16] E. W. Kolb and R. Peccei, eds., *Proceedings of the Snowmass 95 Summer Study on Particle and Nuclear Astrophysics and cosmology*, World Scientific Singapore, 1995.
- [17] B. Allen and J. D. Romano, “Detecting a stochastic background of gravitational radiation: Signal processing strategies and sensitivities,” *Physical Review D*, vol. 59, pp. 102001–5, 1999.
- [18] J. Weber, “Detection and generation of gravitational waves,” *Physical Review*, vol. 117, no. 1, p. 309, 1960.

- [19] J. Weber, “Gravitational wave detector events,” *Physical Review Letters*, vol. 20, pp. 1307–1308, June 1968.
- [20] J. Weber, “Evidence for discovery of gravitational radiation,” *Physical Review Letters*, vol. 22, pp. 1320–1324, June 1969.
- [21] J. A. Tyson and R. P. Giffard, “Gravitational wave astronomy,” *Annual review of astronomy and astrophysics*, vol. 16, pp. 521–554, 1978.
- [22] M. Cerdonio, M. Bonaldi, D. Carlesso, *et al.*, “The ultracryogenic gravitational-wave detector auriga,” *Classical and Quantum Gravity*, vol. 14, no. 6, pp. 1491–1494, 1997.
- [23] A. Abramovici, W. E. Althouse, and R. W. P. D. and others, “Ligo: The laser interferometer gravitational-wave observatory,” *Science*, vol. 256, pp. 325–333, April 1992.
- [24] T. Accadia, F. Acernese, M. Alshourbagy, *et al.*, “Virgo: a laser interferometer to detect gravitational waves,” *Journal of Instrumentation*, vol. 7, no. 3, p. 03012, 2012.
- [25] B. Willke, P. Aufmuth, C. Aulbert, *et al.*, “The geo 600 gravitational wave detector,” *Classical and Quantum Gravity*, vol. 19, pp. 1377–1387, 2002.
- [26] F. Acernese, M. Agathos, K. Agatsuma, *et al.*, “Advanced virgo: a 2nd generation interferometric gravitational wave detector,” *Classical and Quantum Gravity*, vol. 32, p. 024001, 2015.
- [27] A. Khalaidovski, H. Vahlbruch, N. Lastzka, *et al.*, “Status of the geo 600 squeezed-light laser,” *Journal of Physics: Conference Series*, vol. 363, p. 012013, 2011.
- [28] P. Amaro-Seoane, S. Aoudia, S. Babak, *et al.*, “Low-frequency gravitational-wave science with elisa/ngo,” *Classical and Quantum Gravity*, vol. 29, p. 124016, 2012.

- [29] “Artists impression of elisa.” <https://www.elisascience.org/multimedia/image/admin-lisa-satellite>, First accessed in September 2015.
- [30] G. Hammond, S. Hild, and M. Pitkin, “Advanced technologies for future ground-based, laser-interferometric gravitational wave detectors,” *Journal of Modern Optics*, vol. 61, no. S1, pp. S10–S45, 2014.
- [31] J. Driggers, J. Harms, and R. X. Adhikari, “Subtraction of newtonian noise using optimized sensor arrays,” *Physical Review D*, vol. 86, pp. 102001–1, 2012.
- [32] G. Cella, “Underground reduction of gravity gradient noise.” LIGO Document G060331, 2006.
- [33] M. Punturo, M. Abernathy, F. Acernese, *et al.*, “The einstein telescope: a third generation gravitational wave observatory,” *Classical and Quantum Gravity*, vol. 27, p. 194002, 2010.
- [34] T. Accadia, F. Acernese, F. Antonucci, *et al.*, “Noise from scattered light in virgo’s second science run data,” *14th Gravitational Wave Data Analysis Workshop*, vol. 27, no. 19, p. 194011, 2010.
- [35] J. Hough, S. Rowan, and B. S. Sathyaprakash, “The search for gravitational waves,” *Journal of Physics B: Atomic, Molecular and Optical Physics*, vol. 38, pp. S497–S519, 2005.
- [36] S. Hild, *Advanced Interferometers and the Search for Gravitational Waves - Lectures from the First VESF School on Advanced Detectors for Gravitational Waves - A basic introduction to quantum noise and quantum non demolition techniques*, vol. 404. Springer International Publishing, 2014.

- [37] K. L. Dooley, T. Akutsu, S. Dwyer, and P. Puppó, “Status of advanced ground-based laser interferometers for gravitational-wave detection,” *Journal of Physics: Conference Series*, vol. 610, p. 012012, 2015.
- [38] C. M. Caves, “Quantum-mechanical radiation-pressure fluctuations in an interferometer,” *Physical Review Letters*, vol. 45, no. 2, pp. 75–79, 1980.
- [39] S. Großler, A. Bertolini, M. Born, *et al.*, “The aei 10 m prototype interferometer,” *Classical and Quantum Gravity*, vol. 27, p. 084023, 2010.
- [40] C. Gräf, B. W. Barr, A. S. Bell, *et al.*, “Design of a speed meter interferometer proof-of-principle experiment,” *Classical and Quantum Gravity*, vol. 31, p. 215009, 2014.
- [41] J. Belfi and F. Marin, “Sensitivity below the standard quantum limit in gravitational wave detectors with michelson-fabry-perot readout,” *Physical Review D*, vol. 77, p. 122002, 2008.
- [42] A. Einstein, “Über die von der molekularkinetischen theorie der wärme geforderte bewegung von in ruhenden flüssigkeiten suspendierten teilchen,” *Annalen de Physik*, vol. 322, pp. 549–560, 1905.
- [43] R. Brown, “A brief account of microscopical observations on the particles contained in the pollen of plants,” *Edinburgh new philosophical journal*, p. 358, 1828.
- [44] H. B. Callen and T. A. Welton, “Irreversibility and generalized noise,” *Physical Review*, vol. 83, no. 1, pp. 34–40, 1951.
- [45] R. F. Greene and H. B. Callen, “On the formalism of thermodynamic fluctuation theory,” *Physical Review*, vol. 83, no. 6, pp. 1231–1235, 1951.
- [46] A. S. Nowick and B. S. Berry, *Anelastic relaxation in crustalline solids*. 111 Fifth Avenue, New York, New York 10003: Academic Press, New York, 1972.

- 
- [47] S. D. Penn, G. M. Harry, A. M. Gretarsson, *et al.*, “High quality factor measured in fused silica,” *Review of Scientific Instruments*, vol. 72, no. 9, p. 7630, 2001.
- [48] C. J. Bel, S. Reid, J. Faller, *et al.*, “Experimental results for nulling the effective thermal expansion coefficient of fused silica fibres under a static stress,” *Classical and Quantum Gravity*, vol. 31, no. 6, p. 065010, 2014.
- [49] P. R. Saulson, “Thermal noise in mechanical experiments,” *Physical Review D*, vol. 42, no. 8, pp. 2437–2445, 1990.
- [50] A. V. Cumming, A. S. Bell, L. Barsotti, *et al.*, “Design and development of the advanced ligo monolithic fused silica suspension,” *Classical and Quantum Gravity*, vol. 29, no. 3, p. 035003, 2012.
- [51] S. M. Aston, M. A. Barton, A. S. Bell, *et al.*, “Update on quadruple suspension design for advanced ligo,” *Classical and Quantum Gravity*, vol. 29, p. 235004, 2012.
- [52] J. E. Logan, J. Hough, and N. A. Robertson, “Aspects of the thermal motion of a mass suspended as a pendulum by wires,” *Physics Letters A*, vol. 183, pp. 145–152, 1990.
- [53] S. Göbner, G. Cagnoli, D. R. M. Crooks, *et al.*, “Damping and tuning of the fibre violin modes in monolithic silica suspensions,” *Classical and Quantum Gravity*, vol. 21, pp. S923–S933, 2004.
- [54] A. V. Dmitriev, S. D. Mescherlakov, K. V. Tokmakov, and V. P. Mitrofanov, “Controllable damping of high-q violin modes in fused silica suspension fibers,” *Classical and Quantum Gravity*, vol. 27, p. 025009, 2010.

- [55] T. Westphal, G. Bergmann, A. Bertolini, *et al.*, “Design of the 10 m aei prototype facility for interferometry studies. a brief overview,” *Applied Physics B: Lasers and Optics*, vol. 106, no. 3, pp. 551–557, 2012.
- [56] A. Heptonstall, M. A. Barton, A. Bell, *et al.*, “Invited article: Co2 laser production of fused silica fibers for use in interferometric gravitational wave detector mirror suspensions,” *Review of Scientific Instruments*, vol. 82, no. 1, p. 011301, 2011.
- [57] A. Conway, “Preliminary design and control program for co2 laser based fused silica ”micro” fiber pulling machine,” Master’s thesis, Lake Forest College, August 2014.
- [58] A. Thüring and N. Lastzka, “Just another mode matching tool.” <http://www.sr.bham.ac.uk/dokuwiki/doku.php?id=geosim:jammt>, First accessed in December 2014.
- [59] Firestar, “Data sheet for firestar f100 laser.” <http://www.synrad.com/fseries/f100.htm>, First accessed in December 2014.
- [60] Crystran, “Refractive index of zinc selenide.” <http://www.crystran.co.uk/optical-materials/zinc-selenide-znse>, First accessed in December 2014.
- [61] P. E. Ciddor, “Refractive index of air: new equations for the visible and near infrared,” *Applied Optics*, vol. 35, no. 9, pp. 1663–1667, 1996.
- [62] A. V. Cumming, *Aspects of mirrors and suspensions for advanced gravitational wave detectors*. PhD thesis, University of Glasgow, 2008.
- [63] A. V. Cumming, M. A. Barton, and C. Gianpietro, “Apparatus for dimensional characterization of fused silica fibers for the suspensions of advanced gravitational wave detectors,” *Review of Scientific Instruments*, vol. 82, p. 044502, 2011.

- 
- [64] G. Taylor, “Design of the mkiii igr strength testing unit,” tech. rep., University of Glasgow, 2013.
- [65] A. Heptonstall, M. A. Barton, A. S. Bell, *et al.*, “Enhanced characteristics of fused silica fibers using laser polishing,” *Classical and Quantum Gravity*, vol. 31, no. 10, p. 105006, 2014.
- [66] Crystran, “Young’s modulus of fused silica.” <http://www.crystran.co.uk/optical-materials/silica-glass-sio2>, First accessed in April 2015.
- [67] K. V. Tokmakov, A. Cumming, J. Hough, *et al.*, “A study of the fracture mechanisms in pristine silica fibres utilising high speed imagine techniques,” *Journal of non-crystalline solids*, vol. 358, pp. 1669–1709, 2012.